Apology and Correction Notice

We would like to express our sincere apologies for the errors in the description found in KOBELCO TECHNOLOGY REVIEW No. 40, which was published in January 2023.

We understand that these errors may have caused inconvenience to our readers and other concerned parties.

Specifically, we would like to clarify the author names in the table of contents for the article on page 71.

Incorrect ： Dr. Takayuki TSUBOTA, Dr. Takashi ACHIHA, Yoshiki HAYASHI,
Dr. Takuya MORI, Hiroshi OZONO

Correct   ： Dr. Takayuki TSUBOTA, Dr. Takashi ACHIHA, Yoshiki HAYASHI,
Dr. Takuya MORI, Hiroshi OZONO, <u>Hidemasa TSUNEISHI</u>

KOBELCO TECHNOLOGY REVIEW

No. **40** *Jan. 2023*

Feature- I : Prediction and Measurement of Microstructures and Properties in Materials
Feature- II : Functional Materials and Solutions for Diverse Needs of Society

Contents

Feature- I Prediction and Measurement of Microstructures and Properties in Materials

Feature- II Functional Materials and Solutions for Diverse Needs of Society

First-principles Calculations on Co-segregation of P and Transition Metal Elements at Fe Grain Boundaries

Shinya MORITA[*1]

[*1] Applied Physics Research Laboratory, Technical Development Group

Abstract

The first-principles (ab-initio) calculations based on the FeΣ3 (111) grain boundary model have been used to study the effects of transition metal elements, Cr, Mn, and Mo, on the grain-boundary co-segregation and of P contained in the steel and on the grain-boundary embrittlement. It has been found that Cr, Mn, and Mo indicate repulsive interactions with P at the grain boundaries of Fe and that the shorter the distance to the P atom, the stronger the repulsive interactions become. The interactions have turned out to be small relative to the grain boundary segregation energy of P, causing only a small effect on the segregation behavior of P. However, Mo, when segregated on the grain boundaries, increases the binding energy of the grain boundaries, and is expected to suppress the grain-boundary embrittlement due to P.

Introduction

In ferrous materials, grain boundaries are prone to brittle fracture. In particular, grain boundary embrittlement is well-known to occur when impurity elements such as P and S segregate on the grain boundary, decreasing material strength and ductility. Embrittlement phenomena due to grain boundary segregation include the low-temperature temper embrittlement of low alloy steel,[1] grain boundary cracking by S segregation of Ni steel,[2] and high-temperature cracking in welding.[3] Controlling grain boundary segregation is an essential issue in various materials for mechanical structures.

In order to suppress grain boundary embrittlement, it is necessary not only to reduce grain boundary embrittlement elements such as P and S in steel to the utmost limit, but also to consider the influence of additive elements in the steel. For example, Mn has a high affinity with P and promotes co-segregation. In addition, Cr and Mo form carbide, reducing the grain-boundary segregation of C and promoting the segregation of P. Thus, alloying elements affect the segregation of P on grain boundaries due to various factors.

A certain amount of Mo has been reported to strengthen the grain boundaries while lowering the ductile-to-brittle transition temperature (DBTT).[4]-[7] When multiple elements segregate on grain boundaries, the amount of grain-boundary segregation may be affected by site competition for stable sites (atomic positions) and by interatomic interaction. In reality, however, P, S, and transition metal elements in steel form carbides and alloy compounds, affecting the amount of solid solution that contributes to the grain boundary segregation. Therefore, it is difficult to quantitatively consider the effect of interatomic interaction on the grain boundary segregation of embrittling elements such as P and S.

On the other hand, the first-principles calculations allow the analysis of interatomic interactions, enabling the consideration of the mechanisms for grain boundary co-segregation. As a result, guidelines will be obtained for the future development of high-strength materials. Studies on grain boundary segregation, using first-principles calculations, have also been conducted on ferrous materials. Its effects on segregation tendency and grain boundary strength are considered using indexes such as grain boundary segregation energy and grain boundary binding energy.[8]-[10] For example, Yamaguchi et al. studied the grain boundary segregation of light elements such as P using the Σ3 (111) grain boundary of bcc iron as a model. They clarified that the grain boundary aggregation energy correlates with the ductile-to-brittle transition temperature.[8]

However, no report considers the co-segregation of P with transition metal elements in actual materials. Therefore, this study uses first-principles calculations to investigate the effects of transition metal elements, Cr, Mn, and Mo, on the grain boundary segregation of P and the grain boundary strength, these being elements that are widely used to strengthen ferrous materials, for example.

1. Calculation method

The first-principles calculations for the grain boundaries have employed the bcc-Fe Σ3 (111) grain-boundary model (76 atoms) with excellent symmetry. **Fig. 1** shows the grain-boundary model. Here, the central part is the grain boundary, the upper and lower surface sides are provided with vacuum layers, and all three axes are periodic boundary conditions. The grain boundary energy calculated on the basis of this model is 1.23 J/m², which is close to the energy value, 1.48 J/m²,[11] of Σ27 (552) grain boundary, an almost random
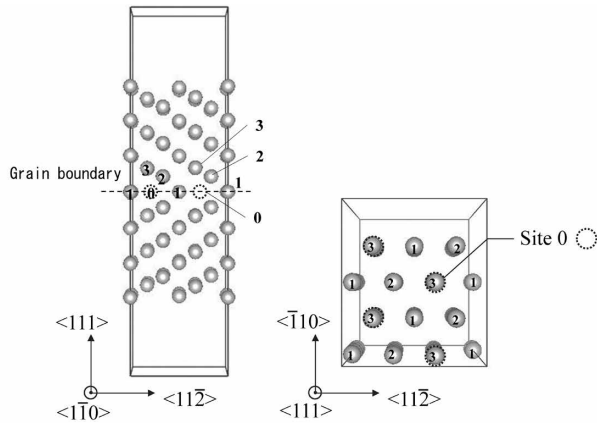
Fig. 1 bcc-Fe Σ 3(111) grain boundary model

grain boundary. This result suggests that the grain boundary segregation tendency at the Σ 3 grain boundary also applies to other random grain boundaries.

The grain boundary segregation sites have been numbered from 0 to 3, as shown in the figure, and the additive elements P, Cr, Mn, and Mo have been arranged at these sites. In the co-segregation calculations, the sites 0 to 3 have been occupied, respectively, by either P or a transition metal element X (here, X refers to one of the elements, Cr, Mn, or Mo), and the calculations have been carried out for a total of 4 × 4 = 16 arrangements. Since the grain boundary segregation energy of the additive elements corresponds to the energy difference between the time when they are segregated on grain boundaries and when they are dissolved as a solid solution in the grains, it has been calculated from Eq.(1):

$$E^{gb}_{seg}[X] = E_{gb}[\text{Fe-X}] + E_{bk}[\text{Fe}] - \{E_{gb}[\text{Fe}] + E_{bk}[\text{Fe-X}] + \mu_{\text{Fe}}\} \quad \cdots\cdots\cdots\cdots\cdots\cdots (1)$$

wherein $E_{gb}[\text{Fe-X}]$, $E_{bk}[\text{Fe-X}]$, $E_{bk}[\text{Fe}]$, and $E_{gb}[\text{Fe}]$ respectively represent the Fe grain boundary when an X atom segregates to a grain boundary, iron crystals when X atom is dissolved as a solid solution in a grain, pure iron crystal, and the total grain boundary energy of pure iron Fe. μ_{Fe} is a chemical potential term for correcting the number of Fe atoms.

The P-X interatomic interaction energy, $E_{int}[\text{P, X}]$, and the grain boundary co-segregation energy, $E_{coseg}[\text{P, X}]$, when P and X atoms co-segregate, are defined by Equations (2) and (3), respectively:

$$E_{int}[\text{P, X}] = E_{gb}[\text{Fe-P-X}] + E_{gb}[\text{Fe}] - \{E_{gb}[\text{Fe-P}] + E_{gb}[\text{Fe-X}]\} \quad \cdots\cdots\cdots\cdots (2)$$

$$E_{coseg}[\text{P, X}] = E_{gb}[\text{Fe-P-X}] + 2E_{bk}[\text{Fe}] - \{E_{gb}[\text{Fe}] + E_{bk}[\text{Fe-P}] + E_{bk}[\text{Fe-X}]\} \quad \cdots\cdots\cdots (3)$$

wherein $E_{gb}[\text{Fe-P-X}]$ is the total energy of the Fe grain boundary when P and X atoms are arranged at the grain boundary, and $E_{int}[\text{P, X}]$ is the energy difference between the time when the P and X atoms are co-segregated at a grain boundary and when they are independently segregated. $E_{coseg}[\text{P, X}]$ is the energy difference between the time when the P and X atoms co-segregate at the grain boundary and the time when they are solid-solutioned in the grain, and the P and X atomic arrangements that minimize $E_{coseg}[\text{P, X}]$ are the most likely ones.

The grain boundary binding energy corresponds to the grain boundary strength and is expressed by Eq. (4) using grain boundary energy, surface energy, and grain boundary area S:

$$E_{bind} = (2E_{surf} - E_{gb})/S \quad \cdots\cdots\cdots\cdots\cdots\cdots\cdots\cdots\cdots (4)$$

The first-principles calculations have employed the Vienna Abinitio Simulation Package (VASP) code based on the density functional theory,[12] and the interatomic potential has used the Perdew-Burke-Ernzerhof (PBE) type Projector-Augmented-Wave (PAW) potential.[13] The cutoff energy of the plane wave basis set is 280 eV, and the k-point mesh in the grain-boundary model in Fig. 1 is 3 × 4 × 1 of the Monkhorst Pack. In addition, the 0.2 eV-wide Methfessel-Paxton smearing method[14] has been used to improve convergence. For structure optimization calculation, all atoms are relaxed after the alloy atoms have been arranged, and the convergence condition has been set to an atomic force of 0.02 eV/Å or less.

2. Calculation results and considerations

2.1 Grain boundary segregation energy during independent segregation

In order to investigate how easily each element segregates on grain boundaries, the grain boundary segregation energy during independent segregation has been calculated for P, Cr, Mn, and Mo. The results are shown in **Fig. 2** (a) to (d). The lower the value, the easier it is to segregate. Phosphorus has the lowest grain boundary segregation energy, and its segregation energies are -1.0 eV/atom and -1.15 eV / atom at Site 0 and Site 2, respectively. Similar to P, Site 2 is most stable for Cr and Mn, and their segregation energies are -0.19 eV/atom and -0.32 eV/ atom, respectively. Of the elements, Mo is the only one most stable at Site 1, and its segregation energy is -0.41 eV/atom.

On grain boundaries, the atomic arrangement is different from that in grains. Therefore, the Voronoi volume, which corresponds to the volume of the
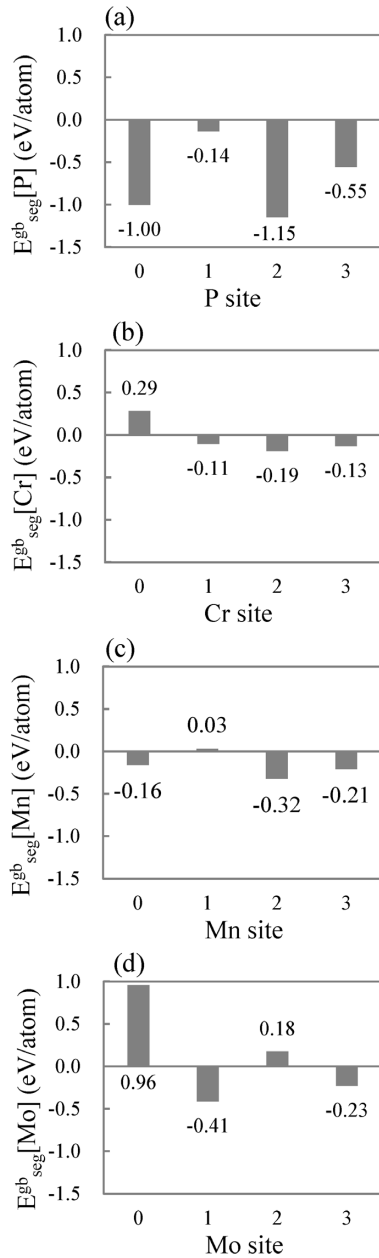
Fig. 2 Calculation results of grain boundary segregation energy at Fe grain boundary ((a)P, (b)Cr, (c)Mn, (d)Mo)

Fig. 3 Relationship between grain boundary segregation energy and Voronoi volume

Fig. 4 Relationship between co-segregation energy and interaction energy with P and X[X=(a)Cr, (b)Mn, (c)Mo] atoms at Fe grain boundary

space occupied by one atom, differs from that in a Fe crystal grain. It is known that the grain boundary segregation energy depends strongly on the Voronoi volume.[9] **Fig. 3** shows the relationship between the Voronoi volumes of the alloying elements and the segregation energies at the segregation sites. The numbers in the graph indicate the segregation site numbers. The Voronoi volumes at pure-iron grain boundaries are 10.2, 13.1, 11.1, and 12.3 Å^3 at Sites 0, 1, 2, and 3, respectively.

The elements P, Cr, and Mn with Voronoi volumes of 11.1 to 11.3 Å^3 in iron crystal grains are most stable at Site 2, while Mo with a Voronoi volume of 11.7 Å^3 is most stable at Site 1. Each tends

to enter a site at the grain boundary with a Voronoi volume similar to itself. In particular, P and Mo, each having an atomic radius significantly different from the base material Fe, are more stable when put on grain boundaries, where various atomic volumes are allowed to exist, and the grain boundary segregation energy decreases.

2.2 Grain boundary segregation energy during co-segregation

Next, P and X are arranged simultaneously on the grain boundary to investigate the P-X interaction energy and co-segregation energy on grain boundaries for each atomic arrangement. The results are shown in **Fig. 4** (a) to (c). The plots in (a) to (c) indicate the atomic arrangement of P, and the numbers in the figure are the site numbers of the X atom. The lower the co-segregation energy on the horizontal axis, the higher the feasibility of the atomic arrangement in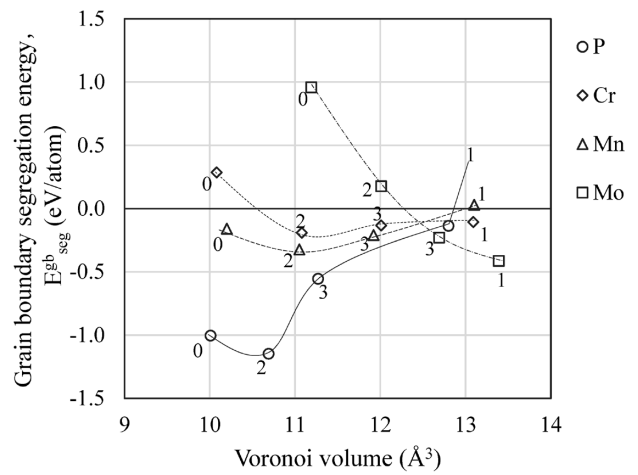 the grain boundary co-segregation. The element P with a low energy of independent segregation tends to have low co-segregation energy when arranged at Site 0 or Site 2. Many plots fall in the first quadrant of the graph, where the interaction energy is positive, and as a whole, repulsive interaction works with P. The interaction energy varies widely from -0.5 to +1.0 eV/atom, and the arrangement of P and X atoms is considered to have a significant effect. As for the differences among the elemental species, Mn has negative interaction energy for P0-Mn0 (arrangement of P and Mn to Site 0, respectively)

and for arrangement P3-Mn0, which has low co-segregation energy, and its repulsive interaction is weaker than those of Cr and Mo.

Similarly, as a result of calculating the P-X interatomic interaction in the bcc-Fe crystal grain from the first-principles calculations, the interaction energies of Cr, Mn, and Mo against P are -0.06, -0.24, and +0.02, respectively. Since Mn has an attractive interaction with P in the crystal and the repulsive interaction is weaker than those of Cr and Mo, this tendency is considered to be inherited even at the grain boundary.

2.3 Dependence of grain boundary segregation energy on Voronoi volume

Fig. 5 (a) to (f) show the results of investigating the relationship between the grain boundary segregation energy of P-X atoms during co-segregation and the Voronoi volume. Fig. 5 (a) and (d), (b) and (e), and (c) and (f) are the results of the co-segregation of P and X atoms, respectively. The upper figures (a) to (c) show the relationship between the segregation energy and Voronoi volume for the P atoms, while the lower figures (d) to (f) show those for the X atoms. The solid plots indicate the relationship during independent segregation, and the numerical values in the figures indicate the sites of coupling atoms. As for P, the grain boundary segregation energy depends on the Voronoi volume of P, although there are variations, and, as in the case of independent segregation, this energy tends to have a minimum value of around 10.5 to 11.0 Å^3
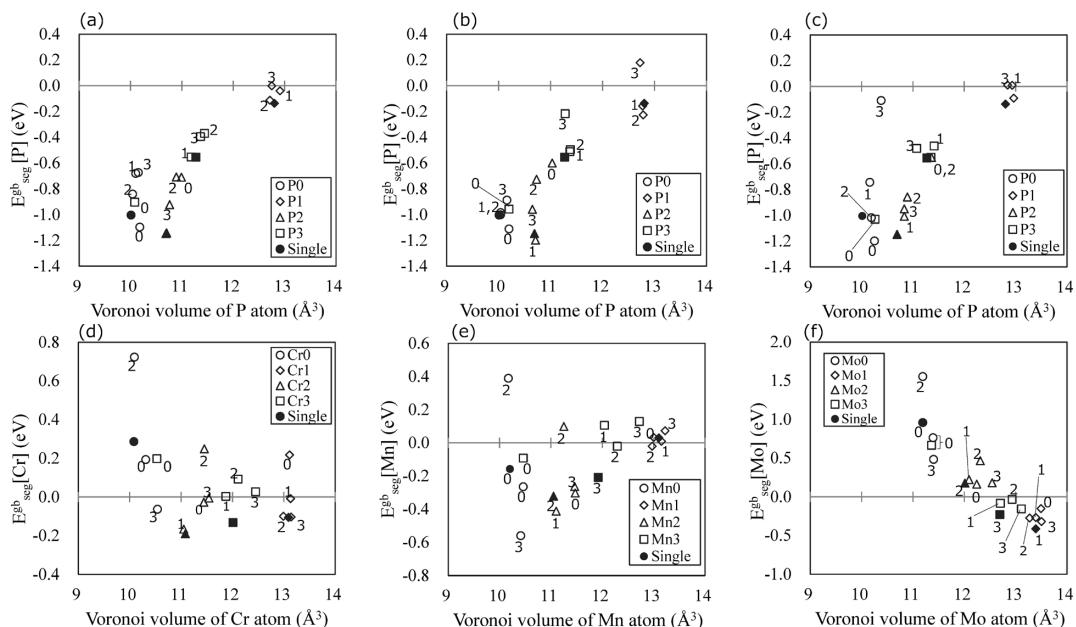

Fig. 5 Relationship between grain boundary segregation energy and Voronoi volume of segregation atoms during P, X co-segregation. (X=Cr (a, d), Mn (b, e), Mo (c, f))

during co-segregation. On the other hand, Cr and Mn do not show as significant a Voronoi volume dependence as that of P and are considered to be strongly influenced by the interaction with P.

Now the effect of atomic position is studied in detail. From Fig. 5 (a) to (c), when P is arranged at Site 0 (notation P0 in the figure), the Voronoi volume increases due to the arrangement of X atoms at P0-X0, so the grain boundary segregation energy of P becomes lower than that during independent segregation. On the other hand, in P0-X1 and P0-X2, the segregation energy of P tends to increase slightly, and in P0-X3, the segregation energy of P increases significantly in the case of Cr and Mo.

Fig. 6 (a) and (b) show the grain boundary structures of the P0-X1 and P0-X3 arrangement, respectively. The interatomic distance of P0-X1 is 2.52 to 2.57 Å, while that of P0-X3 is 2.21 to 2.31 Å, the latter being shorter than the former. The nearest distance of P, X atoms neighboring in Fe grains is 2.49 to 2.58 Å, and the P0-X3 arrangement is shorter than this. Therefore, the P atom is subjected to a considerable strain, generating a significant repulsive force. This effect is particularly significant for Mo, which has a large atomic radius. The same is true when P is arranged on Site 2, where the interatomic distance of P2-X1 is 2.57 to 2.76 Å, whereas P2-X2 is as small as 2.2 to 2.35 Å; in the latter case, the segregation energy of P is increased.

Fig. 7 shows the relationship between P-X interatomic interaction energy and the interatomic distance when P is arranged at Sites 0 and 2. This result indicates that the repulsive force is more significant near 2.2 Å, where the interatomic distance is short, and the interaction energy becomes zero at around 2.6 Å for Mn and 2.8 Å for Cr and Mo. Thus, the interaction energy correlates with the P-X interatomic distance, and as shown in Fig. 7, Cr and Mo have a repulsive interaction stronger than that of Mn by approximately 0.2 eV.

2.4 Effect of grain boundary segregation elements on grain boundary strengthening and embrittlement

Changes in grain boundary binding energy have been calculated to investigate the effect of alloying elements on the grain boundary strength, and the results are shown in **Table 1**. Since the grain boundary binding energy depends on the difference between the surface segregation energy and the grain boundary segregation energy, these energies are also described. Element P has a surface segregation energy lower than the grain boundary segregation energy (surface segregation is increasingly stable). Therefore, the sign of grain boundary binding energy is negative, and as is known empirically, it causes grain boundary embrittlement. On the other hand, Cr, Mn, and Mo all show positive values and have a grain boundary strengthening effect, in which Mo is prone to grain boundary segregation and has the most significant strengthening effect. Generally, elements prone to grain boundary segregation have a low surface segregation energy like P, but this does not apply to Mo, which shows a positive sign.

In order to investigate the effect of surface segregation energy, the differential charge density distribution during surface segregation (change in charge density due to the arrangement of P and Mo on the surface) has been analyzed. The results are shown in **Fig. 8**. The differential charge density is caused by the fact that the P and Mo arranged on the surface are bound to 4 Fe atoms on the bulk side
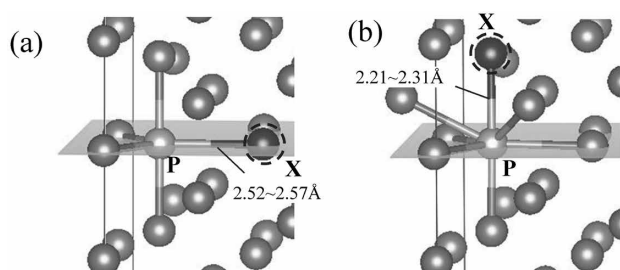

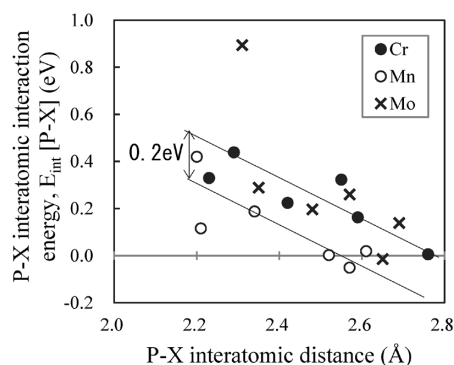Fig. 6 Grain boundary structure in case of (a)P0-X1 and (b)P0-X3 atomic configuration

Fig. 7 Relationship between P-X interatomic interaction energy and interatomic distance on grain boundary

Table 1 Surface segregation energies, grain boundary segregation energies, and grain boundary binding energies of P, Cr, Mn, and Mo

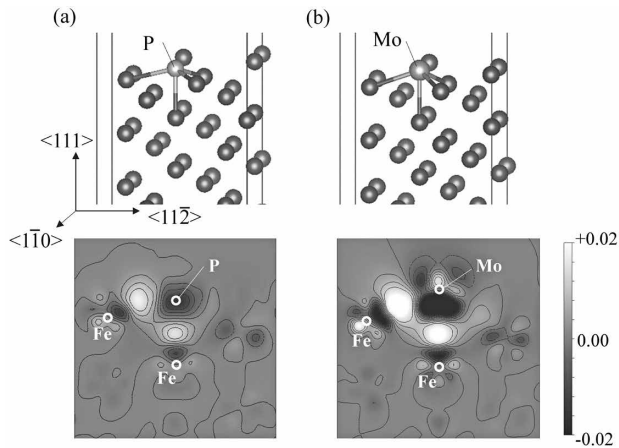| Atom	E^{sf}_{seg} (eV/atom)	E^{gb}_{seg} (eV/atom)	ΔE^{gb}_{bind} (J/m^2)
P	-1.50	-1.15	-0.10
Cr	-0.09	-0.19	0.03
Mn	-0.02	-0.32	0.09
Mo	0.11	-0.41	0.15

Fig. 8 Fe(111) surface structure and differential charge density distribution during (a)P and (b)Mo segregation

but are unbonded on the surface side. Mo exhibits a differential charge density in this part, while P does not. This difference is attributed to the fact that, in P, 3s and 3p electrons create a valence band, whereas Mo constitutes a valence band with 4d electrons. The d electrons have a narrower bandwidth than the s or p electrons and have an electron cloud that is more strongly anisotropic. Therefore, the repulsing electrons are also distributed on the side of unstable unbonded hands, resulting in the high surface segregation energy.

Conclusions

The first-principles calculations have been used to consider the effects of the transition metal elements, Cr, Mn, and Mo, on the grain boundary segregation of P at the Fe Σ 3 (111) grain boundary from the perspective of grain boundary interaction. It has been shown that all of the elements exhibit the grain boundary segregation tendency, and the grain boundary segregation energy depends on the relationship between the Voronoi volume and the atomic radius of the segregation site.

The elements Cr, Mn, and Mo, show repulsive interaction with P on grain boundaries and are expected to reduce the grain-boundary segregation of P from the viewpoint of interatomic interaction. It was also found that, among the three elements, Mo is expected to increase the grain boundary binding energy by grain boundary segregation and suppress the grain boundary embrittlement by P.

On the other hand, in actual materials, it is necessary to consider various phenomena such as the formation of grain boundary characters and grain boundary precipitates, carbide formation, which affects the segregation amount, and the change in the solid-solution amount due to the formation of precipitates. It is considered that the future challenge will be to predict the segregation amount after examining these effects in more detail.

References

1) Y. Murakami et al. Bulletin of the Japan Institute of Metals. 1981, Vol.20, No.9, pp.784-793.
2) J. Murakami et al. Tetsu- to-Hagane. 1987, Vol.73, No.1, pp.191-198.
3) F. Matsuda. JOURNAL OF THE JAPAN WELDING SOCIETY. 1967, Vol.36, No.9, pp.973-986.
4) J. Kameda. Bulletin of the Japan Institute of Metals. 1980, Vol.19, No.8, pp.595-603.
5) J. Yu et al. Met. Trans. A. 1980, Vol.11A, pp.291-300.
6) J. Wu et al. Mat. Charact. 2008, Vol.59, pp.261-265.
7) M. Carcia-Mazario. J. Nuc. Mat. 2007, Vol.360, pp.293-303.
8) M. Yamaguchi. J. Japan Inst. Met. Mater. 2008, Vol.72, No.9, pp.657-666.
9) J. Wang et al. Acta. Mat. 2016, Vol.115, pp.259-268.
10) Y-J. Hu et al. Comp. Mat. Sci. 2020, Vol.171, p.109271.
11) E. Nakajima et al. Tetsu-to-Hagane. 2000, Vol.86, No.5, pp.357-362.
12) G. Kresse et al. Phys. Rev. B. 1994, Vol.49, pp.14251-14269.
13) G. Kresse et al. Phys. Rev. B. 1999, Vol.59, pp.1758-1775.
14) M. Methefessel et al. Phys. Rev. B. 1989, Vol.40, pp.3616-3621.

Multiscale Elasto-plastic Finite Element Analysis of Dual-phase Steel Based on Homogenization Method

Dr. Eisuke KUROSAWA[*1]

[*1] Mechanical Engineering Research Laboratory, Technical Development Group

Abstract

High tensile steel, such as dual-phase steel consisting of ferrite and martensite, is still widely used in several industries. From a research and development point of view, it is important to clarify the relationship between microstructure and macroscopic mechanical properties. In this study, samples of dual- or single-phase steel consisting of similar constituent phases were experimentally produced, and their tensile properties were obtained by material testing. These data were introduced into the microstructure model generated by an image-based modeling method using SEM observation imaging. Using this model, multiscale FE simulation based on homogenization elasto-plasticity theory was conducted, and validation was investigated by comparison with experimental results.

Introduction

The development of high-strength steel materials is being actively promoted to, for example, meet the needs for the weight reduction of transport equipment such as automobiles. A typical material is dual-phase steel (hereinafter referred to as "DP steel"), which comprises ferrite and martensite phases. The material properties of such high-strength steel have been improved by controlling its internal structure. Many studies have been conducted to elucidate the effect of microstructure on macroscopic material properties such as mechanical properties, formability, and ductile fracture behavior.[1)-3)] In recent years, evaluation by multiscale simulation has been attracting attention as an effective means. However, there still are only a few analysis examples for steel[4), 5)] and, at present, the correlation between material properties and structural morphology has not been organized systematically.

This study focuses on DP steel, in which mechanical property data for each constituent phase has been obtained by material testing. An attempt has been made to create a mesh model for analysis to reproduce the structural observation results faithfully. In addition, a large deformation finite element (FE) simulation code based on homogenized elasto-plastic theory[6), 7)] has been developed to perform multiscale strength analysis using the above data.[8)] This paper examines the validity and effectiveness of the developed method by comparing the analysis results with the experimental results.

1. Material testing

1.1 Testing materials

The prepared samples included DP steel, as well as single-phase materials each having properties comparable to respective phase constituting the DP steel. First, a 20 kg vacuum induction melting furnace was used to melt three types of ingots that had been adjusted to meet the target compositions. **Table 1** shows the compositions of the ingots at this stage. The smelted ingots were heated at 1,150℃ for more than 30 minutes. Subsequently, they were forged at 800℃ to a round-bar shape of approximately $\phi 10 \times L150$ mm. After that, they were heat-treated in a salt-bath furnace under the conditions shown in Table 1 to provide three types of samples for the benchmark testing. **Fig. 1** shows the SEM observation images of the internal structure of each sample.

Also, the amount of solid-solution carbon in the martensite phase was analyzed by EPMA. As a result, the average was 0.40 wt% in the DP steel sample (Fig. 1 (a)), while it was 0.49 wt% in the martensite single-phase sample (Fig. 1 (c)). This suggests that the obtained materials have characteristics almost comparable to those of martensite phase.

Furthermore, the structural image in Fig. 1 (a) was analyzed to calculate the surface fraction of the martensite phase in the DP steel sample, and the fraction turned out to be 10 to 15%.

1.2 Tensile testing

Multiple sheet specimens with a gauge length of 12.5 mm, a width of 3 mm, and a thickness of

Table 1 Compositions and heat treatment condition of each steel sample

Sample	Composition (wt%)			Heat treatment condition
	C	Si	Mn	
(a) Dual-phase	0.063	0.50	1.46	800℃-30min 650℃-10min WQ
(b) Ferrite	0.032	0.43	1.37	880℃-30min AC
(c) Martensite	0.49	0.59	1.59	880℃-30min WQ
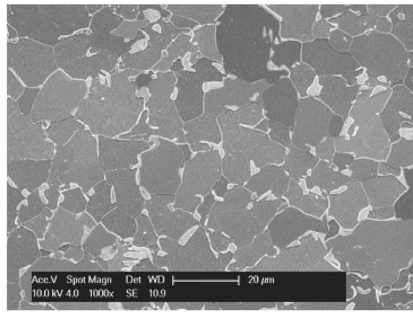
(a)Dual-phase
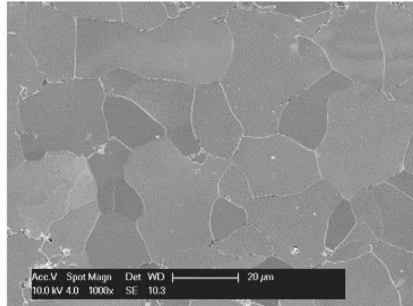
(b)Ferrite
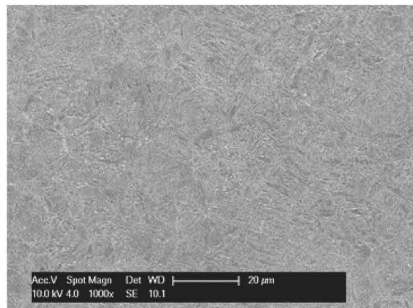
(c)Martensite

Fig. 1 SEM image of each steel sample
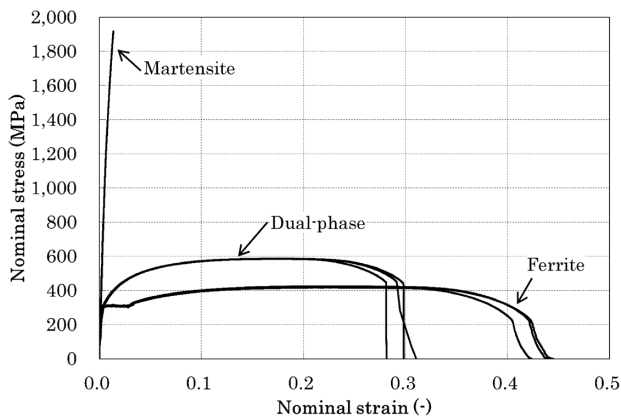
Fig. 2 Nominal stress vs. nominal strain curves of each steel sample

1.2 mm were cut out from each of the above samples. These specimens were subject to tensile testing using a universal testing machine under a crosshead displacement rate of 1 mm/min and room temperature environment.

Fig. 2 shows each sample's nominal stress–nominal strain diagram. Reproducible data were obtained for the DP steel and ferrite single-phase material. The tensile strength of the DP steel prepared this time was slightly less than 600 MPa. On the other hand, the martensite single-phase material exhibited extremely brittle behavior and resulted in fracture at an extremely low strain region (nominal strain 1.4% at the maximum).

2. Formulation based on homogenized elasto-plastic theory

Homogenization method[6), 7)] is one of the numerical analysis methods for coupling and analyzing mechanical behaviors of different scales. In the homogenization method, the governing equations of micro- and macro-scales satisfy physical and mathematical consistency and are versatile enough to handle any geometry in micro-construction.[6)] Therefore, in this study, an attempt has been made to formulate a FE simulation on the basis of the homogenization theory extended to the large deformation elasto-plastic problems.[6), 7)]

The displacement velocity vector $\dot{u}$ at any material point is assumed to be additively decomposable as in the following equation:

$$\dot{u} = \dot{u}^0 + \dot{u}^* \quad\cdots\cdots\cdots\cdots\cdots\cdots\cdots\cdots\cdots (1)$$

wherein the right superscript 0 and * represent the uniform macroscopic component and the perturbed component therefrom, respectively. The macroscopic component acts uniformly on the micro-scale structure, and the perturbed component is the quantity due to the heterogeneity of the micro-scale structure.

The homogenization method assumes that the perturbed component is distributed in the unit cell Y corresponding to the unit structure of the micro-scale, and this Y is placed periodically. This periodicity is referred to as Y-periodicity, and it is generally known that the obtained macroscopic response satisfies various mechanical consistency if the perturbed component $\dot{u}^*$ is a function that changes periodically.[6)]

The following equation was adopted as the material constitutive law for micro-scale structure based on large deformation theory.

$$\check{\sigma} = C^{ep} : D \quad\cdots\cdots\cdots\cdots\cdots\cdots\cdots\cdots\cdots\cdots\cdots (2)$$
$$\check{\sigma} \equiv \dot{\sigma} - L\sigma - \sigma L^{T} \quad\cdots\cdots\cdots\cdots\cdots\cdots\cdots\cdots (3)$$

wherein

σ : microscopic Cauchy stress tensor

$\check{\sigma}$: upper-convective derivative for microscopic Cauchy stress tensor

C^{ep} : micro isotropic elasto-plastic coefficient tensor

D : deformation rate tensor
L : gradient tensor for displacement rate.

It should be noted that the plastic constitutive equation incorporates the related flow rule, and the Mises yield condition has been used for each phase that constitutes the micro-scale structure. According to the homogenization theory in the framework of large deformation by Ohno et al.,[7] the governing equations of micro-scale are derived as equation (4), and the homogenized elasto-plastic constitutive law of macro-scale is derived as equation (5) ;

$$\int_Y \left\{ \frac{1}{2} C_{ijmn}^{ep} (\dot{\chi}_{m,n}^{<kl>} + \dot{\chi}_{n,m}^{<kl>}) \delta \ddot{u}_{i,j}^* + \dot{\chi}_{i,m}^{<kl>} \sigma_{m,j} \delta \ddot{u}_{i,j}^* \right\} dY = \int_Y C_{ijkl}^{ep} \delta \ddot{u}_{i,j}^* dY$$

$$\cdots\cdots\cdots\cdots\cdots\cdots\cdots\cdots \quad (4)$$

$$\check{\Sigma} = C^{epH} : D^0 \quad \cdots\cdots\cdots\cdots\cdots\cdots \quad (5)$$

$$C_{ijkl}^{epH} \equiv \frac{1}{|Y|} \int_Y (C_{ijkl}^{ep} - C_{ijmn}^{ep} \dot{\chi}_{m,n}^{<kl>}) dY \quad \cdots\cdots\cdots\cdots \quad (6)$$

$$\ddot{u}_i^* = \dot{\chi}_i^{<kl>} D_{kl}^0 \quad \cdots\cdots\cdots\cdots\cdots\cdots\cdots \quad (7)$$

wherein

$\dot{\chi}_i^{<kl>}$: characteristic displacement rate vector
$\delta \ddot{u}_i^*$: perturbed component of virtual displacement rate
$\check{\Sigma}$: upper-convective derivative for macroscopic Cauchy stress tensor
C^{epH} : homogenized macroscopic elasto-plastic coefficient tensor
D^0 : macroscopic deformation rate tensor
$|Y|$: unit cell volume of micro-scale structure.

Discretizing equation (4) gives an element stiffness equation for determining the characteristic displacement rate in the micro-scale structure. The characteristic displacement rate obtained from the equation corresponds to the perturbed response when uniform macroscopic deformation information is given to the boundary value problem on the micro-scale side. On the other hand, the heterogeneity in the micro-scale is reflected in the macroscopic response from Eq. (6) via the spatial differentiation of the characteristic displacement rate, allowing response solutions on both scales while satisfying consistency on different microscopic/macroscopic scales.

3. Multiscale strength analysis of DP steel

A homogenized elasto-plastic FE simulation code has been developed on the basis of the formulation described in Section 2, and multiscale strength analysis has been performed on DP steel. This section compares the results of the strength analysis with the material testing results in Section 1 and describes the content of the examination of the validity and effectiveness of the development method.

3.1 Analysis model for DP steel microstructure

A mesh model for the unit cell of micro-scale has been created by image-based modeling using the microstructure image in Fig. 1 (a). As shown in **Fig. 3**, the martensite phase has been extracted by binarizing the SEM image. After removing noise, the geometry data of the phase has been created by a peripheral display. After performing mesh division with a quadrilateral bilinear element, one layer has been provided in the depth direction to create a 3D mesh model that has been divided using a hexahedron bilinear element (8-node isoparametric element). This mesh division has resulted in a unit cell FE model with 40,279 elements and 81,014 nodes, both in total.

Assuming that the above unit micro-scale structure is placed periodically, as shown in **Fig. 4**, the unit cell has been given periodic boundary conditions for the perturbed displacement component. The tensile testing results in Fig. 2 have been converted to the true stress–plastic strain relationship, which has been subjected to multipoint

(1) SEM Image (——20μm)　　(2) Binarization　　(3) Outline of martensite phase
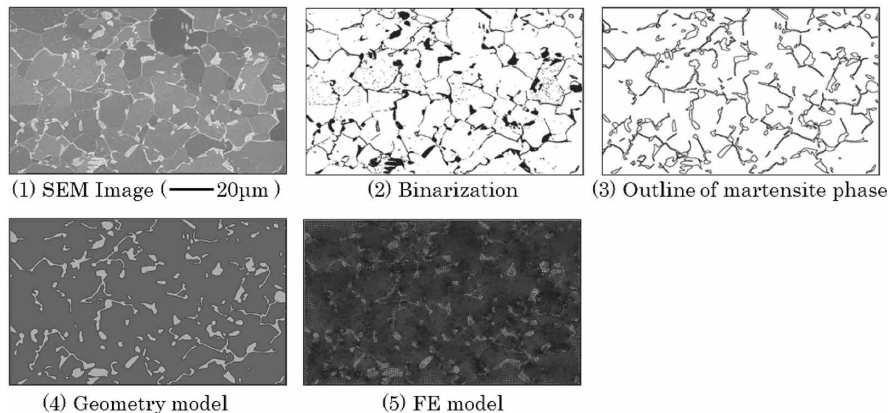
(4) Geometry model　　(5) FE model

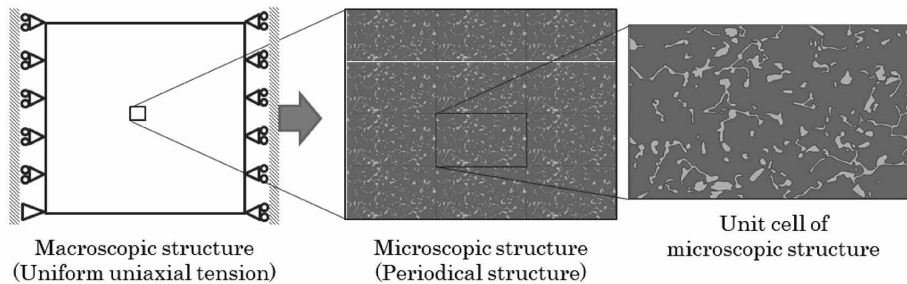Fig. 3 Generation process of FE model for unit cell

Fig. 4 Analytical model

approximation to yield the data for the stress–strain relationship of each phase constituting a unit cell. It should be noted that the damage of each phase has not been considered. In other words, the data obtained by applying the curve fitting with the power-law of the tensile testing result has been used for the stress value after the fracture limit strain of the martensite single-phase material.

On the other hand, the deformation of macro-scale structure was assumed to be uniform. Then, as input data to the boundary value problem of micro-scale structure, macroscopic strain increments equivalent to the uniaxial tension corresponding to the tensile testing have been given to all integration points in the unit cell for each increment calculation step (Fig. 4).

3.2 Results of multiscale simulation

Fig. 5 compares the simulation and experimental results of the true stress–plastic strain curves of the macro-scale structure obtained by the analysis model described in the previous subsection. The solid lines with the plot represent the input data given to each phase. The solid line without plot and the dashed line indicate the experimental result and the simulation result for DP steel, respectively. The tendency for the DP steel to have a stress value and apparent work hardening rate higher than those of ferrite single-phase has been reproduced, providing prediction results for stress-strain relations that are quantitatively close to the actual ones.

As examples of the evaluation of the mechanical behavior in the micro-construction by this simulation, the deformation of the unit cell at the elongation of 20% is depicted in **Fig. 6**, and the distribution of equivalent plastic strain is shown in **Fig. 7**. The distribution of Mises equivalent stress is shown in **Fig. 8**. The martensite phase surrounded by ferrite is elongated in the tensile direction, and the plastic deformation localizes in the ferrite phase near the region where the martensite phase is dense. The internal stress shows a high value in the hard martensite phase (Fig. 8 (a)), and focusing on the
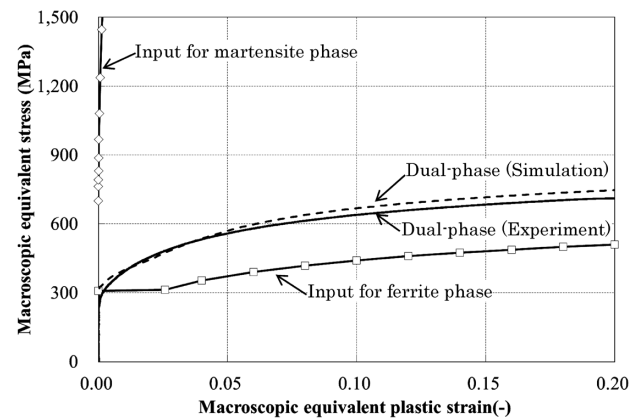
Fig. 5 Macroscopic stress-strain curves obtained by multiscale simulation
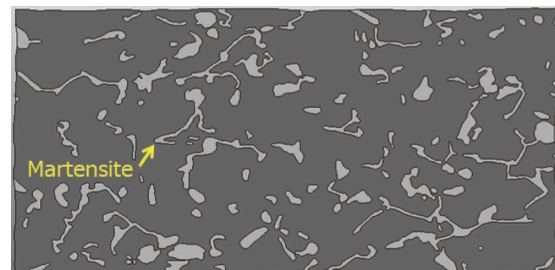
Fig. 6 Deformation of unit cell (at 20% elongation)
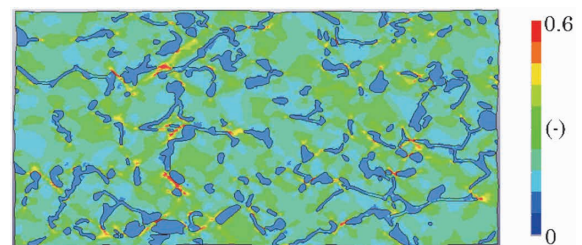
Fig. 7 Distribution of equivalent plastic strain (at 20% elongation)

ferrite phase, the internal stress is confirmed to be high in the region where plastic deformation is relatively large (Fig. 8 (b)). On the other hand, as shown in Fig. 7, plastic strain in the order of several percent occurs even in the martensite phase. In other words, the simulation result suggests that the deformability of the martensite phase is significantly higher in the case of DP steel than in the single-
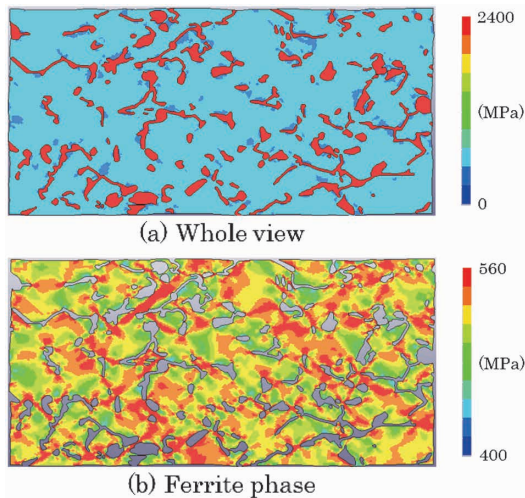
Fig. 8 Distribution of equivalent stress (at 20% elongation)

Fig. 9 SEM image near fracture region in specimen

phase material that fractures in the extremely low strain region.

3.3 SEM observation of specimen after tensile testing

For comparison with the simulation results of the previous subsection, the structure near the fracture surface after the tensile testing (necking part) has been observed for the DP steel specimen to investigate the shape and characteristics of each phase of ferrite and martensite after deformation. As shown in **Fig. 9**, the martensite phase is greatly affected by the plastic deformation effect of the surrounding ferrite phase and is elongated in the tensile direction. This is the same tendency as found in the simulation results. In other words, the results suggest the occurrence of plastic deformation exceeding the fracture limit strain during the tensile testing of the single-phase sample. Macroscopically, the single-phase and DP steel samples have been subjected to the same uniaxial tension. In the martensite phase of DP steel, however, there is a microscopic change to a multiaxial stress field depending on the presence or absence of the surrounding ferrite phase and its deformed state. Therefore, it is presumed that a significant plastic deformation occurred before the fracture compared to the single-phase sample case. The elucidation of the mechanism by which the multiaxial stress field is configured is an issue for the future. A detailed comparative evaluation will be carried out with the help of the newly developed multiscale simulation.

In addition, many microscopic voids have been observed in the ferrite phase near each interface between the phases, mainly in the region where the martensite phase is densely concentrated. It is presumed that these voids have linked to each other and led to the fracture. In other words, the microscopic plastic deformation behavior on the ferrite phase before fracture shows the same tendency as the simulation results of the previous subsection.
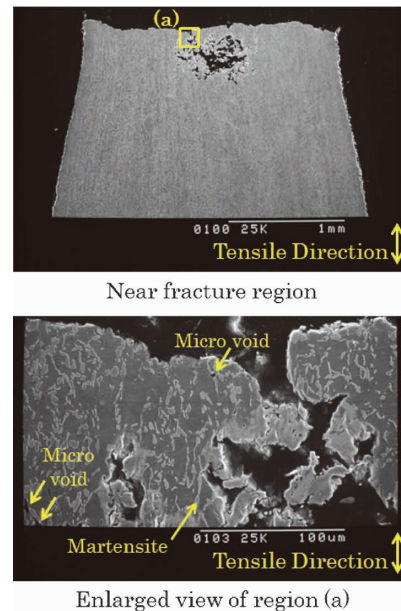
From the above, the multiscale simulation method developed in this study is concluded to be an effective method that allows simultaneous analysis of the microscopic heterogeneous deformation behavior caused by the internal structure in addition to the prediction of macroscopic mechanical properties.

Conclusions

In this study, multiscale strength analysis has been performed by FE simulation of large deformation based on the homogenized elasto-plastic theory for DP steel consisting of ferrite and martensite phases.

For the analysis, material testing data has been obtained for the single-phase sample with characteristics comparable to each phase constituting the DP steel of the benchmark target. Furthermore, the microstructural morphology information inside the material has been reflected in the analysis model by image-based modeling based on the SEM image. The effort has enabled simultaneous analysis of macro stress-strain relationship prediction and microstructural level mechanical behavior, a step toward elucidating the correlation between material properties and internal structure morphology.

Kobe Steel will strive to upgrade this multiscale analysis method so as to evaluate the effect of

microstructural morphology on the strength properties and ductile fracture behavior in practical material.

References

1) T. Ishiguro et al. Tetsu-to-Hagane. 2011, Vol.97, No.3, pp.136-142.
2) H. Shoji et al. Quarterly Journal of JWS. 2015, Vol.33, No.4, pp.341-348.
3) H. Toda et al. Acta Materialia. 2017, Vol.126, pp.401-412.
4) M. Ohata et al. Tetsu-to-Hagane. 2013, Vol.99, No.9, pp.573-581.
5) R. Rieger et al. Archive of Applied Mechanics. 2015, Vol.85, pp.1439-1458.
6) K. Terada et al. Trans. Jpn. Soc. Mech. Eng. (A). 1995, Vol.61, No.590, pp.2199-2205.
7) N. Ohno et al. Journal of the Mechanics and Physics of Solids. 2002, Vol.50, No.5, pp.1125-1153.
8) E. Kurosawa et al. Proceedings of the JSMS annual meetings. 2018, Vol.67, pp.293-294.

Technology for Predicting Residual Stress in Extruded Members of 7000 Series Aluminum Alloy Considering Heat Treatment Process

Hiroaki HOSOI*[1]

*[1] Application Technology Center, Technical Development Group

Abstract

Extruded members of 7000 series aluminum alloy, which has the highest 0.2% proof stress among aluminum alloys, is effective for automotive weight reduction. However, its high sensitivity to stress corrosion cracking (SCC) makes it important to manage residual tensile stress in the members. This paper describes an equation to predict residual stress after artificial aging treatment or after the paint baking process from the residual stress caused by plastic forming during T1 tempering of 7000 series aluminum alloy on the basis of the creep test results of 2 types of newly developed alloys and an extruded material made of standard 7003 alloy. It has been clarified that the artificial aging and paint baking process for extruded members of 7000 series alloy significantly reduce the tensile residual stress caused by plastic forming during the T1 tempering, reducing the risk of SCC.

Introduction

The development of technologies to control CO_2 emissions from automobiles is accelerating worldwide. The weight reduction of structural members is the most basic and effective solution, and Kobe Steel, which has a diverse business and product menu, including steel, aluminum, and welding materials, is also contributing in this area. In particular, for structural members such as bumper reinforcements, side door reinforcements, and side sills, aluminum alloy extruded profiles with hollow cross-sections and high degrees of design freedom can be used, enabling significant weight reduction in comparison to conventional structures combining steel sheets. For these members, Kobe Steel has proposed extruded members made of 7000 series aluminum alloy (hereinafter referred to as "7000 series alloy"), which is expected to have a strength and weight reduction effect exceeding those of 6000 series aluminum alloy (hereinafter referred to as 6000 series alloy), which has been generally used as a structural material. These 7000 series alloy members have been adopted in many automobiles, mainly in the middle-to-high price range.[1)-3)]

The 7000 series alloys, which are Al-Zn-Mg based, have 0.2% proof stress that is exceptionally high compared with those of other alloy systems, but have a susceptibility to stress corrosion cracking (hereinafter referred to as "SCC"), in which the higher the alloy's strength, the greater the susceptibility tends to become.[4)] There are various theories about the occurrence mechanism of SCC, such as the hydrogen embrittlement theory and the anode melting theory, and research is still underway in search of elucidation. From the phenomenal aspect, however, SCC is known to occur when an alloy with high SCC susceptibility is exposed to a corrosive environment under high tensile stress for longer than a specific period. Therefore, when 7000 series alloy is applied to members exposed to corrosive environments, the non-occurrence of SCC must be ensured, and it is essential to manage its cause, i.e., tensile stress. Tensile stresses are roughly classified as tensile stress that resides in the member (residual tensile stress), tensile stress caused by static self-weight, and tensile stress occurring inside a member, caused by various inertial forces during running and road surface input. Of these, the tensile stress caused by the self-weight is generally negligible, and the tensile stress that occurs during driving also has a short loading time, so they are unlikely to be the factors causing SCC. In other words, the stress that requires the most control is the residual tensile stress in each member.

The residual tensile stress in an extruded member of 7000 series alloy mainly occurs during plastic working. The residual tensile stress is relaxed during heat treatment, such as artificial aging in the manufacturing process and the paint baking process at automobile manufacturers, and the residual tensile stress may have decreased by the time of market shipment. This stress relaxation proceeds as creep deformation with the residual stress as the driving force, accompanied by a decrease in elastic strain. The stress relaxation rate depends on stress and temperature and is also considered to depend on dislocation density, i.e., pre-strain. Therefore, a method is required for predicting residual stress after heat treatment, such as artificial aging processing and paint baking, from the residual stress generated by plastic working. In this study, creep testing has been performed by changing the applied stress and pre-strain at temperatures that assume the artificial aging and paint baking for the

extruded material of Kobe Steel's newly developed 7000 series alloys and the standard 7003 alloy. The obtained creep characteristics have been converted into stress relaxation characteristics, which has led to the development of a method using the residual tensile stress after artificial aging and paint baking from the initial residual tensile stress.

1. Manufacturing process of extruded member made of 7000 series alloy for automobiles

Fig. 1 shows a typical manufacturing process for extruded automobile members, such as bumper reinforcements, side door reinforcements, and side sills, made of 7000 series alloy. Fig. 1 separately depicts the process of manufacturing the members in an extrusion factory and the manufacturing process in an automobile factory.

The extrusion factory performs billet casting, homogenization heat treatment, hot extrusion, cooling, and tension straightening to ensure straightness, followed by cutting to the member to its specified length. In the tension-straightening process, a plastic strain of approximately 0.01 is usually applied almost uniformly when cold, and it is considered that the residual stress generated in the cooling process almost disappears in this tension straightening. Subsequently, the bumper reinforcement members and the side-door reinforcement members are subjected to plastic working such as bending and hemming under T1 tempering, which offers superior workability. In the bending process, the cross-sectional shape is kept almost constant. When spring back occurs after the plastic deformation, residual tensile stress up to 0.3 to 0.7 times the 0.2% proof stress occurs in the longitudinal direction in the region from the neutral axis of bending to the outside (tension side) of the bending. In the hemming process, a load in the direction orthogonal to the longitudinal direction is applied to an end of the extruded member, deforming the cross-section. Of the sides that make up the cross-section, the side almost parallel to the direction of load application

is subjected to great bending deformation. Due to this bending deformation, residual tensile stress of approximately 0.5 times the 0.2% proof stress occurs on the inner surface of the bending on the compressive deformation side in the direction orthogonal to the longitudinal direction. Subsequently, artificial aging is applied to achieve the specified mechanical properties. In the case of the artificial aging of 7000 series alloy, 2-step aging[5] may be performed, and the 2nd stage aging, whose temperature is higher, generally involves 3 to 24 hrs. of processing time in the temperature range from 115℃ to 180℃.[6] Finally, machining such as drilling and cutting is performed, and the product is shipped to automobile factories.

In an automobile factory, various mechanical joining methods, such as self-piercing rivets (SPR), are used, in addition to bolt fastening and arc welding, to assemble skeletons, and subsequently, followed by paint baking. Skeleton members, such as side-door reinforcement members, are attached to the skeleton, pass through the paint baking process, and are subjected to the thermal effect. On the other hand, so-called hang-on parts such as bumper reinforcement members are not affected by the heat of the paint baking process because they are attached to the skeleton, which has passed through the paint baking process. The paint baking is divided into a pretreatment process, an electrodeposition process, a washing process, and a drying process. The final drying process uses a high-temperature drying furnace to bake steel sheets, aluminum alloy sheets, sealers, and the like with bake hardenability in addition to the electrodeposition paint. The thermal history of each member is considered to differ significantly since the temperature and time spent in the drying furnace depends on the automobile manufacturer, and the temperature differences among the sites are not negligible. However, even in a steel sheet with a large heat capacity, the temperature of which is the most difficult to raise, the temperature is generally maintained for at least 20 min after reaching 170℃.[7]
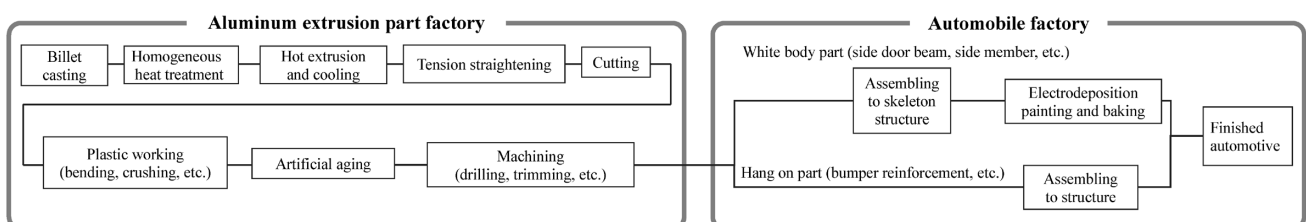

Fig. 1 Typical manufacturing process of 7000 series aluminum alloy extrusion parts for automobiles

2. Creep testing

2.1 Testing conditions

Three types of alloys were selected: Kobe Steel's newly developed alloy A, newly developed alloy B,[2), 3)] and 7003 alloy, a standard alloy selected as a material for comparison. The newly developed alloy A and 7003 alloy are often T5 tempered for use, and the newly developed alloy B is often used after being T7 tempered. **Table 1** summarizes typical mechanical properties in the direction parallel to the extrusion. Hot extrusion was performed using a hydraulic press to produce T1 tempered flat bars, each with a width of 110 mm and a thickness of approximately 3 mm. Then, creep testing pieces with the dimensions shown in **Fig. 2** were collected in the orthogonal direction of the extrusion.

Table 2 summarizes the conditions for the

Table 1 Typical mechanical properties in longitudinal direction

Alloy and temper	Tensile strength (MPa)	0.2% proof stress (MPa)	Elongation (%)	Note
Alloy A-T5	400	350	15	Kobe Steel, Ltd. developed alloy
Alloy B-T7	440	400	14	
7003-T5	315	255	15	Standard alloy

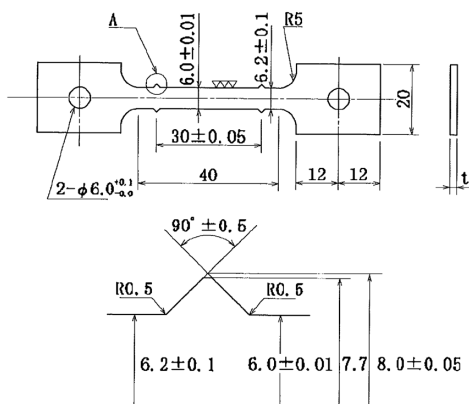Typical value
Longitudinal direction

Fig. 2 Dimensions of creep testing pieces

creep testing. Each creep test was carried out at a temperature assuming artificial aging or a paint baking process. In the creep testing assuming artificial aging, all alloys were T1 tempered before testing. The testing temperature assumed T5 tempering for the newly developed alloy A, T7 tempering for the newly developed alloy B, and T5 tempering for the 7003 alloy. The applied stress was changed from 90 MPa to 250 MPa. The testing time was set at 24 hrs. or less, considering the artificial aging time. Testing conditions were added to investigate the effect of pre-strain on the creep strain rate; that is, the newly developed alloys A and B were pre-strained by an applied stress of 220 MPa, and the 7003 alloy was pre-strained by an applied stress of 150 MPa. After machining each creep testing piece, a nominal strain of 0.005 to 0.1 was given while cold, as a pre-strain to the parallel portion, 30 mm long, of the testing piece by a tensile testing machine. The applied stress and creep strain for the pre-strained conditions accounted for the reduction of the cross-sectional area and changes in the gauge length.

For creep testing under the temperature conditions assuming the paint baking process, the newly developed alloy A was subjected to T5 tempering, the newly developed alloy B was subjected to T7 tempering, and the 7003 alloy was subjected to T5 tempering for the artificial aging before the testing. The testing temperature was 170℃, considered the lower limit of the paint baking process, and the applied stress was changed from 60 MPa to 210 MPa. In order to obtain accurate data of steady-state creep under the conditions of minor creep strain and low applied stress, the testing time is set longer than the time for passing through the drying furnace, with a maximum of 4 hrs. The pre-strained conditions were omitted.

The creep testing method followed JIS Z2271 and included measuring the temporal change of creep strain, in which the elastic deformation is excluded from the total strain.

Table 2 Creep testing conditions

Alloy	Creep test 1（artificial aging process）				Creep test 2（paint baking process）			
	Temper of test pieces	Temperature	Applied stress (MPa)	Note	Temper of test pieces	Temperature (℃)	Applied stress (MPa)	Note
Alloy A	T1	Artificial aging temperature for T5	100, 150, 190, 220	Pre-strain 0.01, 0.02, 0.05, 0.1 conditions are added in 220 MPa.	T5	170	60, 90, 120, 150, 180	-
Alloy B	T1	Artificial aging temperature for T7	150, 190, 220, 250	Pre-strain 0.01, 0.02,0.05, 0.1 conditions are added in 220 MPa.	T7	170	60, 90, 120, 150, 180	-
7003	T1	Artificial aging temperature for T5	90, 120, 150, 180, 200	Pre-strain 0.005, 0.01, 0.03, 0.05 conditions are added in 150 MPa.	T5	170	120, 150, 180, 200, 210	-

2.2 Testing results

Fig. 3 shows the temporal change of creep strain for each alloy with zero pre-strain at the respective artificial aging temperatures. Fig. 4 shows the temporal change of creep strain at the temperature assuming the paint baking process. Under all creep testing conditions, the higher the applied stress, the greater the initial transient creep (primary creep) and the greater the slope of the steady-state creep (secondary creep). Accelerated creep has been confirmed under high applied stress, and some conditions have led to breakage. The creep rates for given applied stress cannot be compared due to the temperature difference in the artificial aging conditions; however, at the temperature assuming the paint tempering process shown in Fig. 4, the rate becomes the highest for 7003-T5, followed by T5

(a) Alloy A -T1 (T5 aging temperature)　　(b) Alloy B- T1 (T7 aging temperature)　　(c) 7003-T1 (T5 aging temperature)
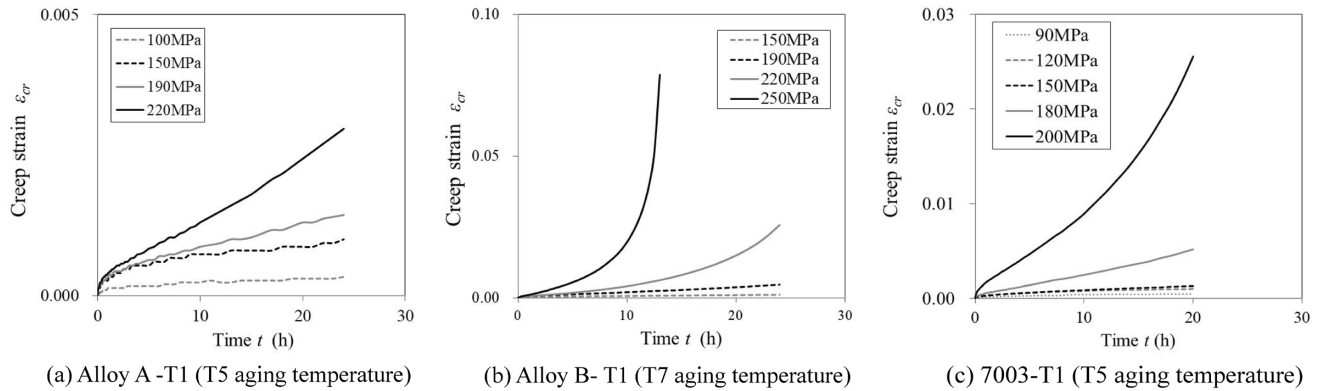
Fig. 3　Creep strain - time relationships at each alloy's artificial aging temperatures in which pre-strain is not applied (Alloy A: artificial aging temperature for T5, Alloy B: artificial aging temperature for T7, 7003: artificial aging temperature for T5)

(a) Alloy A-T5　　(b) Alloy B-T7　　(c) 7003-T5
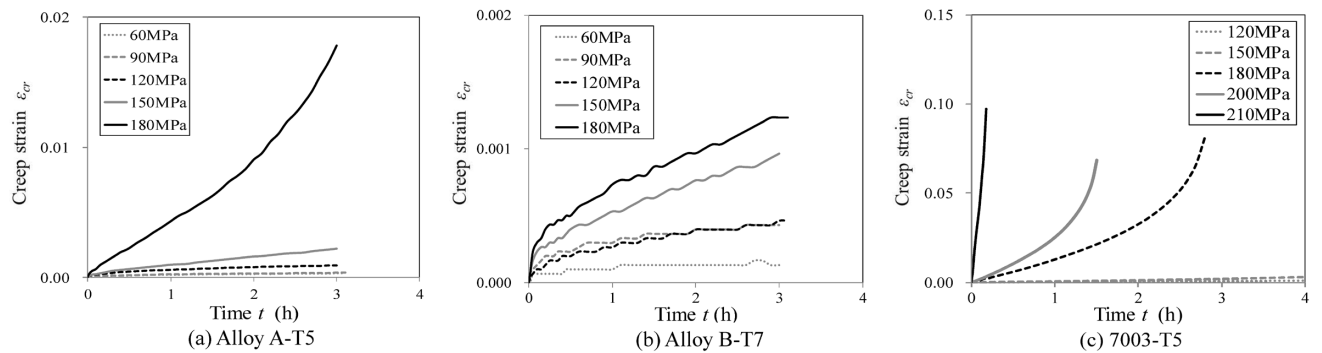
Fig. 4　Creep strain-time relationships at 170℃, which is estimated to be the temperature of the paint baking process (zero pre-strain conditions)

Table 3　Steady state creep rate $\dot{\varepsilon}_{st}$ for each condition (Unit: h^{-1})

(a) Artificial aging temperature

Alloy and temper	Temperature	Applied stress (MPa)								
		90	100	120	150	180	190	200	220	250
Alloy A-T1	Artificial aging temperarture for T5		7.66E-06		1.86E-05		4.33E-05		1.03E-04	
Alloy B-T1	Artificial aging temperature for T7				3.24E-05		1.42E-04		3.14E-04	1.01E-03
7003-T1	Artificial aging temperature for T5	4.00E-05		6.26E-05	6.66E-05	2.08E-04		7.45E-04		

(b) Paint baking temperature (170℃)

Alloy and temper	Temperature (℃)	Applied stress (MPa)						
		60	90	120	150	180	200	210
Alloy A-T5		5.45E-05	5.91E-05	1.67E-04	6.20E-04	4.62E-03		
Alloy B-T7	170	1.08E-05	6.02E-05	8.54E-05	2.11E-04	2.67E-04		
7003-T5				1.08E-04	9.14E-04	1.18E-02	2.43E-02	4.18E-01

Table 4 Steady state creep rate $\dot{\varepsilon}_{st}$ for each pre-strain at artificial aging temperature
(A zero value for pre-strain results in no dimension, $\dot{\varepsilon}_{st}$ 0)

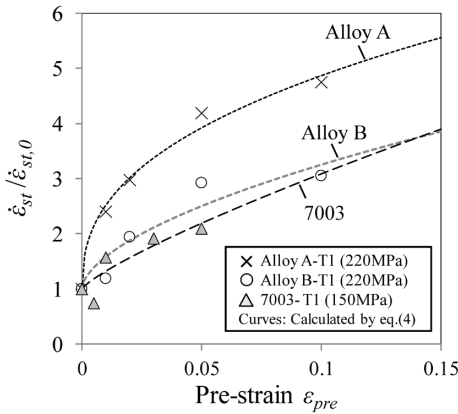| Alloy and temper	Temperature	Applied stress (MPa)	Pre-strain						
			0	0.005	0.01	0.02	0.03	0.05	0.1
Alloy A-T1	Artificial aging temperature for T5	220	1.00		2.40	2.98		4.19	4.75
Alloy B-T1	Artificial aging temperature for T7		1.00		1.19	1.94		2.93	3.05
7003-T1	Artificial aging temperature for T5	150	1.00	0.75	1.57		1.92	2.10	

Fig. 5 Effect of pre-strain on steady state creep rate at artificial aging temperature

tempering of the newly developed alloy A and T7 tempering of the newly developed alloy B, in that order. **Table 3** summarizes the results of extracting the steady-state creep area from the creep strain-time relationship and determining the steady–state creep rate, $\dot{\varepsilon}_{st}$.

Table 4 shows the steady-state creep rate under a different pre-strain at each artificial aging temperature. In Table 4, the steady-state creep rate was rendered dimensionless under the condition of pre-strain 0. **Fig. 5** shows the effect of pre-strain on the steady-state creep rate. Fig. 5 also includes approximated curves based on the approximation expression, Eq. (4), described later. It has been confirmed that the steady-state creep rate tends to increase almost monotonously as the pre-strain increases. For example, compared with pre-strain 0 as a reference, the steady-state creep rate of the newly developed alloy A is approximately 2.4 times for pre-strain 0.01, approximately 3.0 times for pre-strain 0.02, and approximately 4.8 times for pre-strain 0.1. There is also a tendency of differences depending on the alloy types.

3. Derivation of prediction formula for stress relaxation characteristics

Attempts have been made to derive a prediction formula for the stress relaxation characteristics in artificial aging and paint baking processes using the creep testing results of extrusions of the 7000 series alloy. The following assumptions have been made in the derivation:

(a) The relief of residual stress progresses when the elastic strain is replaced with creep strain, which is unaccompanied by shape change (the sum of elastic strain and creep strain is always constant).

(b) Focus is to be placed on the residual stress in the principal stress direction. Other principal stresses do not affect the relief rate of focused residual stress and should be treated the same way as the uniaxial stress state. The stress relaxation is evaluated independently for each point and each principal stress component. Non-linear stress relaxation may cause an imbalance in internal force, causing macroscopic elastic deformation, but its effect should be ignored.

(c) The residual stress dependence of creep strain rate is expressed by the power law. For safe-side evaluation, only steady-state creep will be considered, and neither transient nor accelerated creep will be considered. The power law's proportional constant will take the pre-strain dependence into account.

(d) The effect of pre-strain on the creep strain rate has no dependence on the applied stress or the temperature. The effect of pre-strain before artificial aging is preserved as is in the paint baking process after artificial aging. The pre-strain takes a value of 0 or greater as the equivalent plasticity strain. The effects of strain ratio and strain route should be ignored.

Since the shape is considered not to change due to the creep, the sum of the creep strain rate $\dot{\varepsilon}_{cr}$ and the elastic-strain change rate $\dot{\varepsilon}_e$ is 0:

$$\dot{\varepsilon}_{cr} + \dot{\varepsilon}_e = 0 \quad \cdots\cdots\cdots\cdots\cdots\cdots\cdots\cdots\cdots\cdots\cdots\cdots\cdots (1)$$

The elastic strain ε_e is given by Eq. (2) on the basis of Young's modulus E and residual stress σ_{res} :

Table 5 Parameter list of equations for predicting stress relaxation characteristics

Alloy	Temper	Temperature	A_0 (h^{-1})	m	k	n
Alloy A	T1	Artificial aging temperature for T5	6.66E+03	3.16	9.81	0.404
	T5	170℃(paint baking process)	1.48E+07	3.84		
Alloy B	T1	Artificial aging temperature for T7	9.47E+12	6.55	8.64	0.583
	T7	170℃(paint baking process)	9.25E+03	2.88		
7003	T1	Artificial aging temperature for T5	6.09E+04	3.23	13.43	0.809
	T5	170℃(paint baking process)	3.76E+32	13.28		

$$\varepsilon_e = \frac{\sigma_{res}}{E} \qu*\cdots\cdots\cdots\cdots\cdots\cdots (2)$$

The temperature dependence of Young's modulus is not considered, and Young's modulus at room temperature is assumed. The stress dependence of creep strain rate $\dot{\varepsilon}_{cr}$ shall be expressed by the power law of Eq. (3);

$$\dot{\varepsilon}_{cr} = A(\varepsilon_{pre}) \cdot \mathrm{sgn}(\sigma_{res}) \cdot \left(\frac{|\sigma_{res}|}{E} \right)^m \cdots\cdots (3)$$

wherein m is the stress index (exponential). The absolute value symbol $|\sigma_{res}|$ and signum function, sgn, are used for residual stress σ_{res} to enable handling even when the residual stress is in the compressive direction. In Eq. (3), $A(\varepsilon_{pre})$ is a coefficient corresponding to the pre-strain and gives Eq. (4) that easily expresses Fig. 5 with excellent accuracy:

$$A(\varepsilon_{pre}) = A_0 \cdot (1 + k \cdot \varepsilon_{pre}^{~n}) \quad \cdots\cdots\cdots\cdots (4)$$

wherein A_0 is the coefficient when pre-strain ε_{pre} is 0, and k and n are constants that express the pre-strain dependence. A_0 is determined for each alloy and temperature, and k and n are determined for each alloy. Differentiating Eq. (2) by time and assigning the result to Eq. (1) together with Eq. (3) provide a differential equation for σ_{res}. Solving this equation under the initial conditions ($t = 0$ and $\sigma_{res} = \sigma_{res, 0}$) derives Eq. (5):

$$\sigma_{res}(t) = \mathrm{sgn}(\sigma_{res, 0}) \left\{ |\sigma_{res, 0}|^{1-m} + A_0 \cdot (1 + k \cdot \varepsilon_{pre}^{~n}) \cdot \frac{(m-1)}{E^{m-1}} \cdot t \right\}^{1/(1-m)}$$
$$\cdots\cdots\cdots\cdots\cdots\cdots\cdots\cdots\cdots (5)$$

Eq. (5) allows the evaluation of the changes in residual stress caused by the artificial aging and paint baking process. Also, setting the residual stress after artificial aging to the initial value allows the evaluation of residual stress after the artificial aging and paint baking process. **Table 5** summarizes A_0, m, k, and n determined from the experimental results using the least-squares method.

4. Calculation of stress relaxation characteristics

The stress relaxation characteristics have been calculated using Eq. (5) and Table 5. As mentioned above, the artificial aging conditions are T5 treatment standard conditions for the newly developed alloy A, T7 treatment standard conditions for the newly developed alloy B, and T5 treatment standard conditions for the 7003 alloy. The conditions for the subsequent paint baking have all been set to 20 min at 170℃. Young's modulus E has been set to 70 GPa. The pre-strain ε_{pre} has been set to levels, 0, 0.01, and 0.1. **Fig. 6** shows the change in residual stress due to the artificial aging treatment. **Fig. 7** shows the change in residual stress due to the artificial aging treatment and paint baking process. In Fig. 6, the x-axis represents the residual stress before artificial aging, and the y-axis represents the residual stress after artificial aging. In Fig. 7, the x-axis represents the residual stress before artificial aging, and the y-axis represents the residual stress after artificial aging and paint baking. The y-axis value of each curve and the distance in the y-direction from the function y = x correspond to the amount of stress relaxation caused by the heat treatment.

The stress relaxations caused by artificial aging alone and by artificial aging and paint baking tend to be more pronounced as the residual stress and/or pre-strain increase. The residual stress after heat treatment is almost the same as that before the heat treatment when the residual stress before the heat treatment is low but tends to approach a specific value as the residual stress before the heat treatment increases. This tendency is increasingly pronounced in the newly developed alloy B and 7003 alloy. The asymptotic residual stress depends on the pre-strain; the more significant the pre-strain, the lower the value. The comparison between Fig. 6 and Fig. 7 shows that newly developed alloy B and 7003 alloy have significant stress relaxation by artificial aging and little stress relaxation by the paint baking process.

The newly developed alloy A has little stress relaxation due to artificial aging compared with the newly developed alloy B and 7003 alloy.
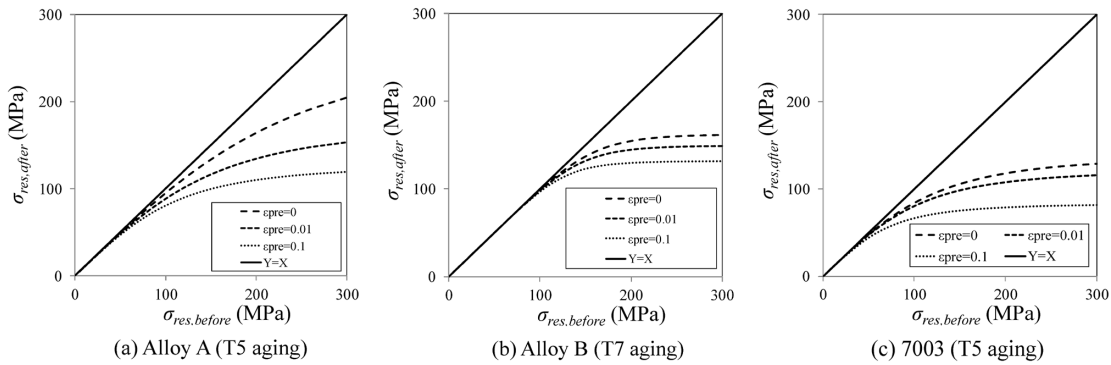
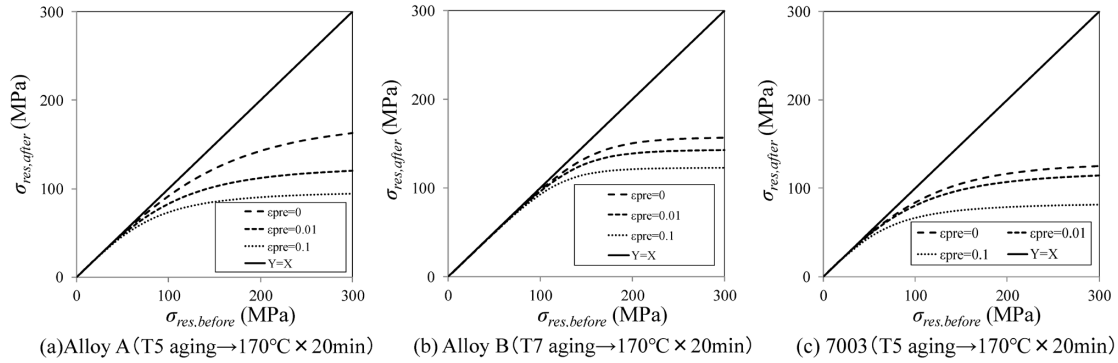**Fig. 6** Changes in residual stress due to artificial aging process (estimated results using Eq. (5))

(a) Alloy A (T5 aging) (b) Alloy B (T7 aging) (c) 7003 (T5 aging)

Fig. 7 Changes in residual stress due to artificial aging treatment and paint baking process (estimate results using equation (5))

(a) Alloy A（T5 aging→170℃×20min） (b) Alloy B（T7 aging→170℃×20min） (c) 7003（T5 aging→170℃×20min）

Conclusions

The extruded materials of two types of Kobe Steel's newly developed 7000 series alloys and the 7003 alloy, a standard alloy, have been subjected to creep testing simulating the temperature conditions of artificial aging treatment and the paint baking process. The test results have been used to develop a method to predict the residual stress after artificial aging treatment and paint baking process from the initial residual stress generated by plastic working during T1 tempering.

(1) Regarding the newly developed alloy A, newly developed alloy B, and 7003 alloy, data have been obtained for the dependence of the creep strain rate on the applied stress and pre-strain under the temperature conditions assuming artificial aging treatment and the paint baking process.

(2) Under various assumptions, prediction formulas were created for the stress relaxation characteristics during artificial aging treatment and paint baking. The stress relaxations by artificial aging treatment alone and artificial aging treatment + paint-baking processing are more pronounced when the initial residual stress is higher and the pre-strain is greater, and the residual stress tends to approach a specific value.

(3) The above results show that the heat treatment (artificial aging treatment and paint baking process) performed on the extruded members of 7000 series alloys significantly reduces the residual tensile stress caused by the plastic working during T1 tempering and contributes to the reduction of SCC risk.

Extruded members using the 7000 series alloy, which has the highest class of strength among aluminum alloys, can contribute to the weight reduction of automobiles, and there are high expectations from automobile manufacturers. In order to meet their expectations, Kobe Steel will continue to focus on technological development that supports practical application by its customers.

References

1) Y. Takagi et al. R&D Kobe Steel Engineering Reports. 2019, Vol.69, No.1, pp.6-10.
2) T. Oka et al. R&D Kobe Steel Engineering Reports. 2004, Vol.54, No.3, pp.51-53.
3) T. Shikama et al. R&D Kobe Steel Engineering Reports. 2017, Vol.66, No.2, pp.90-93.
4) M. Hirano et al. Journal of Japan Institute of Light Metals. 1991, Vol.41, No.7, pp.477-484.
5) Japan Light Metal Association: The fundamentals of aluminum materials and industrial technology. 1985, p.169.
6) Japan Aluminum Association: Aluminum Handbook. 6th edition, 2001, p.10.
7) K. Sugisaki. Journal of the Surface Finishing Society of Japan. 2002, Vol.53, No.5, pp.293-298.

Analysis of Hot Crack and Welding Deformation during One-side Butt Welding Using Idealized Explicit FEM

Tsuyoshi MIWA*1 ・ Dr. Kei YAMAZAKI*1 ・ Kensaku NISHIHARA*2 ・ Dr. Masakazu SHIBAHARA*3

*1 Technical Center, Welding Business
*2 KOBELCO WELDING TechnoSolutions Co., LTD
*3 Osaka Prefecture University (currently Osaka Metropolitan University)

Abstract

This paper reports on the analyses by idealized explicit FEM of hot crack and welding deformation during one-side butt welding. In the hot crack analysis, the incremental value of the plastic strain generated in the brittle temperature range (BTR) and the temperature gradient vector have been evaluated as the occurrence index of hot cracks. By comparing these with the results of welding experimentation, the validity and effectiveness of the hot crack occurrence forecasting by this analysis method have been examined. In the deformation analysis, the actual structure size level has been examined for one-side submerged arc welding (FCB^TM method) and one-side tandem welding (HT-MAG^TM method). It has been shown that the application of these analysis methods has enabled deformation forecasting at high speed and with high accuracy even in large-scale analyses, which hitherto have been difficult.

Introduction

The numerical simulation method has recently been widely used for the mechanical analysis of practical structures. In particular, the finite element method (hereinafter referred to as "FEM") is being introduced in a wide range of fields in design and production. However, the scope of its application to the analysis of welding mechanism is often limited to the vicinity of weld joints, and there are few examples of its application to large-scale analysis. This is because welding is a non-linear transient phenomenon accompanying moving heat sources. Currently, static implicit FEM is generally used to accurately simulate 3D stress/deformation behaviors. In this method, however, memory usage and analysis time become problems as the scale of the analysis increases. In addition, to analyze hot cracking during welding, it is necessary to accurately analyze the displacement and strain behavior of each part at a high temperature using small increments of time and temperature. If the object of analysis extends to welded joints and welded structures, the analysis will inevitably require an enormous amount of time.

An idealized explicit FEM, capable of analyzing at high speed with saved memory, has been applied to large-scale mechanical analysis. This study shows that this method effectively analyzes hot cracking during welding and welding deformations of actual structures.

1. Analysis method based on idealized explicit FEM for hot cracking

1.1 Analysis of welding mechanics by idealized explicit FEM

The following describes the analysis method of idealized explicit FEM, an FEM method for thermal elasto-plastic analysis with an increased scale and speed. Most conventional analyses of welding mechanics assume that the influences of inertial force and damping force are minor and employ the static implicit FEM to solve problems.

$$[M]\{\ddot{u}\}_t + [C]\{\dot{u}\}_t + [K]\{u\}_t = [F]_t \cdots\cdots\cdots\cdots\cdots (1)$$

The conventional method assumes that the influence of the first term (inertia term) and the second term (damping term) in the motion equation (1) are quasi-static phenomena that are negligibly small and solves the overall stiffness equation $[K]\{u\}_t = [F]_t$ expressed in incremental type. On the other hand, the idealized explicit FEM uses the temperature increment obtained by heat transfer analysis as the external force, and the load due to this temperature increment is given to Eq. (1). Solving Equation (1) using optimized mass matrix $[M]$ and damping matrix $[C]$ to increase analysis speed gives the displacement for the next step. In the idealized explicit FEM, the displacement calculation is advanced by solving the calculation step of dynamic explicit FEM, or the step in Equation (1). As the calculation step is advanced, the displacement converges to a constant value, and this step is repeated until the obtained displacement satisfies the static equilibrium, i.e., $[K]\{u\}_t = [F]_t$. After the static equilibrium is reached, the displacement is calculated in the following temperature step. In this way, the displacement calculation in the load step is regarded as a pseudo-dynamic problem, and the analysis is divided into pseudo-time steps for advancement. It should be noted that the static implicit FEM requires solving the stiffness

equation for the entire system, which makes the computational complexity in each calculation step enormous in a large-scale analysis. On the other hand, this idealized explicit FEM does not require solving the overall stiffness equation because it divides the calculation step to proceed with the analysis, and the computational complexity at each calculation step is much smaller than that of the static implicit FEM. Therefore, even if the number of steps to be calculated increases, it is possible to speed up the calculation and save memory.[1] In addition, in the thermal elasto-plastic analysis, the idealized explicit FEM advances the time step using dynamic explicit FEM until its solution reaches a state equivalent to the solution obtained by static implicit FEM, enabling an accuracy of analysis almost the same as that of the conventional method,[2] at a greater scale of analysis compared with the conventional method.[3]

1.2 Overview of hot cracking analysis method

Fig. 1 outlines the occurrence mechanism of hot cracking. Generally, metallic material has a brittle temperature range (hereinafter referred to as "BTR"), where ductility becomes extremely low at a temperature between liquidus and solidus. Hot cracking is considered to occur during the solidification process of welded metal when a significant strain occurs in the BTR with poor ductility. A proposed idea includes defining the minimum strain at which cracking occurs as the limit strain and evaluating the occurrence of cracking in the BTR by the strain acting on the welded metal and the high-temperature ductility curve.[4]

This study relates to the idealized explicit FEM analysis. As shown in **Fig. 2**, the increment of the plastic strain that occurs in the BTR between the liquidus and solidus temperatures, which depend on the material composition in the cooling process and are specified before analysis, is defined as the BTR plastic strain increment. This increment is considered the occurrence index of hot cracking to examine the influence of various factors on cracking.

The solidification morphology near the final solidification zone of welded metal significantly affects the hot cracking resistance. It has been experimentally confirmed that when the meeting angle between crystals is small and butting solidification (head-on collision solidification) occurs, an impurity segregation line appears and promotes cracking.[5] It should be noted that, except for the initial stage of solidification, the solidification growth direction of welded metal is approximately the same as the direction of the
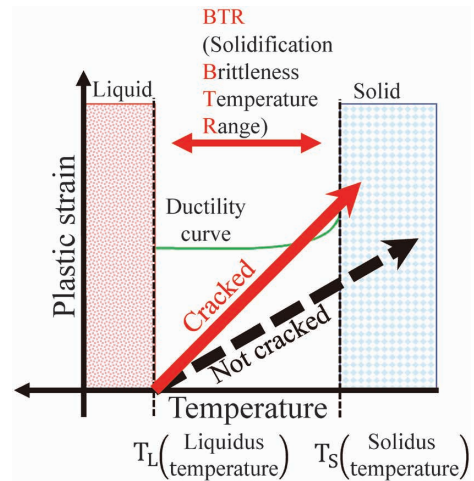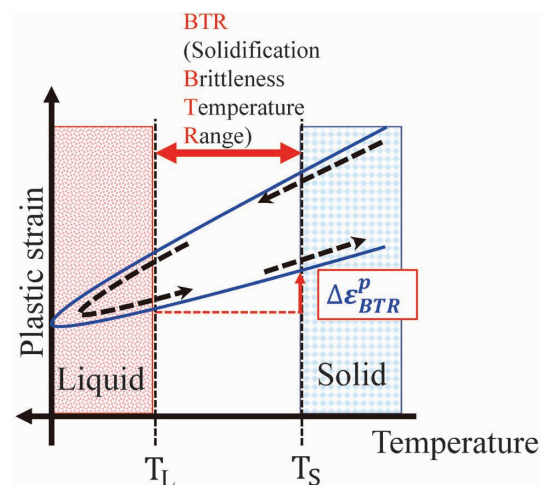

Fig. 1 Mechanism of hot cracking

Fig. 2 Schematic illustration of plastic strain increment in BTR during cooling
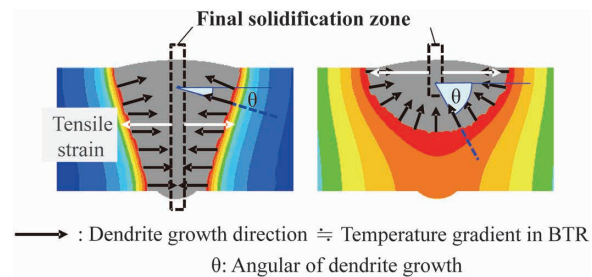

Fig. 3 Schematic illustration of BTR temperature gradient vector

maximum temperature gradient. Therefore, this study considers the solidification growth direction of welded metal and proposes a simple method to determine the direction of solidification growth from the temperature gradient vector obtained by heat transfer analysis. The temperature gradient vector when the liquidus temperature is passed through in the cooling process and transition is made into the BTR is defined as the BTR temperature gradient vector. The direction of this temperature gradient vector is assumed to be the solidification

growth direction. As shown in **Fig. 3**, evaluation is conducted on the angle formed between the temperature gradient vector at the position where the dendrites meet in the final solidification zone and the direction perpendicular to the welding line (hereinafter referred to as the dendrite growth angle).

2. Analysis of hot cracking in one-side tandem welding

One-side tandem welding is a method for realizing automation and high efficiency of welding in the plate joining process in shipbuilding. Regarding this welding, experiments have been conducted to accelerate hot cracking. Also carried out was an idealized explicit FEM to simulate the experiments. The following describes the results.

2.1 Testing method of cracking in one-side tandem MAG welding

Following JIS G 3106 SM490A, a small, simple trolley for automatic welding was used to perform single-side first-pass welding at the flat position on sample steel plates. The shape of the testing plates is shown in **Fig. 4**, the testing conditions are listed in **Table 1**, and the schematic diagram of the welding is depicted in **Fig. 5**. The points ①, ②, and ③ in Fig. 4 will be explained in Section 2.3. In-plane tack welding of 5 mm in height and 50 mm in length was provided to the welding ends and the central region of the welding line. For the stabilization and welding improvement of the molten pool, a cut wire for groove filling (FAMILIARC™ Note 1) M-GRITS,
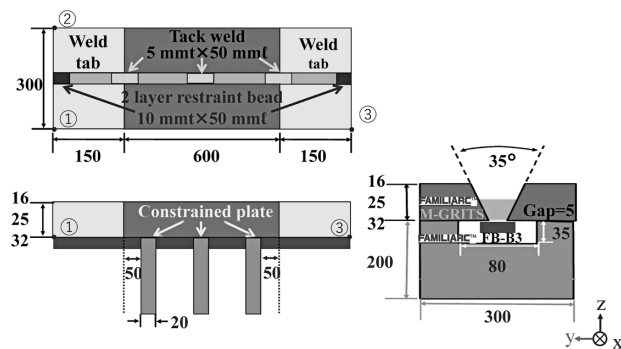
Fig. 4 Shape and dimensions of test plate

Table 1 Welding conditions

Electrode	Polarity	Wire	Welding current -arc voltage	Electrode distance	Welding speed
Leading	DCEP	**FAMILIARC™** MX-100E (φ1.6)	410 A-34 V	40 mm	250 mm/min
Trailing	DCEN	**FAMILIARC™** DW-1ST (φ1.4)	240 A-24 V		

φ1.2 mm × 1.4 mm) was sprayed in the groove. FAMILIARC™ FB-B3 was attached to the entire back side of the welding line as a backing material. Flux-cored wires (hereinafter referred to as "FCW") were used for both electrodes. Arc interference was suppressed by using FAMILIARC™ MX-100E (polarity DCEP) for the leading electrode and FAMILIARC™ DW-1ST (polarity DCEN) for the trailing electrode. The electrode distance was 40 mm, the plate thickness was changed from 16 mm to 25 and 32 mm, and the hot cracking positions along the 600 mm length (excluding starting and runoff web tabs) of this weld were evaluated by X-ray transmission testing.

2.2 Testing results of cracking in one-side tandem MAG welding

Fig. 6 shows the hot cracking test results. The 16 mm thick plate exhibits no hot cracking throughout the overall length of the welding line. The 25 mm thick plate, however, has hot cracking near the tack weld in the groove positioned in the center of the welding line, and the 32 mm thick plate has hot cracking also in places other than the tack weld. **Fig. 7** is a cross-sectional macrograph of the 25 mm thick plate at locations where cracking has occurred and where no cracking has occurred. Hot cracking has occurred in the upper region of the welded metal, and the dendrite growth angle at the cracking occurrence site is small. It should be noted that the distances from the welding metal surface are the same, even for the hot cracking that has occurred on
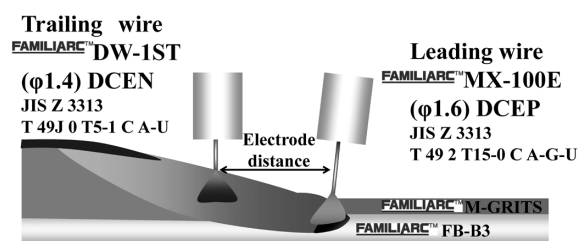
Fig. 5 Schematic illustration of one-side tandem MAG welding method
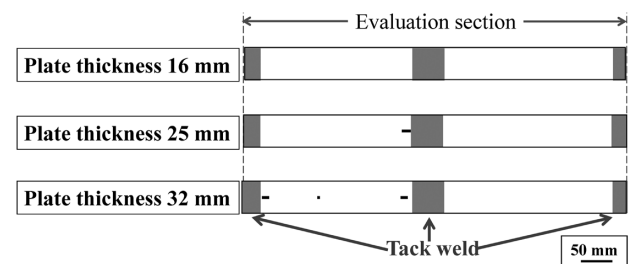
Fig. 6 Hot cracking test results

Note 1) FAMILIARC is a registered trademark of Kobe Steel.

the 32 mm thick plate. This result suggests that, in these welding conditions, the risk of hot cracking is particularly high near the tack weld and above the welded metal for the plate with a 25 mm or greater thickness.

2.3 Analysis of hot cracking in one-side tandem welding by idealized explicit FEM

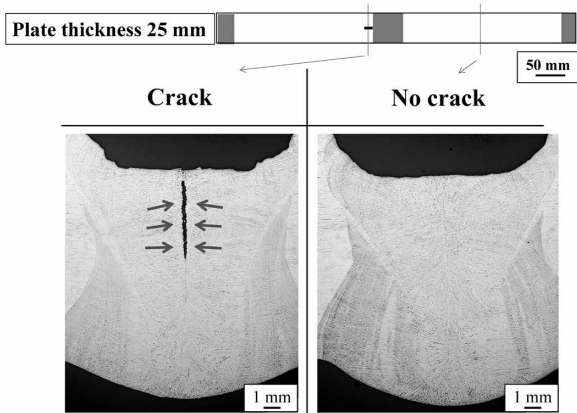An analysis model was created for the test plate shown in Fig. 4. The minimum mesh spacing in

Fig. 7 Cross-sectional macrostructures

the cross-section near the weld was 0.5 mm, the mesh size in the welding line direction was 1 mm, and the number of nodes and element counts in the plate thickness of 25 mm were 1,122,416 and 1,059,664, respectively. The analysis time was 26 hrs. The material constants of SM490A shown in **Fig. 8** were used for the welded metal and base material. The analysis was performed at a BTR of 1,350 to 1,450 ℃. As the boundary condition, the back side was restrained at points ①, ②, and ③ in Fig. 4 in the xyz, xz, and z directions, respectively. This analysis does not take into consideration the influence of the latent heat of solidification.

Fig. 9 shows the dendrite growth angle obtained by the analysis in the central region of the welded metal. Fig. 9 also includes the cross-sectional macrostructure corresponding to the analysis. At the plate thickness of 16 to 32 mm, the dendrite growth angle is negative in the region of 0 to 4 mm from the back bead surface, and the solidification growth direction is toward the lower region of the welded metal. On the other hand, in the region, 4 to 10 mm from the back bead surface, the dendrite growth angle becomes a positive value due to the heat input from the trailing electrode, and the direction of solidification growth is toward the upper region of
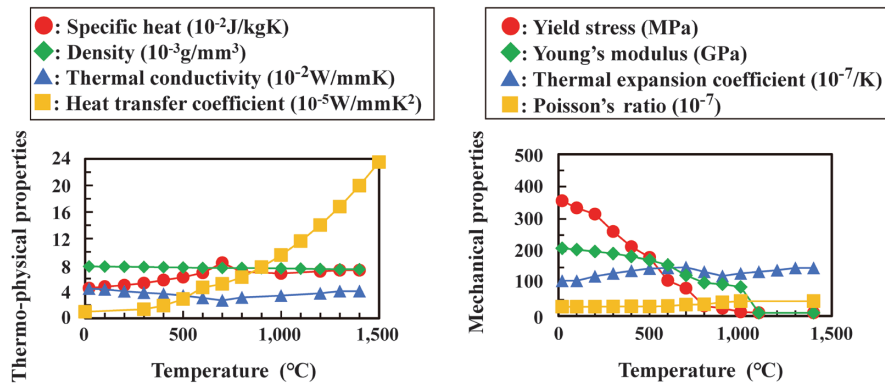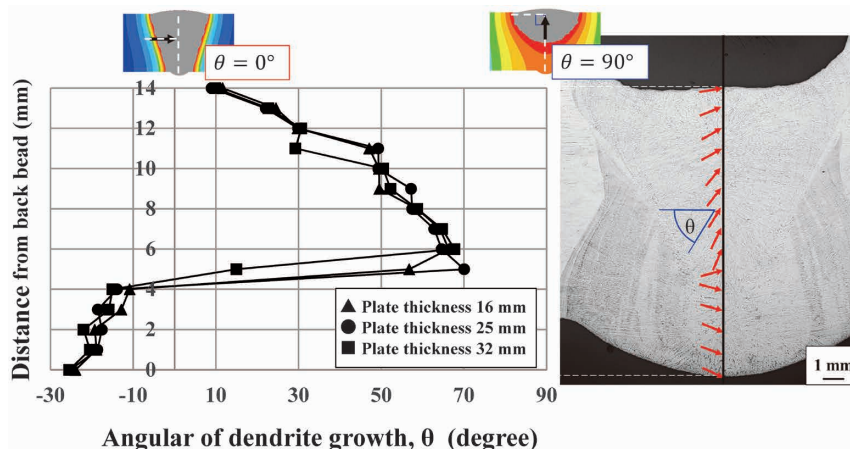

Fig. 8 Material constants

Fig. 9 Angular of dendrite growth

the welded metal. Meanwhile, in the experiment, the dendrite growth angle value is small in the vicinity of the welded metal surface where hot cracking occurred (the region 10 to 14 mm from the back bead), indicative of butting solidification (head-on collision solidification). Therefore, it is considered that the dendrite growth angle obtained by the above analysis roughly expresses the solidification morphology of the welded metal confirmed by the cross-sectional macrostructure shown in Fig. 9.

Fig.10 shows the distribution of BTR plastic strain increments in the cross-section of the welding line for each plate thickness. For the plate thickness of 16 mm, the BTR plastic strain increment does not become extremely large over the entire welding line, whereas, for the plate thicknesses of 25 mm and 32 mm, the BTR plastic strain increment becomes large near the tack weld positioned in the center of the welding line and the region above the welded metal.

Fig.11 shows the distribution of the BTR plastic strain increment and the distribution of the BTR temperature gradient vector in the cross-section of the tack weld (plate thickness 25 mm).

The BTR plastic strain increment in the upper region of the welded metal is shown to be relatively large. Also, the dendrite growth angle is smaller

in the upper region of the welded metal. In other words, the vicinity of the tack weld of a plate with a thickness of 25 mm or greater, where hot cracking occurred, is where the region with a significant BTR plastic strain increment and the region with a small dendrite growth angle overlap in the upper region of the welded metal. The result suggests that this analysis method can estimate the position with a high risk of hot cracking.

2.4 Considerations

A confirmation has been made on the angular distortion behavior obtained by this analysis and the cracking process in the cracked region. **Fig.12** shows the temperature change of the evaluation point near the tack weld caused by the heat-source movement and the transition of the angular distortion in the cross-section perpendicular to the welding line, including the evaluation point. Fig.12 (b) shows the calculation results of the angular distortion
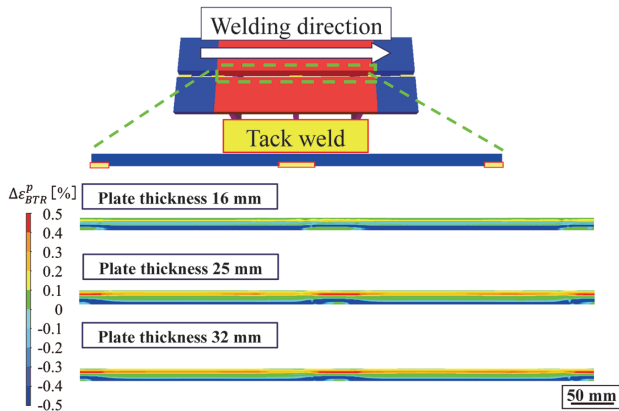

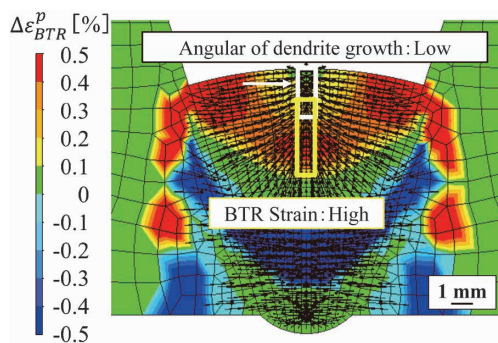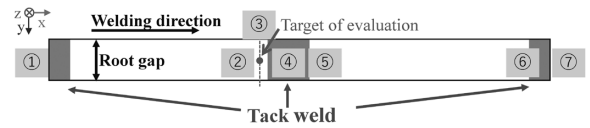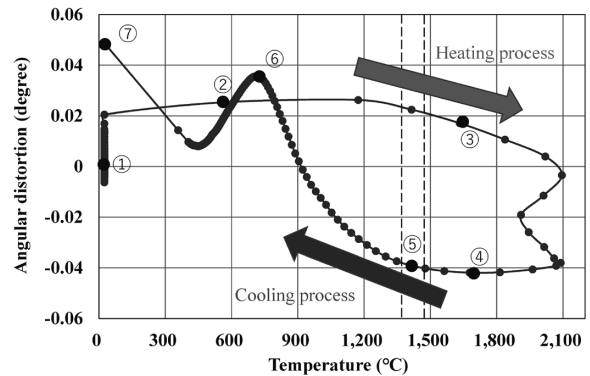Fig.10 Distribution of BTR plastic strain increment in longitudinal section

Fig.11 Distribution of the BTR plastic strain increment and the distribution of the BTR temperature gradient vector in the cross-section of the tack weld

(a) Target point for evaluation and heat source locations

(b) Angular distortion and temperature behavior of near tack weld
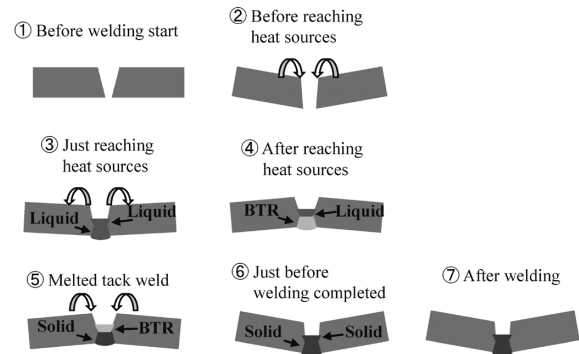
(c) Schematic illustrations of angular distortion behavior at each heat source location

Fig.12 Angular distortion behavior near tack weld portion

behavior when the heat source is positioned at ① to ⑦ in Fig.12 (a), and Fig.12 (c) depicts the schematic diagram. The temperature evaluation point is 2.3 mm from the upper surface of the welded metal where cracking occurred and 10 mm proximal to the tack welding end. The plate thickness is 20 mm, the center of the welding line is the adiabatic boundary surface, and a 1/2 symmetric model with a fixed y direction is used. Here, ① is before the start of welding, and angular distortion has not occurred. In ②, the heat source is located proximal to the evaluation point, and the cross-section of the evaluation point receives the influence of angular distortion of the existing weld. Here, the angular distortion has increased from a positive value because both ends of the base material rise, narrowing the groove angle, as shown in schematic diagram ②. Diagram ③ indicates the state when the heat source reaches directly above the evaluation point. The distortion angle is slightly reduced, and the groove angle is confirmed to have widened. This is attributable to the welded metal being in the liquid phase, and the vicinity of the heat source is thermally expanded. Diagram ④ shows the state after the heat source has passed the cross-section to be evaluated. The process from ③ to ④ causes a large deformation, changing the distortion angle from positive to negative. The welded metal begins solidifying from the lower region of the welded metal formed by the leading electrode. Since the upper region of the welded metal is in the liquid phase, the degree of restraint in the surrounding region is small, and the contribution to deformation is negligible. When the trailing heat source moves forward, and the upper region gradually solidifies, the thermal contraction in the upper region is restrained by the lower region that has already been solidified, leading to angular distortion. This is what causes such a large deformation to occur. Diagram ⑤ depicts the state after the heat source has passed through the tack weld and shows that the evaluation point is in the BTR. Here, the distortion angle tends to increase, and the groove angle narrows, as shown in diagram ⑤. At this time, the evaluation point is subjected to strain in the tensile direction. Then, when the tack weld has completely melted, the restraint due to the tack welding, which has suppressed the deformation of the plate until then and has been released, the strain rapidly increases in the direction of tearing the welded metal. As a result, as shown in Fig.11, the BTR plastic strain increment in the upper region of the welded metal near the tack weld becomes more significant than that in the steady region. Also, a large plate thickness is considered to increase the bending stiffness of the

base material. As a result, the BTR plastic strain increment in the upper region of the welded metal over the entire welding line is considered to become more significant in the plate thickness of 25 mm and 32 mm than in the plate thickness of 16 mm, causing hot cracking. The diagram ⑥ shows the state before the end of welding. The distortion angle increases from ⑤ to ⑥, turning from a negative value to a positive value. Therefore, as shown in diagram ⑥, the groove angle narrows, resulting in a V-type angular distortion. The diagram ⑦ shows the state of cooling to room temperature after welding is completed. Immediately after ⑥, the tack welding of the welding terminal melts, and at that moment, the restraint that suppressed the expansion deformation near the heat source is released. Therefore, in the cross-section to be evaluated, the groove angle expands once from the V-type angular distortion. After the welding is completed, the welded metal contracts, resulting in a behavior in which the groove angle narrows, leading to a final deformed state, as shown in ⑦.

Thus, the influential factors in hot cracking are diverse, complex actions having to do with material type, welding heat input conditions, electrode distance, the groove condition, tack welding condition, restraint condition of the material, and the like. For this reason, even if the appropriate conditions for preventing hot cracking are extracted in the laboratory, hot cracking may occur in actual welding, and many trials and errors are often repeated on-site. This analysis method offers a valuable tool that proactively forecasts the positions with hot cracking risks in actual structures on the basis of simulation techniques introduced in the former section and offers welding guidelines on controlling various influential factors to suppress cracking.

3. Examples of welding deformation analysis aiming at actual structures

The FCB™ Note 2) method, which is one-side submerged arc welding, is widely applied in the plate joining process in shipbuilding. FCB™ is a method of single-sided welding, which includes spreading backing flux (FAMILIARC™ PF-I50R in this study) uniformly on a copper plate, pressing the copper plate against the back side of the groove with an air hose or by some other means, and performing multi-electrode submerged arc-welding using topside flux (FAMILIARC™ PF-I55E in this study) and wire (FAMILIARC™ US-36 in this study).

Note 2) FCB is a registered trademark of Kobe Steel.

On the other hand, the HT-MAG™ Note 3) method, which is two-electrode gas-shielded arc welding, has been developed in recent years to reduce welding deformation in the plate-joining process for thin steel plates (plate thickness of approximately 10 mm).[6] HT-MAG™ is a welding method using a solid wire, FAMILIARC™ MG-50HM, as the leading electrode for deep penetration, and FAMILIARC™ MX-50HM, which is an FCW for improving bead shape, as the trailing electrode. This paper introduces an example of analysis using idealized explicit FEM regarding the deformation reduction effect of HT-MAG™ on FCB™, targeting actual structures.

Fig.13 illustrates the target work for deformation analysis. The analysis has been conducted on the process of constructing a 15.8 m wide block using plates with a thickness of 9.5 mm. The weld length is 12 m, and three welding lines join the plates. The second and third welding passes are set to begin immediately after the end of the previous welding pass. The material constants of welded metal and base material are the same as in Fig. 8. The back sides of the points shown in ①, ②, and ③ in Fig.13 are restrained in the xyz, xy, and z directions,
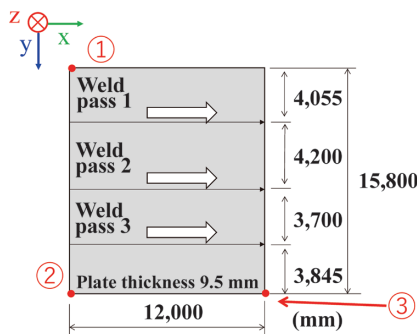
respectively, as the boundary conditions. **Fig.14** shows the cross-sectional shape of welded metal and the cross-sectional macrostructure after welding at the plate thickness of 9 mm in the analysis. The analysis has confirmed that the region heated to above 1,500 ℃ has a morphology similar to that of the cross-sectional macrostructure of the welded metal. **Table 2** shows the analysis conditions. The minimum mesh spacing in the cross-section near the weld is 1.5 mm, and the mesh size in the welding line direction is 10 mm. The number of nodes and element count for the FCB™ are 1,300,605 and 905,554, respectively, and the number of nodes and element count for the HT-MAG™ are 1,257,477 and 963,202, respectively. The welding heat input of HT-MAG™ is approximately 1/3 of that of FCB™, but these one-pass welding methods yield excellent penetration shape. **Fig.15** shows the displacement amount in the thickness direction after the end of the first welding pass, and **Fig.16** shows the amount of displacement in the thickness direction after the end of the third pass (final welding pass). It should be noted that the amount of displacement in the thickness direction is based

Fig.13 Shape and dimensions for deformation analysis
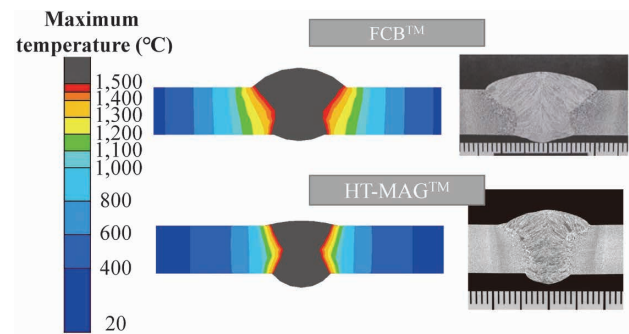
Fig.14 Cross-sectional shape in analysis

Table 2 Analysis conditions of FCB™ and HT-MAG™

	Leading electrode	Trailing electrode 1	Trailing electrode 2	Welding speed	Total heat input	Number of nodes	Number of elements
FCB™	1020 A-33 V	700 A-40 V	700 A-45 V	800 mm/min	6.99 kJ/mm	1,300,605	905,554
HT-MAG™	460 A-32 V	250 A-28 V	—	600 mm/min	2.14 kJ/mm	1,257,447	963,202

Fig.15 Displacement in thickness direction after first pass welding

Fig.16 Displacement in thickness direction after third pass welding

Note 3) HT-MAG is a registered trademark of Kobe Steel.

on the back side of the plate before welding. In addition, for the convenience of calculation, the deformation of the third and fourth plates, which are unwelded, follows the deformation due to the first and second plates' first welding. The same applies to the second welding. HT-MAG™ has resulted in a minor displacement in the thickness direction over the entire plate. **Fig.17** shows the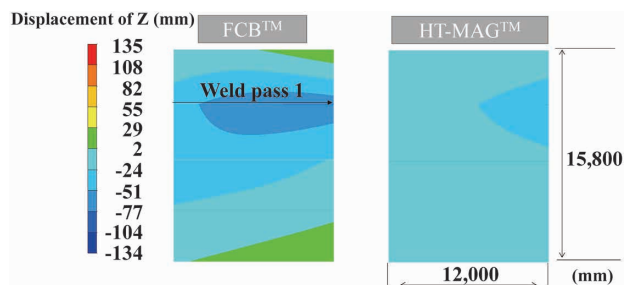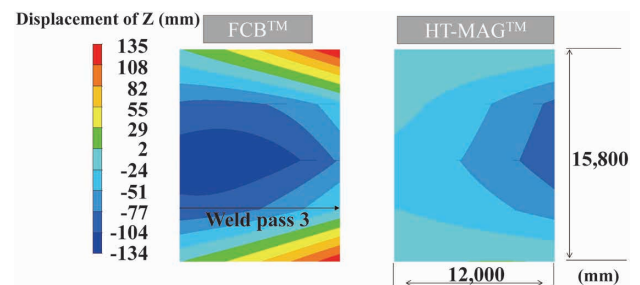 angular distortion at the center of the welding line (X = 6000). Both welding methods have resulted in V-type angular distortions, in which the difference between the maximum and minimum values in the thickness directions is 63 mm for HT-MAG™ and 185 mm for FCB™. The value for HT-MAG™ is approximately 1/3 of the value for FCB™. **Fig.18** shows the longitudinal bending deformation based on the welding start. Since the shape of welding metal differs depending on the welding method, a comparison has been made on the amount of longitudinal bending deformation in the center of the third plate, which is the center of the base material. These welding methods result in different deformation directions; HT-MAG™ causes deformation that descends as it progresses in the welding direction, whereas FCB™ causes a deformation that conversely ascends. Since the reference line cannot be fixed to compare the amount of longitudinal bending deformation, the amount of displacement from the tangent at X = 0 is used for the convenience of calculation. The maximum

displacement from the tangent is 23 mm for HT-MAG™ and 82 mm for FCB™, confirming that the maximum displacement in longitudinal bending of HT-MAG™ is 1/3 that of FCB™ or less.

Although welding deformation is greatly influenced by the welding heat input, the deformation behavior is also affected by other factors such as the number of electrodes, electrode distance, groove conditions, restraint conditions, and welding sequence. The present analysis method has completed the deformation analysis in actual size (analysis example 2 above) in about 157 hrs. The time spent by the static implicit FEM with the same mesh is assumed to be more than 100 times longer. The idealized explicit FEM is regarded as a very effective method in the welding assembly analysis of large-scale structures, which hitherto has been considered difficult.

Conclusions

This paper has reported on hot cracking analysis using idealized explicit FEM and a method for analyzing the welding deformation of actual-sized structures. The results are shown below:
(1) In the hot cracking analysis, the incremental value of the plastic strain and the temperature gradient vector in the BTR have been evaluated as the hot cracking occurrence index. Comparison with the results of the
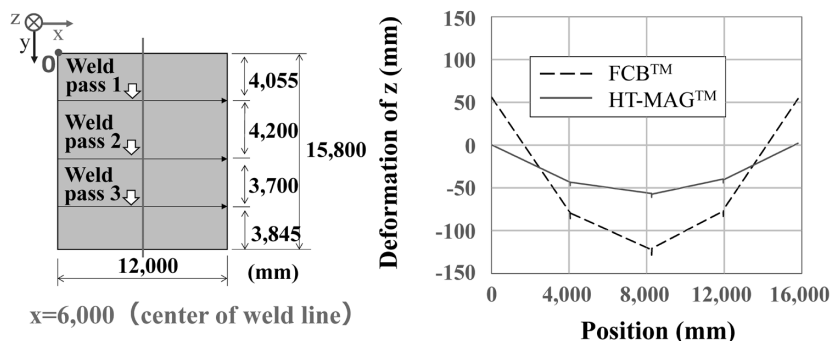

Fig.17 Analysis results of angular deformation
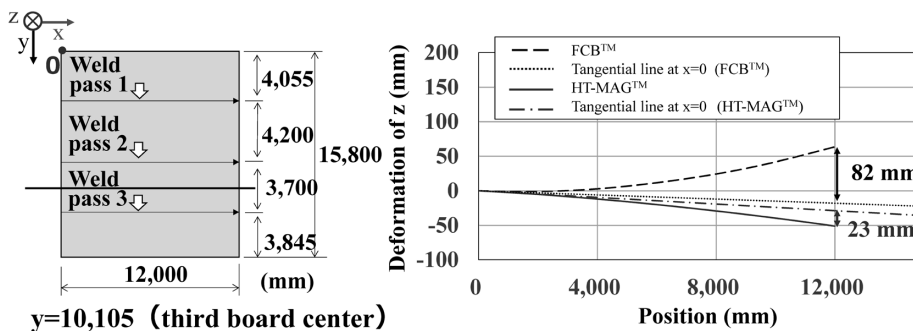
Fig.18 Analysis results of longitudinal bending deformation

welding experiment suggests that the occurrence of hot cracking can be forecasted by applying this analysis method.

(2) In the deformation analysis, FCB™ and HT-MAG™ have been used to conduct a study aiming at actual-sized structures. It has been shown that this analysis method enables high-speed, highly-accurate deformation forecasting even for large-scale analysis, which hitherto has been difficult.

Many welding problems are challenging to solve in the laboratory, "forecasting" and "performance evaluation" by the analysis method shown in this study are also considered to provide some welding solutions. Kobe Steel will strive to contribute to our customers' manufacturing by utilizing various welding solutions.

References

1) M. Shibahara et al. JOURNAL OF THE JAPAN WELDING SOCIETY. 2014, Vol.83, No.7, pp.549-554.
2) K. Ikushima et al. QUARTERLY JOURNAL OF THE JAPAN WELDING SOCIETY. 2013, Vol.31, No.1, pp.23-32.
3) K. Ikushima et al. QUARTERLY JOURNAL OF THE JAPAN WELDING SOCIETY. 2015, Vol.33, No.1, pp.69-81.
4) T. Senda et al. JOURNAL OF THE JAPAN WELDING SOCIETY. 1972, Vol.41, No.6, pp.709-723.
5) T. Kakizaki et al. Preprints of the National Meeting of JWS. 2017-9-11/13, JOURNAL OF THE JAPAN WELDING SOCIETY. 2017, pp.418-419.
6) Y. Yuan. R&D Kobe Steel Engineering Reports. 2018, Vol.67, No.1, pp.5-10.

Battery Degradation Modeling Based on FIB-SEM Image Features Extracted by Deep Neural Network

Dr. Yoichi TAKAGISHI[*1] ・ Dr. Tatsuya YAMAUE[*1]

[*1] Kobelco Research Institute, Inc

Abstract

Attention is being paid to attempts at predicting the degradation and life of lithium-ion batteries (LIBs). This paper focuses on the examination conducted on the features, advantages, disadvantages, etc., of a data-driven prediction model that combines feature extraction and regression by deep learning. Also described is a physics-based model that predicts the degradation progress by electrochemical reaction formula and the like. As a result, it was found that in the physics-based model, the prediction accuracy is high when the degradation phenomena are relatively straightforward, but its application is difficult when the phenomena are complicated or unknown. On the other hand, the data-driven modeling can be done even when the phenomena are not sufficiently clear and is considered to have a great advantage in predicting degradation accurately. Further consideration of the constructed model has also turned out to be useful for elucidating hidden phenomena.

Introduction

Lithium-ion batteries (hereinafter referred to as "LIBs") are installed in various equipment, including information terminals such as notebook PCs and smartphones, as well as transport machines such as electric cars, aircraft, and artificial satellites. Therefore, the technologies for predicting the degradation of LIBs have become extremely important in evaluating equipment life.

The degradation prediction methods for LIBs are being actively studied, including, in addition to the simple rule of thumb (power law, logarithmic law), physics-based models (electrochemical models) in which hypotheses of degradation phenomena are human-made to solve electrochemical reaction formulas numerically, and, more recently, data-driven models for predicting the remaining life from charge-discharge cycle data based on machine learning. **Fig. 1** is a map summarizing these approaches, showing "Hypothesis-driven/Data-driven" on the vertical axis and "Black box/White box" on the horizontal axis. In the hypothesis-driven approaches, various assumptions (simplification or homogenization) are human-made to model the phenomena. In contrast, in the "data-driven" approaches, models that conform to the measured data are established by machine learning. The term "black box" refers to a modeling method of describing a phenomenon only by the relationship between input and output, and "white box" refers to a modeling method that takes into account the details of the phenomenon (here, electrochemical reaction, concentration diffusion, and the like). The empirical methods (second quadrant) as typified by route rules[1] are easy to apply because they use simple functions, but their validity must always be discussed. Physics-based models[2] (first quadrant) are rigorous because they assume physical phenomena. Still, it is challenging to establish a model when the phenomenon itself is complicated or if there is an unknown process.

Recently, the data-driven approach[3] (third quadrant) has been attracting attention. In this approach, machine learning is proactively applied to degradation data under various conditions. Most of these attempts, however, are black-box types not considering the mechanism. Although they show excellent regression/prediction performance, feedback on the cell design and operating conditions is difficult because degradation factors are often hard to estimate.

KOBELCO Research Institute Inc. has recently proposed a white box method that assumes degradation phenomena while taking a data-driven approach (4th quadrant).[4] This paper briefly describes the conventional physics-based model, which models the complex phenomena of degradation, and then describes the data-driven white box model that predicts degradation from the SEM images of electrode cross-sections.
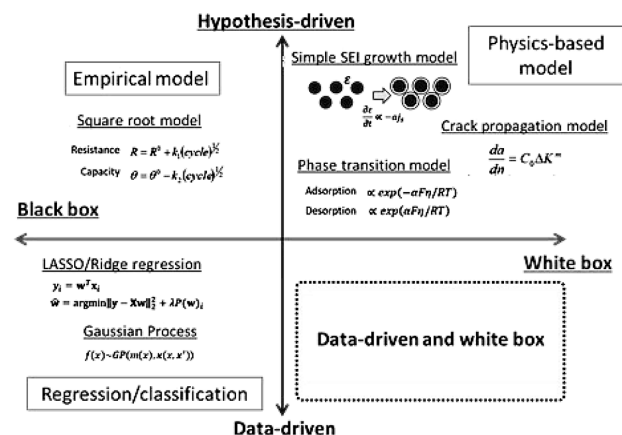

Fig. 1 Approach map for predicting degradation of Li-ion batteries

1. Conventional physics-based model

A method (physics-based model) that considers various degradation phenomena inside electrodes in ordinary or partial differential equations has been suggested as a high-precision method of predicting LIB degradation behavior.[1] **Fig. 2** shows an example of the degradation prediction schemes using a physics-based model. First, various observations, such as SEM and TEM/EELS, are performed to identify critical phenomena in battery degradation. In the case of LIBs, the main degradation phenomena include passivation films (solid electrolyte interfaces, hereinafter referred to as "SEIs") deposited on the active material surface, structural transition in the surface layer of the active material, and inter-particle cracks. Modeling methods such as the "simple SEI growth model," "phase transition model," and "crack propagation model" are suggested, respectively. Next, the formula predicting the temporal evolution of the physical values is established for the identified degradation phenomenon. For example, in the case of SEI film growth, the side reaction current is usually calculated using Tafel's equation. It is often assumed that the growth rate of film thickness is proportional to this current. Finally, the physical values are reflected and converted into battery characteristics (charge-discharge resistance and capacity) to predict the subsequent behavior. The parameters used for the case (hereinafter referred to as "reflection parameters") are determined by fitting them to the actual measurement. The fitting includes sequential optimization by the least square method with regularization term and data assimilation by Kalman filter. **Fig. 3** shows an example of applying the physics-based model to the degradation prediction of a Li(Ni$_{1/3}$Mn$_{1/3}$Co$_{1/3}$)O$_2$-graphite system, a typical configuration of LIB electrodes. A first-order reaction formula expresses the coverage increase for the structural transition layer of the positive electrode active material. Two types of negative electrode SEI films (inorganic and organic) are assumed, and the linearized Butler-Volmer equation is used for the growth rate, in which the growth driving force is regarded to be proportional to the side reaction overvoltage. In addition, the crack growth rate between active material particles or at the interface of the current collector foil adopts an empirical formula based on the Paris rules.

Such an approach can be expected to result in a highly accurate prediction compared with the empirical rule of thumb[2] but requires the assumptions of degradation factors in advance. Therefore, the key is to model the dominant factor
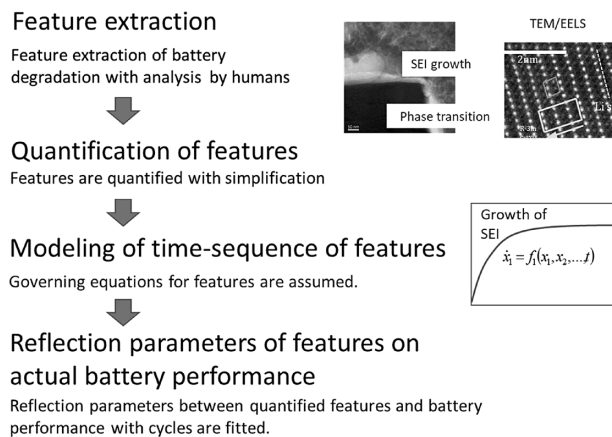
Fig. 2 Typical degradation modeling methods using physics-based models
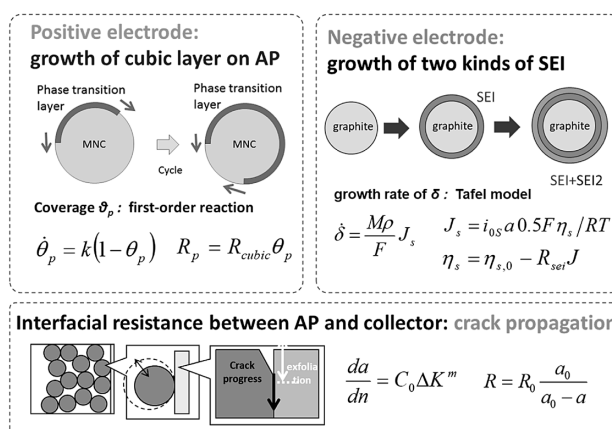
Fig. 3 Typical physics-based model in Li (Ni$_{1/3}$Mn$_{1/3}$Co$_{1/3}$) O$_2$−graphite system

properly. Especially, modeling itself may be difficult if the degradation phenomena are complex or the factors are not sufficiently clear.

2. Data-driven white box model

KOBELCO Research Institute Inc. has recently developed a new degradation prediction technology. This technology comprises extracting statistical feature values by deep learning and image analysis from the cross-sectional SEM image of each degraded state of the electrode and estimating their temporal evolution by the Gaussian process regression. This technology's significant advantage is that the degraded state's feature value is extracted and selected from analysis images, which enables a highly accurate prediction while estimating the objective degradation factors.

Fig. 4 shows the flow of the analysis. As described in the previous section, a data-driven model may be established using only the charge-discharge voltage's cycle/temporal change data. However, despite being of the same data-driven

type, the present approach uses SEM images of the electrode as the input value. It thus is a white box approach expected to enable the feature acquisition of degradation phenomena inside the battery. The main flow is as follows:

① Feature value is extracted by deep learning and visualized in the analysis images (here, the SEM images of the electrode cross-section) of each degraded state to identify the notable feature locations in the degradation image. In addition, image processing is used to score the statistical feature value of degradation indicated by these feature locations. As will be described later, scoring candidates include the area, thickness, and maximum pore diameter of the coated and/or cracked regions.

② A nonparametric regression without prescribing a function form is used to predict how these scores change over time.

③ An artificial neural network determines the reflection parameters that map each score to the actual battery capacity degradation value.

2.1 Acquisition of measurement data

A battery cell for evaluation (prototype coin cell) was created to acquire measurement data for machine learning. The electrodes and electrolyte were made of ordinary materials as much as possible, adopting Li $(Ni_{1/3}Co_{1/3}Mn_{1/3})O_2$ for the positive electrode, SiO-graphite for the negative electrode, and 1M $LiPF_6$(EC: DEC= 1：1) for the electrolytes. The coin cell had a diameter of 10 mm and a capacity of 4.8 mAh.

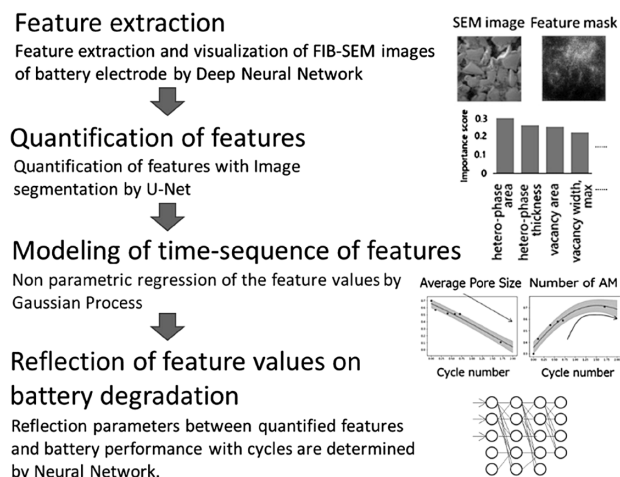Next, after the initial charge-discharge, a charge-discharge cycle test was performed under a temperature of 25 ℃, an upper limit voltage of 4.0 V, a lower limit voltage of 3.0 V, and a charge-discharge rate of 1 C to measure the capacity per each cycle. In addition, the cross-section of the negative SiO electrode in each degraded state was observed by SEM. The maximum number of cycles was set to 100.

2.2 Extraction and selection of feature values from FIB-SEM image

The cross-sectional SEM images of negative electrodes in the initial state and degraded state (after ten cycles) were trimmed and enlarged to $50\,\mu$m squares to establish a degradation state classification model using a convolutional neural network (hereinafter referred to as "CNN"). The CNN feature value extractor was based on VGG16,[5] having a proven track record in ImageNet 1000 class classification. The weight of the neural network was adjusted independently only for the fully connected layer and the previous block. The 4,096-dimensional feature value vector thus obtained was used to carry out classification. As a result, learning approximately 50 images yielded excellent classification characteristics. These flows are shown in **Fig. 5**. Furthermore, the slope of the loss function was backpropagated to the input image to visualize the pixels contributing to the classification.[6]

The mask image, thus obtained, indicates high reactions in relatively vast pores, precipitation films around the active material, and the fine porous region (**Fig. 6**), which leads to an interpretation that these are the regions characterizing the degradation. It should be noted, however, that the vectors representing these degradation characteristics are not interpretable as-is and cannot necessarily be used for degradation prediction. Therefore, this study used U-net,[7] a segmentation method based on deep learning. This technique has been used to perform the regional division for each degraded

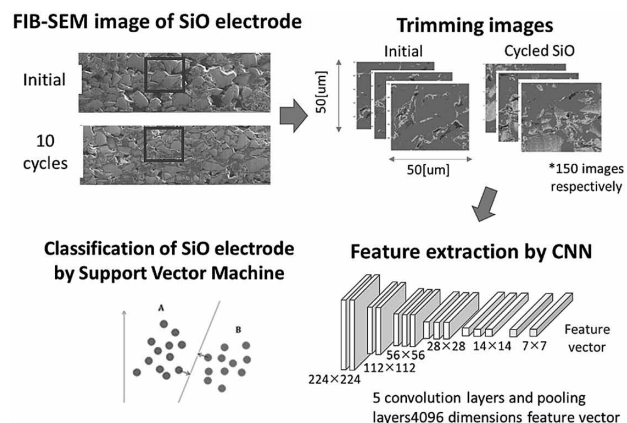Fig. 4 Proposed procedure for data-driven and white box approaches

Fig. 5 Flow of feature extraction and classification of FIB-SEM images using deep learning

state image to identify the precipitation film and porous regions found in the feature locations of the cross-sectional SEM image. At this point, annotation by a skilled SEM technician was carried out to create teacher data. Statistical values on the image such as pore area, surface roughness, and average film thickness of the active material surface layer were calculated and defined as the degradation feature values. Here, segmentation was carried out in four regions: active material, binder/conductive aid, pores, and active material surface layer (**Fig. 7**).
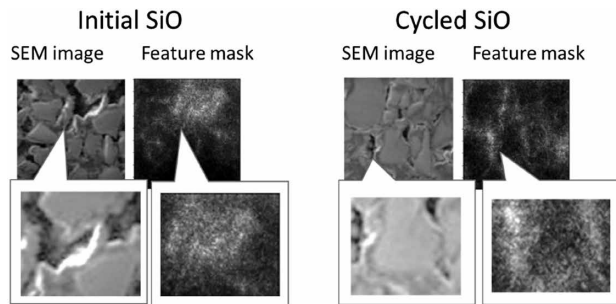
Fig. 6 Visualization of feature locations in cross-sectional SEM images of initial (left) and degraded (right) SiO$_x$ electrodes

2.3 Cycle change of degradation feature values

In Section 2.2, the degradation behavior of battery capacity has been predicted by Gaussian process regression with the number of charge-discharge cycles as the parameter for the temporal change of the quantified degradation feature values. The Gaussian process regression is one of the nonparametric regression methods. It comprises probabilistically interpolating between the data points by the kernel function, thereby adaptively performing regression and prediction from the data characteristics without specifying the function shape. In the present analysis, the Gaussian kernel given by Eq. (1) has been adopted:

$$\kappa_{SE}(x, x') = \theta_f^2 \exp\left(-\frac{1}{\theta_l^2} \|x - x'\|^2\right) \quad \cdots\cdots\cdots\cdots (1)$$

wherein x and x' are data vectors, and θ_f and θ_l are scaling parameters.

Fig. 8 (figures on the left) shows an exemplary regression for the change of degradation feature values with the cycle. This example deals with the

Fig. 7 Segmentation of FIB-SEM images of SiO$_x$ using U-net

Fig. 8 Example of regression of cycle change in degradation features

cycle changes in the entire area of pores, the average area of the active material, the entire area and thickness of the surface region of the active material, the avera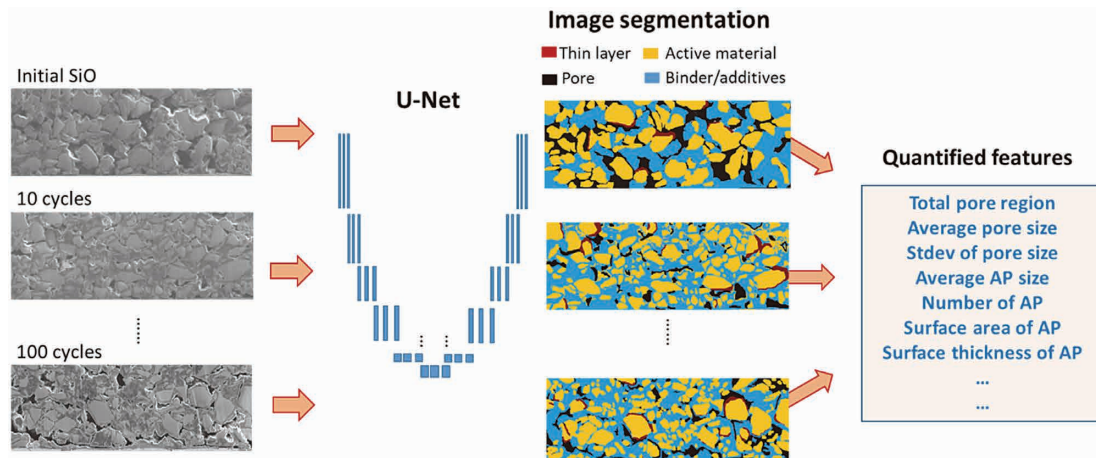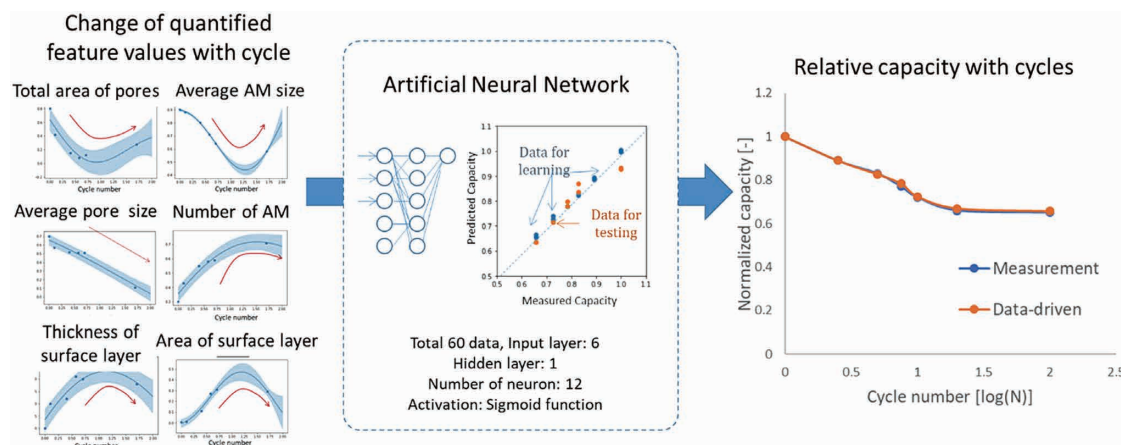ge pore size, and the number of active materials. While the measured battery capacity decreased monotonously, each score fluctuated with the cycle, exhibiting a complicated behavior. For example, the thickness of the active material surface layer does not necessarily increase monotonously with the cycle. In other words, the conventional physics-based model assumes relatively monotonous temporal changes in physical values, but does not necessarily capture the phenomena sufficiently.

The combination of those degradation feature values, subjected to regression, is considered to correspond with the value of electrode degradation. Therefore, the cycle change of each score and the measured degradation value (capacity drop) have been coordinated with the reflection parameters (Fig. 8, center figure). In the present analysis, the coordination has been conducted by an artificial neural network with each degradation feature value as an input and reflection parameter as an output. It should be noted that the reflection parameters have been assumed to have no dependence on the number of cycles. Since the capacity of actual measurement limits the number of data points, the regression has been performed after interpolating the data. Fig. 8 (figure to the right) compares the measured capacity retention rate and the capacity retention rate determined by the regression of the degradation values. The model demonstrates an excellent regression.

2.4 Considerations

The contribution of each degradation feature value has been analyzed from the input layer and the coefficient of the middle-class first layer of the established neural network. **Fig. 9** (a) shows the contribution of each factor to the capacity loss after each cycle. Higher values are indicated by the feature values related to the active material size, such as the average area of active material and the active material density, and by the pore diameter, suggesting their significant contribution. Fig. 9 (b) shows the segmentation images of the negative electrode cross-section after the initial 10 cycles and 100 cycles. As shown, the active material size decreases, and the finer pores increase as the cycle progress. Thus, the degradation is presumed to be mainly due to the pulverization of active material and crack propagation, which enables feedback to the electrode design.

As described, this approach uses the SEM images of the electrode as input and enables degradation prediction for phenomena whose mechanism is not sufficiently clear. It is also noteworthy that the features related to electrode degradation and the main factors have been extracted.

The present analysis uses the cross-sectional SEM images as the only learning data. The model is expected to be further enhanced by including other information (including XPS and TEM-EELS). On the other hand, this approach assumes no physical phenomenon, making the data quality extremely important. The challenge is to secure a sufficient quality and amount of data. In addition, the relationship between the feature values extracted here is nothing more than an inter-phase
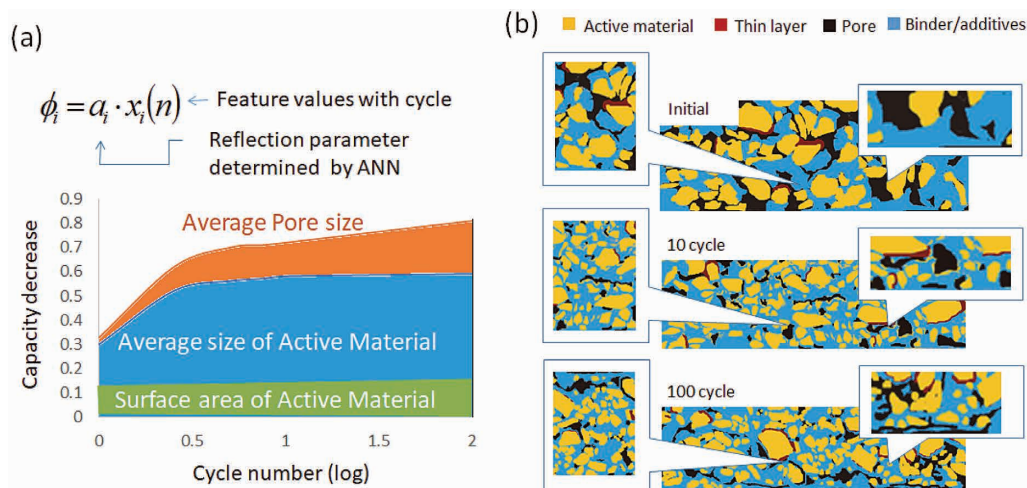

Fig. 9 Cycle change of parameters reflected in actual measurement (a), and segmented FIB-SEM images at initial cycle, after 10 cycles, and after 100 cycles (b)

relationship, and it is necessary to pay sufficient attention to spurious correlation.

Conclusions

This paper has described the degradation prediction technology of lithium-ion batteries and introduced a conventional physics-based model and a data-driven model using machine learning and deep learning, attracting recent attention. The newly developed data-driven white box models enable the modeling of insufficiently clear phenomena and have highly superior degradation prediction accuracy. It has been shown that considering an established model is also helpful in elucidating hidden phenomena. Each of these models has its own character, and it is essential to use them properly in accordance with the phenomena, purpose and findings.

The plan includes establishing highly accurate prediction technology, including extrapolation region by utilizing the SINDy method[8] that estimates the governing equation from data by sparse matrix.

References

1) G. Ning et al. Journal of Power Sources. 2003, Vol.117, pp.160-169.
2) Y. Takagishi et al. International Journal of Automotive Engineering. 2017, Vol.8, No.3, pp.143-148.
3) R. Richardson et al. Journal of Power Sources. 2017, Vol.357, pp.209-219.
4) Y. Takagishi et al. 59th Battery Symposium in Japan. 2018-11-27/29, The Electrochemical Society of Japan, p.209.
5) D. Smilkov et al. SmoothGrad: removing noise by adding noise. arXiv.org e-print archive. 2017, 1706.03825, https://arxiv.org/abs/1706.03825, (accessed on 2020-12-14).
6) K. Simonyan et al. Very Deep Convolutional Networks for Large-Scale Image Recognition. arXiv.org e-print archive. 2015, 1409.1556. https://arxiv.org/abs/1409.1556, (accessed on 2020-12-14).
7) O. Roneberger et al. U-Net: Convolutional Networks for Biomedical Image Segmentation. arXiv.org e-print archive.2015, 1505.04597. https://arxiv.org/abs/1505.04597, (accessed on 2020-12-14).
8) S. L. Brunton. et al. Acad. Sci. U.S.A. 2016, Vol.113, pp.3932-3937.

Technology for Analyzing Solute Carbon in Retained Austenite Using Soft X-ray Emission Spectroscopy

Dr. Aya HINO[*1] · Keiko YAMADA[*1]

[*1] Applied Physics Research Laboratory, Technical Development Group

Abstract

An attempt has been made to measure the microscopic distribution of carbon concentration and to analyze the results using a soft X-ray emission spectroscopy analyzer installed in a scanning electron microscope. The obstacle to accomplishing this was the organic substances adhering to the sample surfaces and acting as contaminants. However, a technique has been established for analyzing while removing contamination by gas-cluster ion beam irradiation, which has enabled carbon distribution measurement focusing on the microstructure in steel. It has also been suggested that this technique may be used for the analysis of the binding state of carbon contained in steel.

Introduction

As the world demands the reduction of CO_2 emissions, it is essential to reduce the CO_2 emitted by transport equipment. Weight reduction is one of the effective means for decreasing the amount of CO_2 emissions from transport equipment such as automobiles.

Reducing the weight of transport equipment, especially automobiles, requires steel sheets with high strength and workability. It is known that transformation-induced plasticity (hereinafter referred to as "TRIP") is effective in improving these properties. Murakami et al. have reported that the strength-elongation balance can be improved by controlling the concentration of solute carbon in retained austenite (retained γ) and dispersing it unevenly.[1] Their study estimates the unevenness of carbon concentration in retained γ from the peak shape of X-ray diffraction (XRD). However, the XRD method for identifying the amount of solid-dissolved carbon can analyze the average carbon content only in crystals with specific structures, but it cannot reveal the microscopic distribution of carbon concentration. Yamashita et al. have reported a method based on field emission electron probe micro-analysis (FE-EPMA) to analyze the carbon concentration distribution in a micro area of steel.[2] They consider that a higher spatial resolution is required to analyze the carbon concentration distribution in micro crystal grains in the order of several hundred nm. This paper reports the results of efforts to establish soft X-ray emission spectroscopy (hereinafter referred to as "SXES") for analyzing carbon at a spatial resolution of 200 nm or smaller in steel to study the carbon concentration distribution in micro crystal grains. Section 1 describes the apparatus configuration of SXES. Section 2 shows the results of examining the analysis conditions of SXES and introduces the contrast resolution and spatial resolution of SXES analysis. Section 3 describes the evaluation results using SXES on the solute carbon distribution in steel. Finally, Section 4 introduces future developments, focusing on the possibility of utilizing high energy resolution analysis, a feature of SXES.

1. Measurement apparatus

X-rays are emitted when inner shell electrons are excited by the electron beam irradiated on a sample surface, causing the transition of the valence band electrons. The SXES is a method for analyzing the energy spectrum in the soft X-ray region. The transition energy of electrons (released X-ray energy) has a value unique to the atomic species. Concerning electron transitions, the electrons that transition from the outermost shell to the inner shell have an energetic spread that reflects the state density of the electrons. From this aspect, it is said that SXES can analyze light elements with peaks on the low energy side and evaluate the bonding state of atoms.[3],[4]

This study uses a scanning electron microscope (SEM)-equipped SXES detector (SEM: JEOL JSM-7100F, SXES: JEOL SS-94000) to perform SXES analysis with high spatial resolution. **Fig. 1** shows the apparatus configuration of the SXES used in this study.[5] An electron beam irradiates the sample, and the soft X-ray in the generated X-rays is separated by a spectral grating and detected by two-dimensionally arranged CCD cameras. The spectral grating and the high-precision CCD cameras enable an analysis of soft X-rays with high energy resolution.

This study aims at establishing a method of quantitative analysis for solute carbon in steel. It is known; however, that an electron beam irradiated during SXES measurement causes contamination-containing carbon on the sample surface.[6] The signal from the carbon contained in the contamination
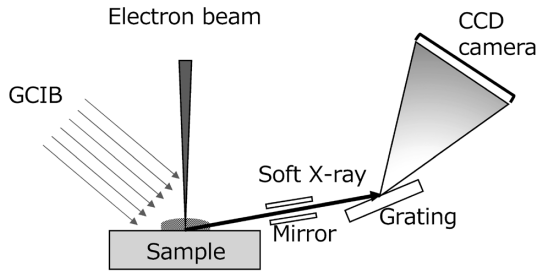
Fig. 1 Configuration of soft X-ray emission spectroscopic analyzer with scanning electron microscope

Fig. 2 Standard curve between 2nd order C Kα integrated intensity and C concentration for Fe-C film

interferes with the measurement. Therefore, a gas cluster ion beam (GCIB) irradiation apparatus (GCIB10S manufactured by IONOPTIKA) has been attached to the SXES apparatus for decontamination,[7]-[9]

The conditions for SXES measurement are acceleration voltage 5 kV and measurement time 5 min/point, unless otherwise specified.

2. Examination of analysis conditions and results of analyzing steel

2.1 Quantitative evaluation of carbon and creation of standard curve

This section evaluates the correlation between carbon content and SXES spectral intensity. Also described is the creation of the standard curve. The samples are Fe-C thin films in which the carbon content in the Fe was controlled. The sputtering method, which facilitates the formation of metastable states, was selected for sample preparation. The samples were formed by simultaneous sputtering with Fe and C targets. The carbon contents calculated from the thickness (volume) and density of the films deposited from the targets were 0.00, 1.00, 1.10, 1.19, 1.40, 1.58, and 2.47 mass%. The intensity of second-order C Kα was obtained from the SXES spectrum of the Fe-C thin films. To this end, the difference in the measurement results between the Fe thin film and the SXES of each Fe-C thin film were taken to derive the integrated intensity of the second-order C Kα. **Fig. 2** shows the relationship between the carbon contents in the samples and the integrated intensity of the second-order C Kα of SXES. A linear relationship was found in the integrated intensity of carbon content and second-order C Kα, allowing the creation of a standard curve.

The standard deviation σ in the simple regression model of the standard curve was determined by Equation (1), and the quantitative accuracy σ_c for the carbon was obtained by Equation (2), assuming the variation in the carbon content of
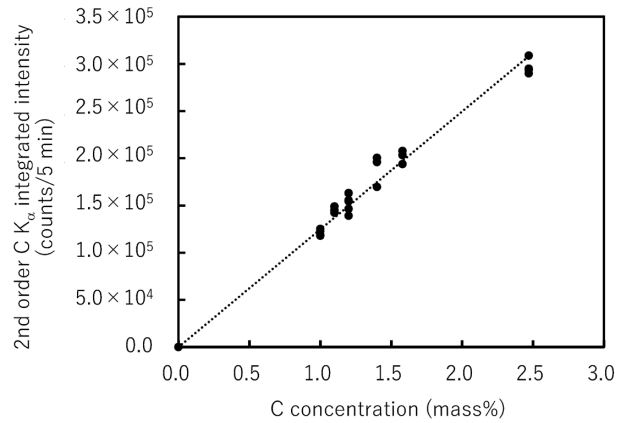
the sample:[10]

$$\sigma = \sqrt{\frac{\sum_{i=1}^{n}[\{y_i - (\hat{\alpha} + \hat{\beta}x_i)\}^2]}{n-2}} \quad \cdots\cdots\cdots\cdots\cdots (1)$$

$$\sigma_c = \frac{\sigma}{\hat{\beta}} = 0.091 wt\% \quad \cdots\cdots\cdots\cdots\cdots\cdots (2)$$

wherein y_i is the count number of second-order C Kα of the i-th data, $\hat{\alpha}$ is the y-intercept of the regression line, $\hat{\beta}$ is the slope of the regression line (count/mass%), x_i is the carbon concentration (mass%) of the i-th data, and n is the number of measurement points.

The quantitative accuracy has turned out to be 0.091 mass%, considering the sample's carbon content variation, showing that the SXES can discriminate the difference in the carbon content of 0.1 mass%.

2.2 Removal of carbon-containing contaminant and line mapping analysis

This section introduces efforts to establish a measuring method that is not affected by carbon-containing contaminants, which adhere during SXES measurement. TRIP steel (steel A) consisting of equiaxial fine grains was used as the sample to examine an analysis method with decontaminating capability. The GCIB, used for cleaning off organic matter, was examined to remove the contaminants that adhere during the measurement.

First, to investigate the decontamination effect of GCIB, line measurement by SXES and SEM observation were performed with and without GCIB irradiation. The measurement was focused on an α grain (carbon concentration 0.02 mass% or less) in steel A, and the influence of the variation in the sample's carbon concentration was excluded. The interval of the line measurement was 150 nm, and the total measurement length was 2 μm.

The SEM images of the sample surfaces after SXES line measurement are shown in **Fig. 3** (a) without GCIB and Fig. 3 (b) with GCIB. The white dotted line in Fig. 3 indicates the location of the line measurement. Fig. 3 (a) shows adhesion around the line measurement location, presumed to be a contaminant. On the other hand, in Fig. 3 (b), no adhesion is observed on the sample's surface.

Fig. 4 shows the second-order C Kα integrated intensity measured by the SXES line measurement. Without GCIB, the integrated intensity of the second-order C Kα increased sharply after the second measurement and did not decrease until the end of the measurement. On the other hand, with GCIB, the second-order C Kα integrated intensity exhibits almost no change. There is almost no distribution of carbon in the α grain used for the measurement, and the increase in the integrated intensity of the C Kα second-order line seen without GCIB is unlikely to be derived from the sample. Thus, the measurement results obtained with GCIB are considered to match the sample properties. The results shown in Fig. 3 and Fig. 4 have led to an

SXES measurement method with GCIB irradiation to remove contaminant that adheres to the sample surface by electron beam irradiation.

2.3 Spatial resolution of SXES analysis in steel

A spatial resolution of several hundred nm or smaller is required to evaluate the carbon concentration distribution in the retained γ of steel. This section describes the evaluation of SXES's spatial resolution in steel. This study aims at a spatial resolution of 200 nm or smaller in steel. The spatial resolution was evaluated by the line measurement of steel A used in the previous section. The SXES line measurement location of steel A is shown in **Fig. 5** (a), and the analysis results are shown in Fig. 5 (b). As shown in Fig. 5 (a), the line measurement location straddles the point where α grain and retained γ grain touch. As shown in Fig. 5 (b), the integrated intensity of the second-order C Kα changes in accordance with the locations between the α grain and retained γ grain in steel A. The concentration variation at the boundary between
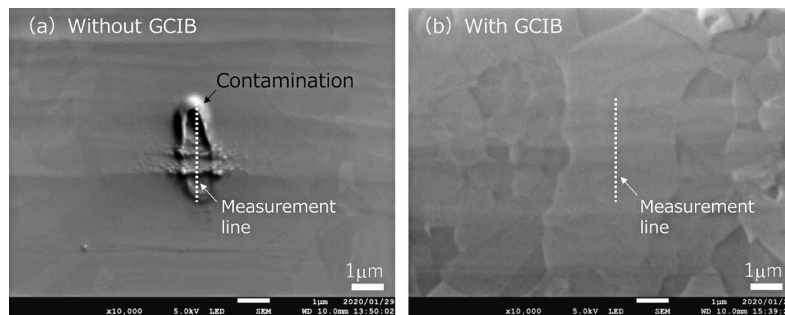

Fig. 3 SEM images of samples (a) without GCIB and (b) with GCIB after SXES line measurements
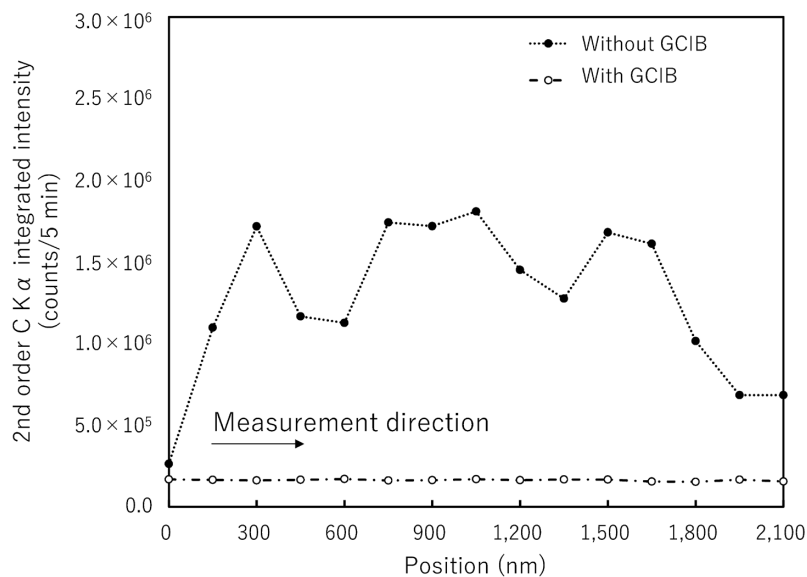

Fig. 4 Variation of 2nd order C Kα integrated intensity of SXES line measurements with and without GCIB
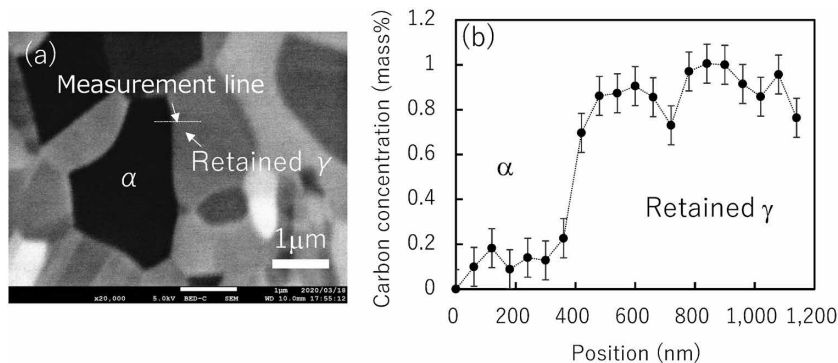
Fig. 5 (a) SEM image and (b) SXES line measurement results of steel A sample including α and retained γ phase

α grain and retained γ grain is described by measurements at 4 points or less. Hence, the actual spatial resolution of SXES during the measurement is estimated to be 180 nm or smaller, which is the distance covered by the four measurement points. This verifies that the spatial resolution in the steel of the SXES analysis measured this time is 180 nm or smaller.

3. Analysis and evaluation of carbon in steel microstructure

The above study has enabled a contrast resolution in steel of 0.1 mass% or smaller and spatial resolution of 180 nm or smaller in SXES analysis. This section describes an attempt to evaluate the microscopic distribution of solute carbon in retained γ in steel. A sample of 1.5 GPa class TRIP steel with a carbon content of 0.4 mass% (steel B) was evaluated for the concentration distribution of solute carbon in the retained γ in the steel microstructure. **Fig. 6** (a) shows steel B's electron backscatter diffraction (EBSD) phase map. In the figure, the red corresponds to α grains, and the green corresponds to retained γ grains. The SXES analysis was performed at the points identified as being in retained γ grains. Fig. 6 (b) shows the frequency distribution of the solute carbon concentrations in the retained γ grains of the steel B. As shown in this figure, the carbon content distribution of retained γ grain in steel B is divided into grains with 1.2 mass% or lower and grains with 1.4 mass% or higher. No clear correlation between carbon distribution and grain size has been found in this measurement.

In the frequency distribution shown in Fig. 6 (b), grains with a carbon concentration close to 0 mass% have been detected, although they are retained γ grains. Usually, no grain with low carbon content remains as a retained γ grain; however, this measurement has detected retained γ grains with low carbon content. The following discusses
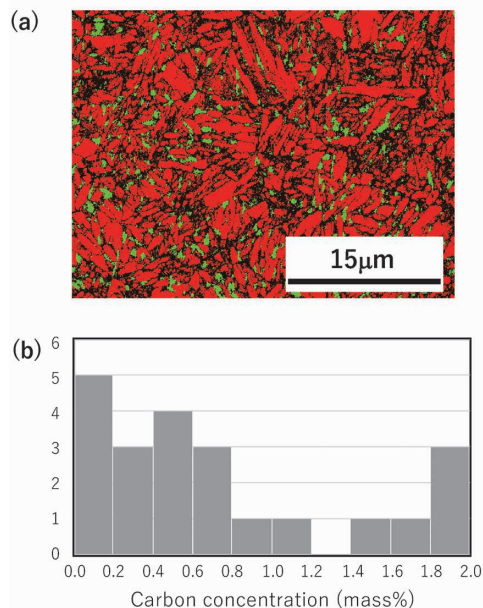
Fig. 6 (a) Phase map image of steel B sample by using EBSD (red: body center cubic, green: face center cubic) and (b) histogram of carbon concentration in retained γ phase measured by SXES

the reason. In the case of SXES measurement, the electron penetration depth into the sample is estimated to be approximately 160 nm from the equation of Kanaya and Okayama.[11), 12)] If a retained γ grain is thin in the depth direction from the sample surface and α grain is present below it, the carbon content is presumed to be intermediate following the volume ratio of the α grain and retained γ grain. Since the distribution of grains in the depth direction of the sample cannot be evaluated, it is considered necessary to improve future measurement and sample preparation methods.

Per the analysis above, SXES-equipped SEM combined with GCIB enables carbon concentration analysis focusing on each retained γ grain in steel, which has yielded a measurement result indicating that the concentration of solute carbon is different for each grain.

4. Prospects: Toward the evaluation of bonding state

Carbon is a typical element that strongly affects steel's properties. The state of carbon in the steel, such as solid solution or carbide, greatly influences delayed fracture and workability. Hence, an SXES analysis has been performed on steel consisting of a lamellar perlite structure (steel C) to evaluate the bonding state of carbon in the steel. **Fig. 7** (a) shows an SEM image of steel C, and Fig. 7 (b) shows its SXES mapping image. As shown in Fig. 7 (a), steel C has a lamellar structure. The SEM image presents a lamellar structure consisting of a bright contrast α layer and a dark contrast Fe_3C layer. This image has been mapped with SXES at 1 min/point, which yielded the image shown in Fig. 7 (b). In Fig. 7 (b), the high-carbo-content region is shown in red, producing a color contour diagram of the lamellar structure corresponding to the SEM image.

The spot measurement results on the solute carbon in steel A's retained γ grain, steel A's α grain, and steel C's Fe_3C in lamellar perlite have been standardized by min/point to produce the spectra shown in **Fig. 8**. The results show that the spectral intensity of approximately 138 eV is the strongest for the solute carbon in the retained γ grain, and approximately 139 eV is the strongest for the carbon in Fe_3C. The spectral shapes differ between the solute carbon in the retained γ and the carbon in Fe_3C. The above indicates that the SXES can detect a spectrum that reflects the difference in the state of carbon in the steel, a possibility of analysis that reflects the bonding state of carbon in steel by SXES.
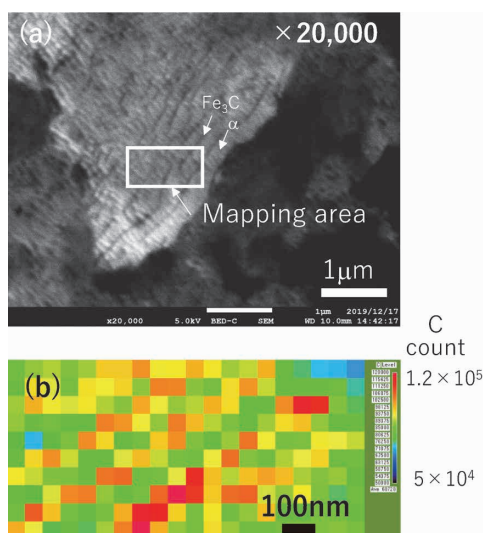

Fig. 7 (a) SEM image and (b) carbon concentration mapping image of lamellar perlite by using SXES
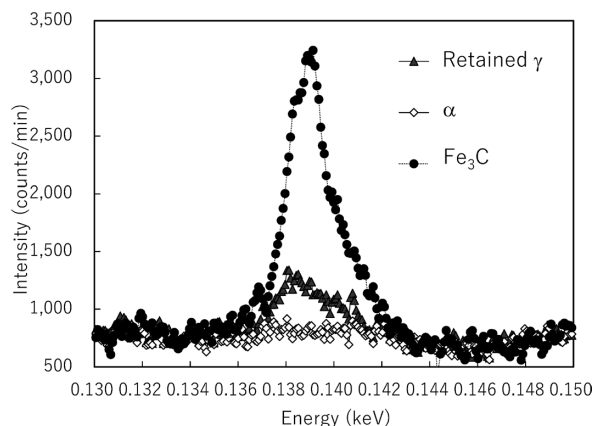

Fig. 8 2nd order C Kα spectra of solute C in retained γ, α, and Fe_3C obtained by using SXES

Conclusions

This study has established a method using SEM with SXES to analyze the steel's microscopic solute carbon quantitatively. The GCIB irradiation has successfully removed contamination containing carbon that adheres to the sample surface during the measurement, a problem in analyzing solute carbon in the steel, offering a clear idea for measuring the carbon concentration distribution in each micro-crystal grain of the steel. Kobe Steel will utilize these analysis techniques to develop materials such as steel.

References

1) T. Murakami. R&D Kobe Steel Engineering Reports. 2019, Vol.69, No.1, pp.29-32.
2) T. Yamashita et al. Tetsu-to-Hagane. 2017, Vol.103, No.11, pp.622-628.
3) M. Terauchi et al. J. Surf. Sci. Soc. Jpn. 2015, Vol.36, No.4, pp.184-188.
4) K. Tanaka. Bulletin of the Japan Institute of Metals. 1976, Vol.15, No.12, pp.753-761.
5) M. Terauchi et al. Handbook of Soft X-ray Emission Spectra Version 5.0. JEOL Ltd., 2019, p.11.
6) M. Amman et al. Journal of Vacuum Science & Technology B.1996, Vol.14, Issue1, pp.54-62.
7) I. Yamada et al. OYO BUTURI. 1997, Vol.66, No.6, pp.559-568.
8) A. Miisho. Tech_library KOBELCO research institute. 2015, No.43 APR, pp.1-3.
9) T. Miyayama. Journal of the Vacuum Society of Japan. 2016, Vol.59, No.5, pp.134-137.
10) T. Kubokawa et al. Statistics. University of Tokyo Press, 2016, p.352.
11) K. Kanaya et al. Journal of Physics D. 1971, Vol.5, No.1, pp.43-58.
12) H. Soejima. J. Surf. Sci. Soc. Jpn. 1984, Vol.5, No.3, pp.351-363.

Technology of Evaluating Minute TiN Inclusions in High-carbon Steel Wire Rod for Advanced Applications

Takashi SUGITANI[*1] • Atsuhiko TAKEDA[*2] • Takehiro SHUDO[*3] • Dr. Hiroki OTA[*4] • Masaki SHIMAMOTO[*5] • Yoshiki TAKEDA[*6]

[*1] Steelmaking Development Department, Research & Development Laboratory, Steel & Aluminum Business
[*2] Wire Rod & Bar Products Development Department, Research & Development Laboratory, Steel & Aluminum Business (currently Wire Rod & Bar Rolling Department, Kobe Wire Rod & Bar Plant, Kakogawa Works, Steel & Aluminum Business)
[*3] Wire Rod & Bar Products Development Department, Research & Development Laboratory, Steel & Aluminum Business
[*4] Steelmaking Development Department, Research & Development Laboratory, Steel & Aluminum Business (currently Steelmaking Department, Kakogawa Works, Steel & Aluminum Business)
[*5] Materials Research Laboratory, Technical Development Group (currently Business Development Department)
[*6] Kobelco Research Institute, Inc.

Abstract

In high-carbon steel wire rod to be drawn into fine diameters, it is necessary to suppress breakage caused by inclusions during the wire drawing process. In the past, breakage in high carbon steel wires was mainly due to alumina inclusions. However, with the higher reduction in the diameter of wires, breakage started from titanium nitride (hereinafter referred to as TiN), which is more minute than alumina, has become remarkable. To study the means for suppressing TiN and to verify their effects, it is necessary to establish both a technique to analyze the ultra-low concentration of Ti dissolved in steel and a technique to evaluate the number of TiN inclusions. This paper describes a method for quantifying concentration of dissolved Ti using a secondary ion mass spectrometer owned by the Kobe Steel group and a technique for evaluating the number of TiN particles, which has been newly developed by applying a chemical extraction method. This paper also describes how the correlation between the number of TiN particles and the frequency of wire breakage has made it possible to predict the quality of extra fine wires.

Introduction

High-carbon steel wires can be strengthened with appropriate heat treatment and cold wire drawing. Hence, they are used as materials that support social infrastructures, such as galvanized steel wires for bridges, steel wires for prestressed concrete (PC), and wire ropes, as well as tire reinforcement materials such as steel cords and bead wires. The application has recently expanded to the material for cutting out silicon wafers from silicon ingots.

With such an expansion of applications, the diameters of product wires are being reduced more and more. In particular, for the cutting of silicon ingots, an extra-fine wire of 50 to 130 μm in diameter is required in order to minimize the cutting allowance. It is known that, in wire drawing, the final process of manufacturing, the presence of non-metallic inclusions (hereinafter referred to as "inclusions") such as alumina (Al_2O_3) sized 30
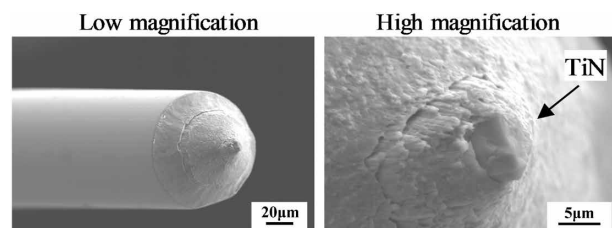

Fig. 1 Fracture surface of extra-fine wire starting from TiN

to 50 μm in the extra-fine wire induces breakage originating in the inclusions.[1] However, recent advances in wire-diameter reduction have revealed that breakage occurs with a titanium nitride (hereinafter referred to as "TiN") sized 5 to 20 μm as the origin (**Fig. 1**), which hitherto has not been the case. As with alumina-based inclusions, breakage originated from TiN also decreases the productivity of wire drawing. Therefore, it is necessary to suppress the formation of TiN in steel as much as possible.

Studying the generation conditions and means of suppressing TiN requires quantitative analysis of the concentration of dissolved Ti and the number of TiN particles in the steel. In particular, ensuring quantitative accuracy becomes challenging when the concentration of dissolved Ti is a trace amount. Hence this paper describes the estimation results for the critical Ti concentration for suppressing the formation of TiN, the origin of breakage. This paper also introduces quantitative analysis means with high precision, including a method for quantifying the concentration of dissolved Ti using a secondary-ion mass spectroscope owned by the Kobe Steel group and a newly developed evaluation technology for quantifying the trace number of TiN particles. Also reported is a breakage test conducted on the high-carbon steel wire manufactured by an actual machine. The results have enabled predicting the rate of breakage from TiN on the basis of the correlation with the number of TiN particles.

1. Generation mechanism of TiN in steel and estimation of critical Ti concentration

Inclusions in steel products are roughly classified into exogenous types mixed from refractory and slag in contact with the molten steel and endogenous types formed by the chemical reaction of components dissolved in the steel. Due to their generation mechanism, the exogenous inclusions are mainly oxide and are relatively coarse. Meanwhile, TiN, which becomes the breakage origin, is considered endogenous, and its suppression requires the elucidation of the generation mechanism.

Hence, a study has been conducted first on the possibility that Ti and N dissolved in molten steel will react to form TiN crystals during the steelmaking process. The solubility product of TiN when TiN is formed by the reaction of dissolved Ti and N is expressed by Eq. (1):[2]

$$\log[\text{Ti}]_L [\text{N}]_L = -14{,}000/T + 4.70 \quad\cdots\cdots (1)$$

wherein: $[\text{Ti}]_L$: concentration (mass%) of Ti in molten steel,

$[\text{N}]_L$: concentration (mass%) of N in molten steel, and

T : temperature (K) of molten steel.

Fig. 2 shows the range of concentration product for gross Ti and gross N measured at each step in the steelmaking process for the general high-carbon steel wire of Kobe Steel. The concentrations of gross Ti and N have been measured per JIS G 1258 and JIS G 1228, respectively. It should be noted, however, that the gross Ti concentrations have been less than the lower limit of quantification, and the concentration products of gross Ti and gross N have been calculated assuming that they are equal to the lower limit of quantification, 10 ppm. The figure also includes the solubility product of TiN calculated by Eq. (1), in which the Ti concentration is 10 ppm, and
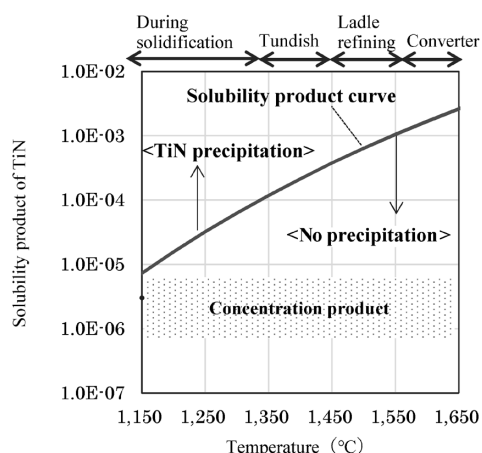

Fig. 2 Relationship between temperature and solubility product of TiN in molten steel[2]

N concentration is the maximum value of the actual measurement.

TiN is formed when the left side of Eq. (1) exceeds the right side, i.e., when the concentration product of Ti and N is higher than the solubility product of TiN in Fig. 2. The actual range of concentration product for Ti and N is below the solubility product curve in both of the temperature ranges, despite the higher-than-actual value for Ti concentration. Therefore, as far as shown in Fig. 2, TiN cannot be formed on the equilibrium calculation.

The TiN in steel products may be precipitated by heat treatment after the casting process. However, the TiN precipitates formed by solid phase diffusion are extremely small in size, generally in the submicron order,[3] and the size does not match the size of the breakage origin, TiN, of approximately 5 to 20 μm, which is the target of evaluation in this paper.

From the above, it is inferred that the breakage origin TiN is formed by the solute condensation associated with the temperature drop during solidification, i.e., the solubility product is locally exceeded by segregation. Hence, a study has been conducted on the mechanism of TiN generation by segregation and the critical Ti concentration that suppresses TiN formation.

Segregation morphologies are roughly classified as micro-segregation occurring in the microregion between dendrites and macro-segregation caused by the widespread movement of solute condensed by micro-segregation due to solidification shrinkage and convection. Scheil's equation[4] can predict the condensation of a solute component by micro-segregation, assuming that the liquid phase has a uniform composition and no diffusion in a solid phase. Bloody-Flemings' equation[5] predicts the same considering the diffusion in the solid phase. These equations suggest the possibility that the TiN solubility product in Fig. 2 is exceeded by segregation as the solidification progresses, even in the case of molten steel with an initial Ti concentration on the order of ppm. It should be noted; however, in the actual operation, it is unlikely that a TiN precipitate with a diameter of 10 μm would form in a micro-segregation region with a diameter of 100 μm, since the mass balance requires hundreds to thousands of times more Ti condensation than the initial concentration. Hence, it has been presumed that the breakage origin, TiN, is caused by macro-segregation rather than micro-segregation. This presumption has led to the examination of the critical Ti concentration to suppress TiN.

The critical Ti concentration was examined by the

following method. First, a high-carbon steel slab was made by Kobe Steel's continuous bloom caster, and the slab's longitudinal cross-section was analyzed by an electron probe micro analyzer (EPMA) to quantify the Mn concentration in the macro-segregation. Next, calculations were performed on the solid phase ratio when Mn condenses to this EPMA analysis value. The segregation calculation model by Ueshima et al.[6)-8)] was used to calculate the solid phase ratio. The parameters shown in **Table 1** were used for the calculation.[6), 9)-11)] Since the target is high-carbon steel in which solidification progresses in the γ single-phase region, Eq. (2) was used to calculate the liquidus temperature:[12]

$$
\begin{aligned}
T_L(^{\circ}\!C) = {} & 1625 - 110[\%C] - 25[\%Si] \\
& + 3[\%Mn] - 35[\%P] - 71[\%S] \\
& - 2[\%Ni] - 7[\%Cr] \quad\cdots\cdots\cdots\cdots\cdots (2)
\end{aligned}
$$

wherein [%M] is the concentration (mass%) of the component M in the liquid phase. The TiN with the stoichiometric composition is assumed to crystallize when the product of [%Ti] and [%N] in the liquid phase exceeds the equilibrium solubility product.[2] After crystallization, it is assumed to exist stably without moving among elements.

Subsequently, the initial Ti concentration was changed stepwise to calculate the segregation concentration of components other than Mn at the above solid phase ratio. These concentrations were used as initial conditions, and the concentration of crystallized TiN in macro-segregation was calculated using the same model. Furthermore, assuming that the TiN particle is a cube each side of which is 10 μm, the crystallized TiN concentration in the macro-segregation was converted into the number of TiN particles to derive the relationship between the initial Ti concentration and the number of TiN particles (**Fig. 3**). Fig. 3 shows that the initial Ti concentration index value for not forming a TiN of 10 μm is 0.5 or less, compared with the standard

Table 1 Parameters for numerical calculation of micro segregation[6), 9)-11)]

Elements	$K^{\gamma/L}$	D^{γ}(m²/s)
C	0.33	7.61×10⁻⁶exp(-1.35×10⁵/(R·T))
Si	0.52	3.00×10⁻⁶exp(-2.51×10⁵/(R·T))
Mn	0.13	5.50×10⁻⁶exp(-1.83×10⁵/(R·T))
P	0.79	1.00×10⁻⁶exp(-2.49×10⁵/(R·T))
S	0.035	7.50×10⁻⁴exp(-2.23×10⁵/(R·T))
Ti	0.07	1.50×10⁻⁵exp(-2.51×10⁵/(R·T))
N	0.48	3.60×10⁻⁵exp(-1.69×10⁵/(R·T))

$K^{\gamma/L}$: Equilibrium distribution coefficient between γ phase and liquid

D^{γ}: Diffusion coefficients in γ phase

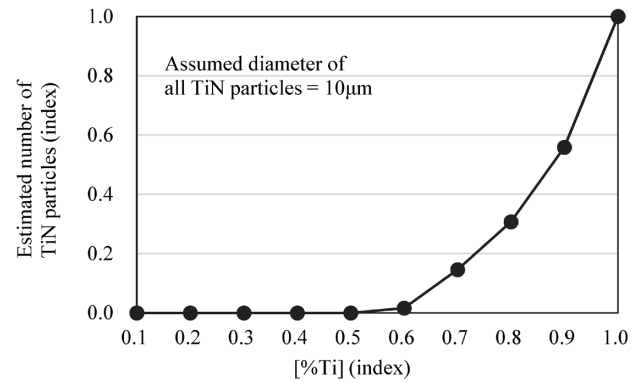R: Gas constant of 8.314 J·K⁻¹mol⁻¹

T: Temperature in Kelvin

Fig. 3 Relationship between initial Ti concentration and number of TiN particles (index)

material, assuming the Ti concentration of 1 for Kobe Steel's general high-carbon steel wire.

2. Method for quantifying trace amount of Ti dissolved in steel

As described in the previous section, the gross Ti concentration in Kobe Steel's high-carbon steel for extra-fine wire is less than the lower limit of quantification according to JIS G 1258 (less than 0.001 mass%), requiring a more precise method of quantifying Ti. It is not the gross Ti concentration, but the concentration of Ti dissolved in the molten steel that affects the thermodynamic conditions for the formation of TiN.

However, the JIS method described above can only analyze gross Ti concentration and cannot distinguish between the Ti dissolved in the steel, and the Ti contained in inclusion particles. Hence, Kobe Steel investigated a method for quantifying the concentration of dissolved Ti using CAMECA's secondary ion mass spectrometry (SIMS) IMS7F owned by the Kobe Steel Group. Hitherto, the Kobe Steel group had conducted quantitative analysis using SIMS for the trace amount of Al dissolved in steel. In the SIMS analysis, it is necessary to eliminate the influence of Al-containing inclusions on the measurement results. To this end, secondary-ion mapping is performed on the sample surface of a steel product to select an area that is not affected by inclusions on the surface. Next, analysis in the depth direction is performed by ion sputtering to confirm that a stable concentration profile is obtained without sudden concentration increase due to inclusions before calculating the trace amount of Al.[13]

The present method adapts this method of quantitatively analyzing dissolved components using the SIMS to the quantitative analysis of dissolved Ti. The results have enabled quantifying

the concentration of Ti dissolved in a range from ppm to ppb. In addition, the operation improvement of the actual machine has enabled quantitative evaluations of whether or not the concentration of dissolved Ti could be reduced to less than the index value determined in the previous section.

3. Development of method for extracting and evaluating TiN particles in steel

Inclusions in steel products are critical factors that affect the quality, making their evaluation key. The methods for evaluating inclusions include a chemical extraction and separation method. In this evaluation method, the base material of steel products is dissolved to extract only inclusions for evaluation. This method allows for three-dimensional evaluation of inclusions and is suitable for grasping their amount, number, and chemical composition. Therefore, many reports have been made.[14)-21)]

However, when multiple inclusions coexist in a sample, an excess of multiple types of inclusions will remain excessively on the filter during inclusion extraction, making the quantification difficult. On the other hand, to extract only the inclusions of the target chemical species to be evaluated, complicated separation procedures and operations must be performed, and depending on the series of operations, the target inclusions may disappear.[21)] In the case of the high-carbon steel wire in this study, there are multiple inclusions such as carbide and oxide in addition to TiN, and it is not easy to quantify TiN by the conventional technique. Hence, as the basis for developing the manufacturing process of high-quality wire, efforts have been made to develop a new technique to evaluate the number of TiN inclusions while considering the components of the steel products and the species of inclusions other than TiN.

TiN is often added proactively to steel products to improve their quality,[22), 23)] and there are many reports on extracting and evaluating TiN in steel products. Examples include the acid treatment method for extracting TiN particles using an acid such as hydrochloric acid or sulfuric acid,[15)] and an electrolysis method that separates TiN by constant current electrolysis using a solution of 10%AA system (10% acetylacetone-1% tetramethylammonium chloride-methanol) and by secondary processing using 10% bromine methanol solution.[24)]

In developing the evaluation method, a decision was made to apply the acid treatment method, which has more evaluation allowance than the electrolysis method. The electrolysis method has a low dissolution tolerance of steel products,[25)] and is not suitable for the trace amount evaluation of TiN originating from Ti mixed at an impurity level, the target of this study. Although it has been reported that TiN dissolves slightly in the acid treatment,[26)] the factor that causes breakage of extra-fine wire is the number of relatively coarse TiN particles sized 10 μm or greater. Hence, a slight dissolution of TiN is considered not to significantly affect the number evaluation, and the acid treatment method using hydrochloric acid has been chosen for the extraction.

SEM observations were performed on the residues on the filter after treatment with hydrochloric acid. The result is shown in **Fig. 4**. Fig. 4 b) schematically illustrates the residues on the filter and is based on the evaluation results from energy dispersive X-ray spectroscopy. The acid treatment does not dissolve inclusions other than TiN, and SiO_2, carbide-derived carbon, and P compounds remain over the entire filter surface in addition to TiN.

Hence, additional processing for extracting only TiN has been studied to establish the process shown in **Table 2**. The feature of the process shown in Table 2 is that TiN is converted to insoluble Ti oxide after the removal of carbon by atmospheric combustion. This process avoids the disappearance of TiN particles caused by the mixed-acid treatment in the back end, whose purpose is to reduce residues other than the Ti-based ones. The only residue on the filter finally obtained by the flow in Table 2 is Ti oxide derived from TiN (**Fig. 5**), and no inclusion of other chemical species is observed.
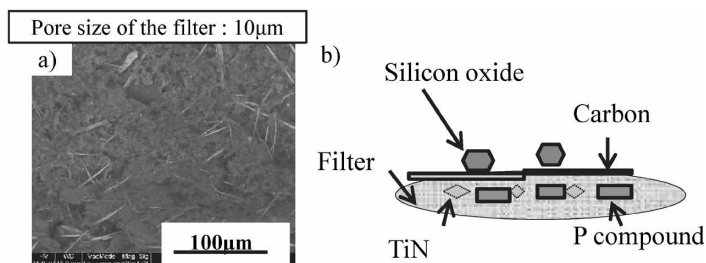

Fig. 4 Residue after acid treatment with HCl (a: SEM Image, b: Schematic diagram of residue on filter)

Table 2 Procedure for evaluation of TiN particle number

Procedure	Purpose
Sample preparation ↓	—
Acid treatments with HCl ↓	Extraction of inclusion
Filtration ↓	—
Heated in air atmospere ↓	Dissolution of residue derived from carbon Modifing of TiN
Treatment with ammonium hydrogen fluoride ↓	Dissolution of residue derived from SiO_2
Treatment with mixed acid ↓	Dissolution of residue derived from Phosphorus
Filtration ↓	—
SEM observation	Evaluation of size and number of Ti oxide derived from TiN

Fig. 5 Ti oxide on filter after mixed acid treatment

Measuring the size and number of inclusions by SEM has enabled quantitative evaluation of the number of TiN particles in steel products.

4. Example of application of analysis evaluation method

The following describes the results of the quality evaluation of production materials at Kobe Steel using the new analytical method described in the previous section.

4.1 Results of evaluation of concentration of dissolved Ti and TiN particle count

When making high-carbon steel wire, multiple alloying elements and auxiliary feedstock are added during molten steel refining. Here, the steel was melted while appropriately controlling the Ti concentration in four batches at Kobe Steel's Kakogawa Works (250 tons/batch) and hot rolled to ϕ5.5 mm by a Kobe Steel wire rod mill.

Table 3 Chemical compositions of production materials

(mass%)

	C	Si	Mn	P	S	Cr	Dissolved Ti (index)
Steel A	1.05	0.20	0.29	0.004	0.005	0.22	1.2
Steel B	1.04	0.19	0.30	0.006	0.006	0.21	1.5
Steel C	1.04	0.20	0.31	0.008	0.004	0.22	1.0
Steel D	1.04	0.19	0.29	0.004	0.005	0.20	0.5

Table 3 shows the chemical compositions of the four batches. The concentration of dissolved Ti was measured by the method described in Section 2 and was confirmed to be quantifiable even if the concentration was less than 10 ppm. Table 3 includes the index value with the concentration of dissolved Ti in Steel C, which is equivalent to Kobe Steel's general high-carbon wire steel, being 1.0, and Steel D corresponds to the material that satisfies the improvement guidelines shown in Fig. 3 of Section 1. It should be noted that the results hereinafter will be described by index value, with Steel C being 1.0.

Fig. 6 shows the relationship between the concentration of dissolved Ti in Steels A to D and the number of TiN particles evaluated by the TiN particle extraction method newly developed. A positive correlation was confirmed between the concentration of dissolved Ti and the number of TiN particles. In addition, no TiN particles were detected in Steel D, which satisfied the guidelines for improving the concentration of dissolved Ti.

4.2 Effect of TiN particles on breakage rate

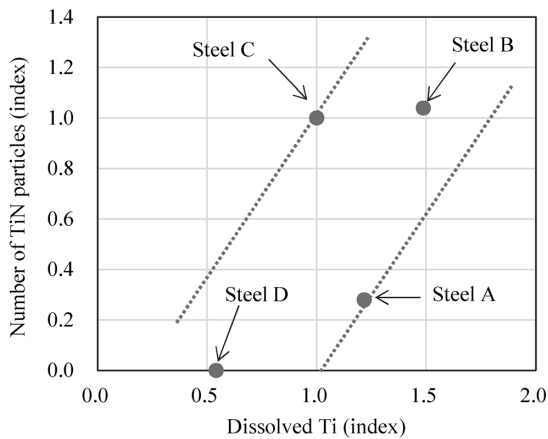The following method has been used to examine

Fig. 6 Relationship between dissolved Ti concentration and number of TiN particles (both of index in Steel C: 1.0)
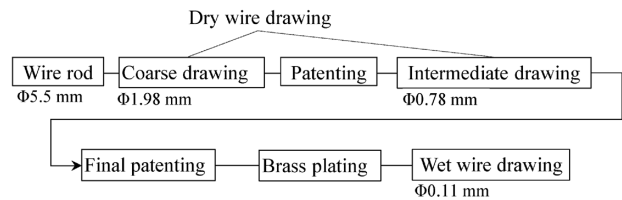

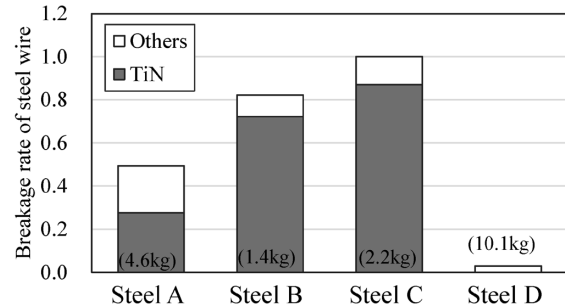Fig. 7 Wire drawing process for evaluation of breakage rate

Fig. 8 Results of breakage rate of steel wire with wet drawing (index in Steel C: 1.0)

Fig. 9 Relationship between number of TiN particles and breakage rate of steel wire caused by TiN (both of index in Steel C: 1.0)

the effect of the number of TiN particles in steel on the breakage rate during wire drawing. **Fig. 7** describes the wire drawing process for evaluating the breakage rate. A wire of $\phi 5.5$ mm was roughly drawn, followed by an intermediate wire drawing to $\phi 0.78$ mm. After the subsequent patenting and brass plating, the wire was wet-drawn to $\phi 0.11$ mm to evaluate its breakage rate. Typical low-angle dies were used for the first 19 passes of wet drawing, and high-angle dies were used for the final 5 passes to increase the shear stress around the TiN particles to facilitate the evaluation of the effects of the number of TiN particles.

Fig. 8 shows the evaluation results for the breakage rates of Steels A to D. The numbers in parentheses indicate the wire drawing evaluation value. In the case of frequent breakage rates, it gives higher reproducible evaluations with fewer samples than for infrequent breakage rates. Therefore, the evaluation value was changed as appropriate, and the breakage results were converted to the number of breakages per 100 km of line drawing distance to exclude the effect of the difference in the evaluation value. The breakage origin was investigated and evaluated for broken wires, distinguishing between TiN and other inclusions.

In this wire drawing test, a fractographic study was conducted after the breakage to confirm that the breakage from TiN origin predominates in Steels A, B, and C. The result proves that this wire drawing condition evaluates the breakage characteristics with TiN origin. In addition, the breakage rate with TiN origin in Steel A, B, and C was 0.3 to 0.9, whereas the breakage with TiN origin was zero in Steel D, whose index value for the concentration of dissolved Ti was 0.5 or less than that of Steel C. This result supports the validity of the improvement guideline shown in Fig. 3 of Section 1.
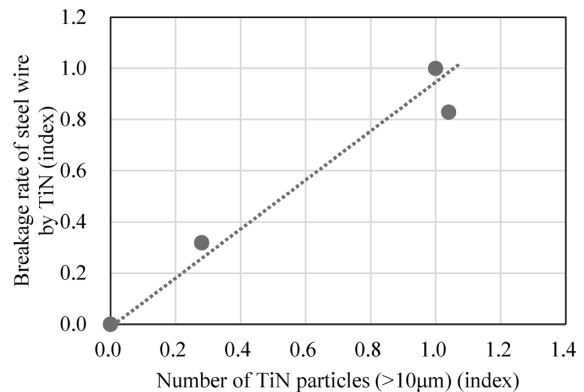
Fig. 9 shows the correlation between the number of TiN particles in Steels A to D and their breakage rate. The number of TiN particles was counted by applying the TiN particle extraction and evaluation method described in Section 3. A linear correlation is observed between the two, and quantifying the number of TiN particles in steel by the newly developed method has enabled the prediction of the breakage rate with TiN origin in the wire drawing process of extra-fine wire.

Conclusions

As the diameter of high-carbon steel wire is reduced, the breakage originating from TiN has become apparent. In order to suppress this breakage, a quantitative analysis technology for dissolved Ti in steel using SIMS and technology for evaluating TiN particle count applying the acid treatment method

have been established.

The concentration of Ti dissolved by the trace amount, the number of TiN particles, and the breakage rate were evaluated for the materials manufactured. These results have revealed that the number of TiN particles in the steel decreases with the reduced trace amount of dissolved Ti, suppressing the breakage from TiN. Besides, the correlation between the number of TiN particles and the breakage rate has enabled the prediction of the quality of extra-fine wire of high-carbon steel by the newly developed TiN particle count evaluation technology.

References

1) T. Minamida et al. R&D Kobe Steel Engineering Reports. 2000, Vol.50, No.3, pp.31-35.
2) S. Amano et al. Tetsu-to-Hagane. 2014, Vol.100, No.4, pp.548-555.
3) S. Matsuda et al. Tetsu-to-Hagane. 1976, Vol.62, No.9, pp.1209-1218.
4) E. Scheil. Z.Mettalke. 1942, Vol.34, p.70.
5) H. D. Brody et al. Trans AIME, 1967, Vol.239, p.615.
6) Y. Ueshima et al. Tetsu-to-Hagane. 1987, Vol.73, No.11, pp.1551-1558.
7) Y. Ueshima et al. Tetsu-to-Hagane. 1988, Vol.74, No.3, pp.465-472.
8) Y. Ueshima et al. Tetsu-to-Hagane. 1989, Vol.75, No.3, pp.501-508.
9) Young-Mok Won et al. Metallurgical and Transactions A. 2001, Vol.32A, pp.1755 -1767.
10) The Japan Institute of Metals and Materials. Metals Databook. 4th Edition, Maruzen, 2004, p.22.
11) The Iron and Steel Institute of Japan. Handbook of iron and steel Ⅰ. The 3rd edition Maruzen, 1981, p.194.
12) S. Koriyama et al. International Journal of Metalcasting. 2020, Vol.14, No.3, pp.774-781.
13) Y. Kanzaki et al., R&D Kobe Steel Engineering Reports. 2000, Vol.50, No.1, pp.21-24.
14) S. Maekawa. Tetsu-to-Hagane. 1969, Vol.55, No.5, pp.381-401.
15) K. Narita. Tetsu-to-Hagane. 1974, Vol.60, No.13, pp.1820-1826.
16) H. Kondo. Tetsu-to-Hagane. 2004, Vol.90, No.10, pp.758-765.
17) A. Chino. 55th Shiraishi Memorial Lecture "Forefront of evaluation and analytical technology leading the leap of steel". 2004, Vol.55, pp.57-71.
18) M. Yanagida. Electric furnace steel. 1968, Vol.39, No.3, pp.161-169.
19) K. Narita. Tetsu-to-Hagane. 1981, Vol.67, No.16, pp.2603-2621.
20) K. Narita. Tetsu-to-Hagane. 1987, Vol 73, No.1, pp.67-83.
21) The Iron and Steel Institute of Japan. Handbook of iron and steel Ⅳ. third edition. Maruzen,1981, pp.327-336.
22) T. Kozeki et al. J. Japan Inst. Met. Mater. 2001, Vol.65, No.7, pp.644-651.
23) S. Kanazawa et al. Tetsu-to-Hagane. 1975, Vol.61, No.11, pp.2589-2603.
24) T. Takayama et al. Tetsu-to-Hagane. 1996, Vol.82, No.2, pp.147-152.
25) K. Yamada et al. Tetsu-to-Hagane. 2014, Vol.100, No.7, pp.867-872.
26) K. Kawamura et al. Tetsu-to-Hagane. 1971, Vol.57, No.1, pp.94-104.

Benefit Estimation of Soft-magnetic Pure Iron by Magnetic Field Analysis Considering Effect of Forging Strain

Shingo KASAI*1 ・ Dr. Masamichi CHIBA*2 ・ Shinya MORITA*3 ・ Takumi KITAYAMA*3

*1 Wire Rod & Bar Products Unit, Steel & Aluminum Business
*2 Wire Rod & Bar Products Development Department, Research & Development Laboratory, Steel & Aluminum Business
*3 Applied Physics Research Laboratory, Technical Development Group

Abstract

The movement toward carbon neutrality is expanding as a result of heightened environmental awareness. For soft-magnetic materials, whose usage is expected to increase as electrification progresses, the omission of the heat treatment step called magnetic annealing is regarded as one of the measures for reducing the amount of CO_2 produced by the manufacturing process. Kobe Steel's soft-magnetic pure iron, the ELCH2 series, has magnetic properties comparable to those of the magnetic-annealed material of low-carbon steel, even without magnetic annealing, and is being looked to as a non-heat-treated material of low-carbon steel. Using forging analysis and magnetic field analysis, a comparison has been made among the component characteristics when a solenoid iron core is changed from magnetic-annealed material of low-carbon steel to as-cold-forged material of ELCH2. This paper introduces the results indicating that the ELCH2, even if the magnetic annealing is omitted, achieves the same electromagnetic force at low current and also achieves higher electromagnetic force at high current than what is achieved by the magnetic-annealed material of low-carbon steel.

Introduction

Heightened environmental awareness, such as global warming countermeasures, is rapidly promoting electrification, mainly in the field of automobiles.[1] Kobe Steel is developing soft-magnetic pure iron, which makes the best use of the magnetic properties of iron, in response to the needs for such electrification, including smaller size, lighter weight, and the higher performance of electromagnetic equipment. **Fig. 1** is an image diagram of the operating frequency range and magnetic flux density of Kobe Steel's soft-magnetic pure iron.

Kobe Steel's products include the soft-magnetic pure iron, "ELCH2 series" (wire/bar) with proven performance mainly in DC applications; and the pure iron-based magnetic iron powder (MAGMEL) with proven performance in magnetic parts of electrical systems for AC applications. In addition,
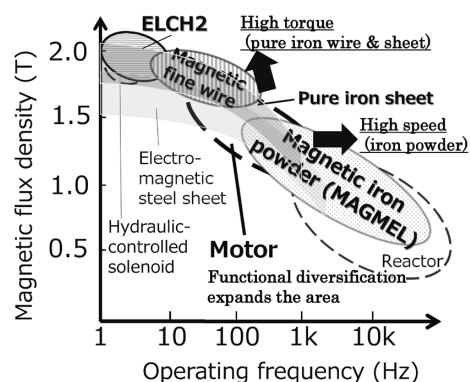

Fig. 1 Examples of operating frequency range and magnetic flux density

the company has developed a "pure-iron magnetic wire" with smaller diameters and "pure-iron sheets" with smaller thicknesses to reduce the eddy current, which lowers the AC magnetic characteristics. Kobe Steel is building a system to propose soft-magnetic pure iron suitable for each application.

This paper describes one such product, the soft-magnetic pure iron ELCH2 series. The ELCH2 series is used as an iron core material for linear solenoids and electromagnetic clutches and is a material that contributes to improving the performance of electromagnetically controlled components. Section 1 describes the advantages of the ELCH2 series (excellent magnetic properties and cold forgeability), and Section 2 describes the magnetic-field analysis results considering the strain due to cold forging to omit magnetic annealing, contemplating the growing need for carbon neutrality.

1. Soft-magnetic pure iron ELCH2 series

1.1 Chemical composition

Table 1 shows the exemplary chemical compositions of the ELCH2 series (ELCH2 and ELCH2S) and the composition standard of JIS soft magnetic irons, SUY.

The ELCH2 series is an ultra-low carbon soft-magnetic iron that increases the magnetic moment, the origin of ferromagnetism, by reducing the factors

Table 1 Example of chemical composition

Priority	Steel grade	C	Si	Mn	P	S
Magnetic properties	ELCH2	0.005	0.004	0.25	0.009	0.008
Machinability	ELCH2S	0.005	0.004	0.26	0.010	0.025
	JIS SUY	$\leqq 0.03$	$\leqq 0.2$	$\leqq 0.5$	$\leqq 0.03$	$\leqq 0.03$
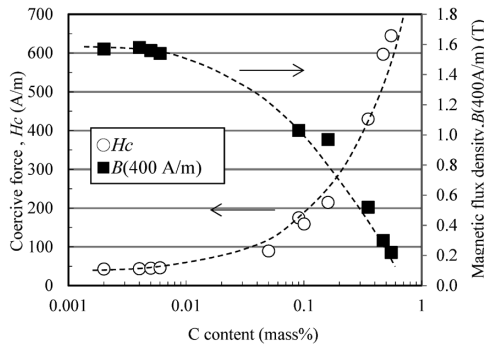
Fig. 2 Carbon content dependence of magnetic properties [2]

Fig. 3 Relation between grain size and coercive force [2]

Magnetic annealed	Non-annealed	850℃ × 3 h
Ferrite grain size number	6.0	4.0
Microstructure	0.1mm	0.1mm

・Magnetic annealed ⇒ furnace cooling (cooling speed＜100℃/s)

Fig. 4 Microstructure before and after magnetic annealing

that adversely affect magnetic properties as much as possible. Excellent magnetic properties (high magnetic flux density and low coercive force) are realized in the low to high magnetic field regions. **Fig. 2** shows the effect of carbon content on coercive force and magnetic flux density. The ferrite phase with ferromagnetism increases as carbon content decreases, improving both the magnetic flux density and coercive force.[2] Another advantage is the improved cold forgeability, a result of reduced Si and additional Mn.[3]

ELCH2S contains a small amount of S, an element improving the free-cutting property, and is a grade expected to reduce tool wear by half, compared with ELCH2. Excessive addition of S causes FeS to precipitate at the prior austenite grain boundary and lowers the magnetic properties. Hence, the Mn/S ratio is appropriately controlled to prevent the precipitation of FeS.[4]

1.2 Microstructure

The domain wall motion in a material is a critical factor that influences magnetic properties. The domain wall moves through the material as the external magnetic field changes. It is known, however, that the presence of lattice defects with low magnetic energy, such as grain boundaries, precipitates, and dislocations, hinders the movement and causes a declination in magnetic properties.[5] Hence, a heat treatment called "magnetic annealing" is applied to remove lattice defects caused by part fabrication processes such as rolling, wire drawing, forging, and cutting, and further coarsen the crystal grains.

Fig. 3 shows the relationship between the average grain size and coercive force before and
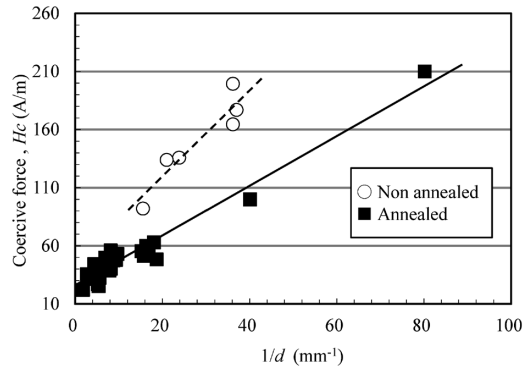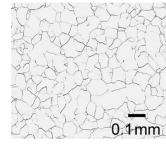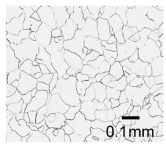
after magnetic annealing of ELCH2. **Fig. 4** shows the microstructure and ferrite crystal grain size before and after magnetic annealing of ELCH2 rolled material. It is shown that the grain size is coarsened by magnetic annealing, and the larger the grain size, the smaller the coercive force becomes. The crystal grain grows as the annealing temperature rises, but care must be taken not to overheat because the Ac3 point of the ELCH2 series is at about 910℃. If the annealing temperature is too high, a part of the ferrite begins to transform into austenite, and a temperature exceeding the Ac3 point results in a single-phase austenite which leads to the generation of a fine ferrite phase in the cooling process and deteriorates the magnetic properties. Desirably, the magnetic annealing shall be in the temperature range of the ferrite single-phase region and performed at around 850℃, considering the temperature variation of the heating furnace.

1.3 Magnetic properties

Table 2 shows the initial magnetization characteristics of the ELCH2 series before and after the magnetic annealing and of low-carbon steel S10C. Also included is the property lower limit of JIS SUY-0, the highest grade of JIS soft magnetic irons. The ELCH2 series after magnetic annealing has a magnetic flux density that satisfies the SUY-0 standard and has properties that can contribute to

Table 2 Example of magnetic properties

Steel		Magnetic flux density (T)				Hc (A/m)
		100 A/m	500 A/m	1,000 A/m	4,000 A/m	
Magnetic annealed	ELCH2	1.22	1.58	1.64	1.82	45
	ELCH2S	1.09	1.53	1.59	1.80	56
	S10C	0.45	1.40	1.54	1.74	86
Non annealed	ELCH2	0.32	1.32	1.54	1.76	96
	ELCH2S	0.23	1.29	1.54	1.76	105
JIS	SUY−0	0.90	1.35	1.45	1.60	≦60

Fig. 5 Comparison of critical upset rate [2]

Fig. 6 Microstructure of compressed specimen after magnetic annealing [2]

Fig. 7 FEM-analysis of equivalent strain (cold upsetting)
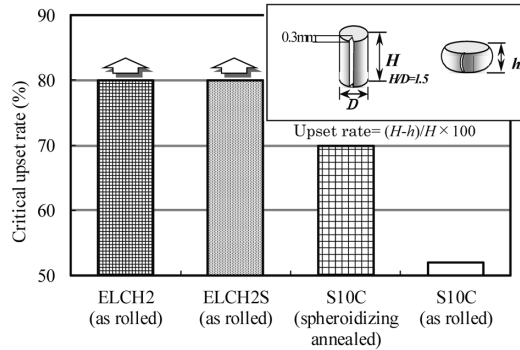
the miniaturization, weight reduction, and enhanced output of electromagnetic components. In addition, even without magnetic annealing, the steel product has properties at the same level as those of S10C after magnetic annealing, allowing the omission of magnetic annealing required by low-carbon steel, which is expected to improve productivity and contribute to carbon neutrality.

1.4 Effect on cold forgeability and post-annealing microstructure

The ELCH2 series has the advantage of high elongation, making cracks unlikely to occur. **Fig. 5** compares the critical upset rate of cracking for ELCH2 and S10C under severe conditions with a notch in each cylindrical test piece. Even as-rolled, the ELCH2 series exhibits a critical upset rate of cracking higher than that of the S10C spheroidize-annealed material, enabling cold forging of complex-shaped parts without soft annealing.

On the other hand, the strain energy due to cold working increases the driving force of grain growth,[6] and the strain distribution affects the grain size after magnetic annealing. **Fig. 6** shows the cross-sectional microstructure of the sample magnetically annealed after cold upsetting, and **Fig. 7** shows the analysis result for the equivalent strain distribution during cold upsetting. The plastic processing analysis software FORGE (trademark of Transvalor S. A.) was used to analyze the ELCH2 material on the basis of an axisymmetric model. As shown, the crystal grains in the part where the strain is minor, near the fixed end (the upper part of Fig. 6 a and c), have been coarsened. On the other hand, the part
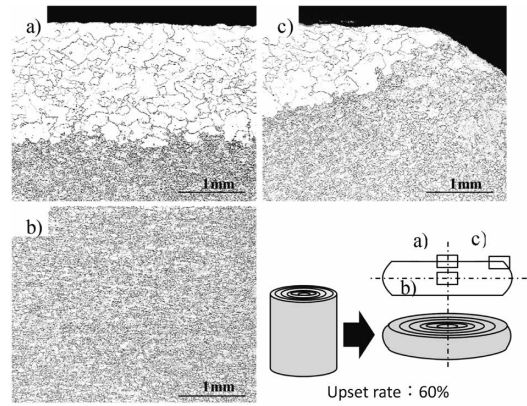
with significant strain, in the center (Fig. 6b), has not coarsened, due to the effect of the remaining strain. The improvement of component characteristics requires strain distribution and annealing conditions that maximize the grain size of the part where magnetic properties are critical, such as a magnetic circuit part where magnetic flux concentrates.

1.5 Temperature dependence

Fig. 8 shows the temperature dependence of the coercive force of the ELCH2 series, and **Fig. 9** shows the temperature dependence of its magnetic flux density. Since the detailed measurement conditions are different, the room temperature characteristics are standardized to 100% for the plotting.

There is no significant difference in magnetic flux density, but the coercive force deteriorates on the low-temperature side. The cause of the deterioration of the coercive force on the low-temperature side is thought to be the effect of an increase in the magnetic anisotropy coefficient[7] and the heat shrinkage of the test piece (an increase in internal strain). It is essential to consider the manufacturing process and usage environment to demonstrate the performance of soft-magnetic material.

Table 3 Examples of magnetic properties of ELCH2 applied work strain by cold upsetting

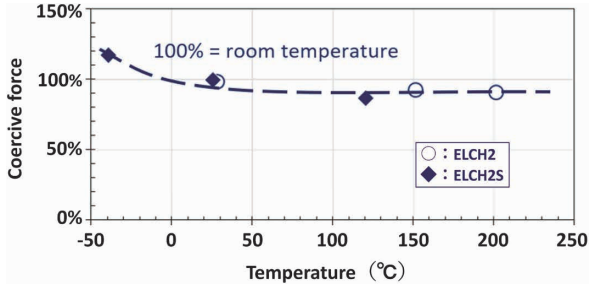| Steel	Upset rate	Magnetic flux density (T)				Hc
		100 A/m	500 A/m	800 A/m	5,000 A/m	(A/m)
ELCH2 non magnetic annealed	0%	0.39	1.24	1.45	1.79	91
	20%	0.04	0.80	1.03	1.74	178
	40%	0.03	0.71	1.01	1.74	218
	60%	0.02	0.61	0.96	1.73	228

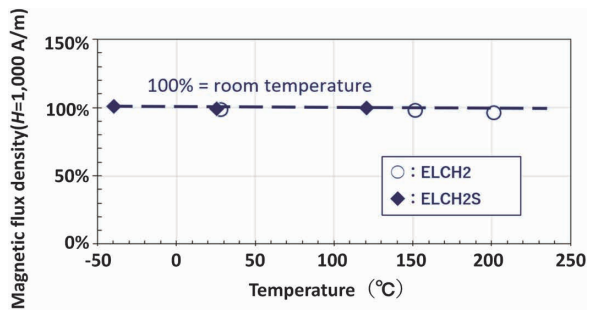

Fig. 8 Temperature dependence of coercive force

Fig. 9 Temperature dependence of magnetic flux density (H=1,000 A/m)
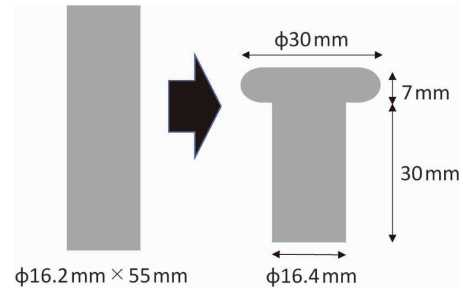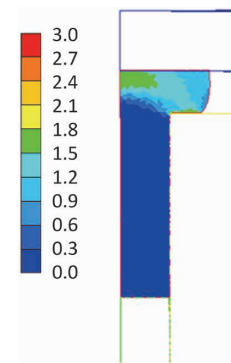

Fig.10 Shape of iron core after cold upsetting process

Fig.11 Calculated equivalent strain in cold upsetting

2. Example of applications to electromagnetic components

Maximizing the electromagnetic component's function while maintaining productivity requires setting the processing conditions that best use the magnetic material's characteristics. This section describes an example of magnetic field analysis regarding the effect of cold-forging strain on component characteristics. This example is in response to the fact that energy reduction in heat supply is being studied from the viewpoint of carbon neutrality.[8] The ELCH2 is assumed to be used as cold-forged without magnetic annealing. Electromagnetic field analysis software JMAG was used for the magnetic field analysis.

2.1 Changes in magnetic properties due to cold forging

The strain associated with cold working reduces the magnetic moment and acts as pinning of the domain wall, thus deteriorating the magnetic properties after cold working. **Table 3** shows the magnetic properties measured on a ring-shaped specimen of $\phi 38$ mm $\times$ $\phi 30$ mm $\times$ thickness 4 mm collected from the central part in the axial direction of material after cold-forging (upsetting) a $\phi 44$ mm $\times$ 50 mm ELCH2 rolled sample at room temperature. As the compression rate increases, the strain increases, and the magnetic properties deteriorate.

2.2 Analysis method and results

Fig.10 schematically illustrates the shape of a sample cold forged around the upper side of the $\phi 16.2$ mm $\times$ 55 mm cylindrical iron core, and **Fig.11** shows an equivalent strain contour diagram of the forging analysis. The upper side, with large deformation, shows a significant strain. Three solenoid models were made, each comprising a pair of iron cores of the above dimensions abutting against each other with a coil and an outer cylinder disposed outside the pair of cores. In the first model, the iron cores were made of ELCH2 (without strain consideration, without magnetic annealing). In the second model, the iron cores were made of ELCH2 (with strain consideration, without magnetic

annealing). In the third model, the iron cores were made of S10C (without strain consideration, with magnetic annealing). Then the electromagnetic force between each pair of iron cores was analyzed for comparison. The analysis was performed in the following steps: (1) performing axisymmetric forging analysis on FORGE and outputting strain distribution data; (2) passing the strain distribution data to JMAG and interpolating the magnetic properties of each part from the measured data regarding the strain distribution; and (3) performing axisymmetric magnetic field analysis on JMAG and outputting the electromagnetic force. **Fig.12** shows the magnetic flux density contour diagram at a coil current of 0.5 A, and **Fig.13** shows the results of electromagnetic force analysis.

A comparison between the contour diagrams of ELCH2 with and without strain consideration shows that the magnetic flux with strain consideration is concentrated at the root corner of the collar. This is due to the decreased magnetic properties in the top region with high forging strain, and the magnetic saturation due to corner concentration slightly lowers the electromagnetic force. The effect of strain can also be seen from the fact that the contour diagrams of ELCH2 and S10C without strain are similar. The electromagnetic force analysis results show that ELCH2 has a greater electromagnetic force than S10C i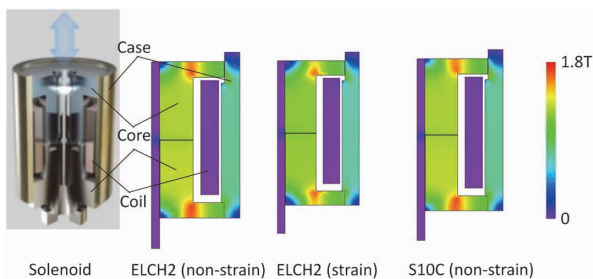n the high current region regardless of strain. This is because ELCH2 is superior in magnetic flux density on the high magnetic field side (Table 2). Analysis considering strain clarifies the cause of characteristics change, enabling measures to alleviate saturation, such as rounding the corners. Thus, it is possible to omit annealing for the ELCH2 forged product to achieve the same performance as the S10C annealed product.

The above results demonstrate the possibility that changing from S10C machined products (with magnetic annealing) to ELCH2 forged products (without magnetic annealing) leads to material yield improvement by altering the process from cutting to forging and productivity improvement and energy reduction by omitting magnetic annealing, without sacrificing the component characteristics.

Kobe Steel will continue contributing to the realization of carbon neutrality by proposing solutions while utilizing analysis technology to maximize component functions and improve productivity in the manufacturing process.

Conclusions

This paper has introduced the advantages of the soft-magnetic pure iron ELCH2 series and has demonstrated the possibility of changing from machined products of low-carbon steel (with magnetic annealing) to ELCH2 forged products (without magnetic annealing) and thus omitting heat treatment (soft annealing and magnetic annealing) and improving material yield. Kobe Steel will continue to propose solutions, including optimal conditions taking an extra step into the manufacturing process of components, and contributing to the challenges such as the realization of carbon neutrality.

Fig.12 Magnetic flux density distribution in solenoid components

Fig.13 Estimated magnetic force by FEM analysis

References

1) METI. Materials for the 1st Automotive New Era Strategy Conference. 2018.
2) M. Sakata et al. R&D Kobe Steel Engineering Reports. 2015, Vol. 65, No. 2, pp. 6-11.
3) M. Chiba. The Special steel. 2015, Vol. 64, No. 2, pp. 24-27.
4) M. Chiba et al. R&D Kobe Steel Engineering Reports. 2005, Vol. 55, No. 2, pp. 18-21.
5) S. Okamoto. Magnetism and Materials. KYORITSU SHUPPAN CO., LTD, 1988, p. 72.
6) T. Kunitake et al. Bulletin of the Japan Institute of Metals. 1982, Vol. 21, No. 8, pp. 589-596.
7) Silicon Steel Sheet Special Committee. IEEJ Journal. 1954, Vol. 74, No. 790, pp. 822-830.
8) NEDO. TSC Foresight. 2020, Vol. 101.4

Axial-gap Motor Using Thin Wire of Soft-magnetic Pure-iron

Shinya MORITA*1 · Takuya MATSUMOTO*2 · Shingo KASAI*3

*1 Applied Physics Research Laboratory, Technical Development Group
*2 Applied Physics Research Laboratory, Technical Development Group (currently Japan Superconductor Technology, Inc.)
*3 Wire Rod & Bar Products Unit, Steel & Aluminum Business

Abstract

Since wires of soft-magnetic pure-iron have high magnetic flux densities, they are used for the iron cores of electromagnetic parts for DC-driven components such as electromagnetic relays and solenoids. It has been difficult, however, to apply them to AC-driven components, such as motors, due to the skin effect and eddy current caused in the material. The application to a motor has been examined by decreasing the diameter of the wire of soft-magnetic pure-iron to reduce the eddy current loss. This paper reports the results of a prototype of an axial-gap motor with a new structure using a wound-on iron core of the hexagonal thin wire of pure iron.

Introduction

Addressing global warming and achieving carbon neutrality have recently become pressing issues worldwide. The spread of electric vehicles emitting no CO_2 is also expected to accelerate in the automobile industry. In addition, technological innovations such as Connected, Autonomous, Shared, Electric (CASE) are digitizing and electrifying the drive motors and various components of automobiles, and the diversification of electromagnetic components to meet various needs is expected to continue in the future. A radial-gap motor using a laminated iron core of electrical steel sheets is often used for the onboard auxiliary motor. On the other hand, there is a growing need for miniaturization to accommodate the mounting space of motors, activating the development of an axial-gap motor (AGM) with a structure different from that of the ordinary radial-gap motor. Axial-gap motors are easily made into flat shapes, an advantageous feature for torque enhancement, miniaturization, and weight reduction, and are attracting attention as, for example, in-wheel type motors for directly driving wheels. This paper reports a study on a new AGM using soft-magnetic pure-iron wire with high magnetic flux density and excellent workability. Compared with electrical steel sheets, the soft-magnetic pure-iron wire has fewer impurities and thus a higher magnetic flux density, an advantageous feature for realizing high motor torque in the low rpm region, where the influence of iron loss is minimal. However, the electrical resistance becomes too low if used as bulk, increasing the eddy current loss. Hence, the wire diameter has been reduced to decrease the loss. This paper introduces the exemplary magnetic characteristics of such a soft-magnetic pure-iron thin wire and reports on the motor performance when applied to the AGM's stator iron core, which exploits its high magnetic flux density.

1. Study on motors using soft-magnetic pure-iron thin wire

1.1 Soft-magnetic pure-iron thin wire

Kobe Steel manufactures the soft-magnetic pure iron ELCH2 series, which is widely used in automotive parts such as electromagnetic relays and solenoid iron cores.[1), 2)] The ELCH2 has excellent magnetic characteristics such as high magnetic flux density and low coercive force and is expected to contribute to the effects of miniaturization, weight reduction, low power consumption, and improved responsiveness of "particularly" DC-driven electromagnetic components. On the other hand, it is essential for motors to reduce the iron loss generated in the magnetic body by the AC-magnetic field. As shown in Equation (1), the eddy current loss, which is a part of the iron loss, is proportional to the square of the wire diameter of the material, and it is necessary to use a thinner wire to reduce the eddy current loss;

$$P_v \propto (fB_md)^2/\rho \qquad\qquad\qquad (1)$$

wherein P_v is the eddy current loss, f is the frequency, B_m is the magnetic flux density amplitude, d is the magnetic material diameter, and ρ is the electrical resistivity of the magnetic body.

Generally, thin metal wires are manufactured by cold wire drawing using dedicated dies. The pure iron-based soft magnetic materials are soft and have excellent cold workability, which enables the fabrication of a shape with a regular hexagon as cross-section, facilitating an increase in the space factor.

Fig. 1 and **Table 1** show the AC-magnetization curves (frequency 50 Hz) and iron loss measurements

of two types of soft-magnetic pure-iron thin wires with different wire diameters. The figure and table also include examples of the magnetic characteristics of non-oriented electrical steel sheets, 35A300 and 50A600, specified in JIS C 2552. The soft-magnetic pure-iron thin wires have cross-sectional shapes of regular hexagons with opposite sides of 1.24 mm and 0.71 mm, respectively. Kobe Steel's ELCH2 has been cold-drawn to specified wire sizes and heat-treated in a reducing atmosphere to improve their magnetic characteristics. Although the iron loss is slightly higher than that of electrical steel sheet, the pure-iron thin wires are characterized by high saturation magnetic flux densities thanks to the low level of impurities and are suitable for the motors used in the low-rotation, high-torque range where high magnetic flux density is required.
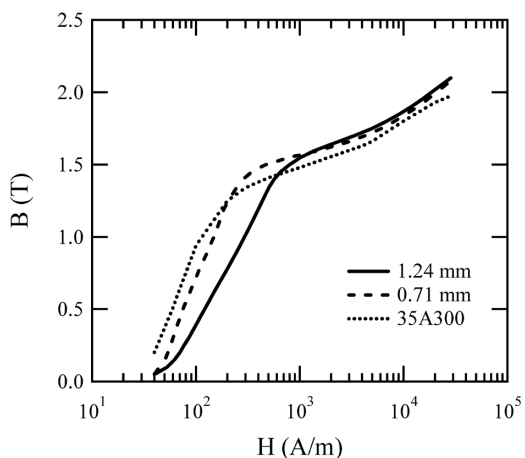

Fig. 1 B-H curves of pure iron hexagonal thin wires

1.2 Design of axial-gap motors

To increase the torque ratio of a motor, it should desirably have a flat shape, in which the torque generating part (the gap between the stator and the rotor) is placed as far outside the rotating body as possible. As shown in **Fig. 2**, a radial-gap motor has a torque generating part placed inside the stator, whereas an AGM has the same located at the outermost part of the iron core and is advantageous for high torque. On the other hand, AGMs have manufacturing issues. For example, there is a report referring to an AGM with a fixed iron core formed by winding and laminating electromagnetic steel sheets in a doughnut shape and then cutting them into a fan shape,[3] but its yield is poor, and the magnetic properties may deteriorate due to the bending. A thin wire could merely be wound and cut to be used as an iron core. Hence, an AGM using pure-iron thin wire has been designed on the basis of electromagnetic field analysis so that it would have the same rating as an auxiliary radial-gap motor commercially available for automobiles. Fig. 2 compares the newly designed AGM with the radial-gap motor reference. The AGM comprises two rotors

Table 1 Example of magnetic properties of pure iron hexagonal thin wires

| Material | Magnetic flux density (T) | | | Iron loss (W/kg) $W_{15/50}$ |
	B_{25} 2,500 A/m	B_{50} 5,000 A/m	B_{100} 10,000 A/m	1.5 T / 50 Hz
Pure iron hexagonal thin wire (d=1.24 mm)	1.65	1.75	1.87	11
Pure iron hexagonal thin wire (d=0.71 mm)	1.63	1.71	1.84	5.35
35A300 (JIS)	> 1.49	> 1.60	> 1.70	<3.0
50A600 (JIS)	> 1.57	> 1.66	> 1.76	<6.0
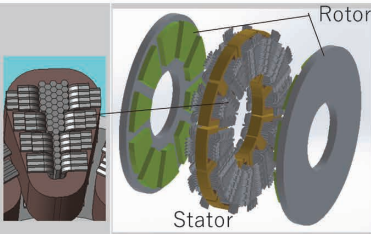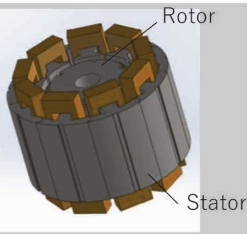
CAD model	Axial gap motor using pure iron thin wire	Radial gap motor
Motor type	Axial gap type (2 Rotor, 1 Stator)	Radial gap type
Poles / slots	10 poles/ 12 slots	6 poles / 9 slots
Core size	Φ 101 x 37 mm	Φ82 x 70 mm
Core volume	296 cm³ (-20% downsized)	370 cm³
Weight	1.41 kg	1.68 kg

Fig. 2 Specifications of the axial gap motor and a commercial radial gap motor

and one stator, configuring ten poles and twelve slots, in which neodymium magnets, "N42SH", are used for the rotor poles. The air gap between the rotor and stator is 1 mm. The rated rotational speed is 1,080 rpm, the rated torque is 1.3 Nm, and the rated output is approximately 150 W, roughly the same as the output of the commercial motor. The iron core volume of the commercial motor is 370 cm^3, while that of the prototype AGM is 296 cm^3, designed to be 20% more compact. The weight, including the casing, is 1.68 kg for the commercial motor, while that of the prototype AGM is 1.41 kg, a weight reduction of 15%.

1.3 Prototyping of axial-gap motor

Fig. 3 shows a photograph of the prototype AGM stator. The AGM stator uses 85 pure-iron hexagonal wires, each with an opposing side's length of 1.24 mm per tooth. The wires have been magnetic annealed before winding to enhance the magnetic characteristics. The thin wires near the center of the iron core are straight, but each thin wire from the outermost layer to the second layer is bent into a U-shape. This increases the facing area between the stator iron core and the rotor magnet, gains the flux content between the stator and rotor, and enhances the torque. This structure is also advantageous in facilitating the fixing of the coil.

1.4 Electromagnetic field analysis of motor and apparatus for evaluating on actual machine

For the motor design, FEM analysis was performed in advance using the commercially available electromagnetic field analysis software JMAG (ver. 20, registered trademark of JSOL Corporation). The fine wire iron core of the stator has a complicated shape, making the CAD modeling challenging and requiring a significant computational load. Hence, a simplified model was used. The simplified model was made into a bulk shape slightly larger than the actual iron core to
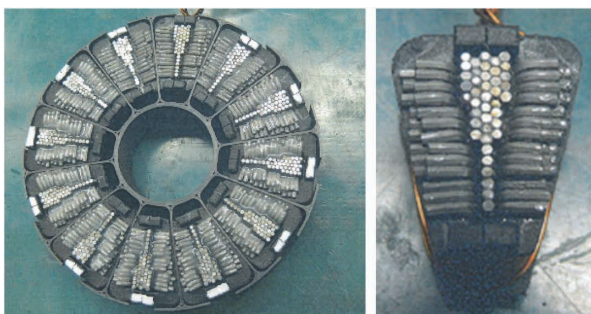

Fig. 4 Bulk core model of the AGM for FEM simulation
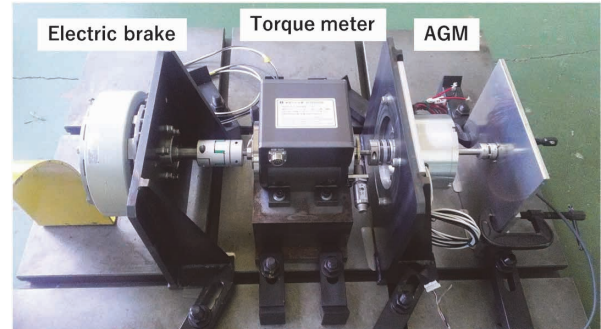
Fig. 5 System for measuring motor properties

enclose the fine-wire iron core, and the space factor of the iron core was adjusted to make the material weight equal to that of the actual machine (**Fig. 4**).

The prototype motor was evaluated using a motor evaluation apparatus in which a Mitsubishi Electric powder brake ZKB-5XN and a torque meter were coupled coaxially, as shown in **Fig. 5**. A MyWay PE-INVERTER was used to control the prototype motor, and a HIOKI power analyzer 3390 was used to obtain efficiency maps in the torque range from 0.3 to 1.6 Nm and the number of rotations from 600 to 1,600 rpm.

2. Evaluation results for prototype motor on actual machine and verification of analysis results

2.1 Evaluation results for prototype motor on actual machine

Fig. 6 shows the results of the AGM's efficiency map measurement. Operating point A represents a point near the rated value of the reference motor (1,000 rpm, 1.3 Nm), operating point B represents a point of high-torque and low-rotation (800 rpm, 1.5 Nm), operating point C represents a point of low-torque and high-rotation (1,600 rpm, 0.6 Nm) and operating point D represents a point of high-torque and high-rotation (1,600 rpm, 1.6 Nm). The motor efficiency is especially high in the high torque range, and the maximum efficiency of 79.8% has been

Fig. 3 Photograph of the axial gap motor

Fig. 6 Efficiency of the axial gap motor

Fig. 7 Motor power and loss at each operating point

confirmed at point D, which is the maximum torque and maximum rotational speed in the measured range. The efficiency at point A near the rated value is 78.9%, which is approximately 2.5 points lower than 81.4% of the referenc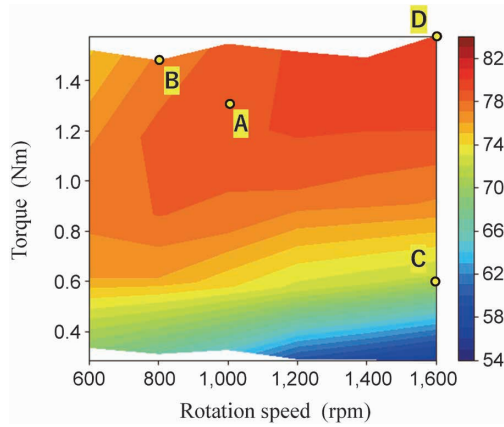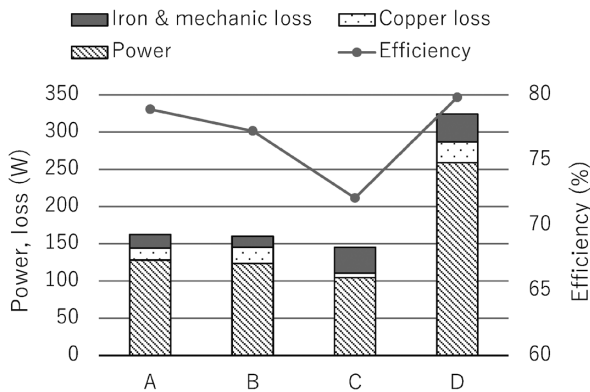e radial-gap motor. Also, the efficiency of AGM is lower than the value designed by electromagnetic field analysis. The material's magnetic properties were possibly affected by the iron-core processing and assembly of the motor. Hence, optimizing the motor manufacturing method and reducing the wire diameter will realize performance comparable to commercial motors.

Fig. 7 shows motor output, copper loss, mechanic loss + iron loss (calculated by subtracting copper loss from input power) at operating points A to D on the efficiency map. Points A to C are all operating points with an input power of about 150 W. Compared to point C, with low-torque and high-rotation, points A and B on the high-torque and low-rotation sides have improved efficiency. As for the breakdown of loss, the iron loss ratio is high at point C, while the copper loss ratio is higher at points A and B than at point C. Generally, the iron loss depends on the number of rotations and increases on the high rotation side, and the copper loss increases on the high torque side because it is proportional to the

square of the current. The prototype AGM reduces the current required for torque output by using a thin pure-iron wire with a high magnetic flux density. From reference points A to C, this AGM is concluded to have a feature of high efficiency even in the high torque range where copper loss is dominant.

2.2 Comparison with electromagnetic field analysis results

Fig. 8 shows the AGM's motor efficiency calculated by electromagnetic field analysis. Similar to the evaluation results on the actual machine, the motor efficiency increases with increasing rotation speeds and torque beyond the range of Fig. 8. For example, the highest efficiency point for 1,600 rpm and 1.6 Nm is 82.6%. The efficiency determined by the electromagnetic field analysis is 3 to 10% higher than that measured on the actual machine in all areas. Possible reasons for this include the effect of mechanical loss, not considered in the analysis, the approximation of the fine wire iron core as a bulk shape, and the effect of increased iron loss in the bent part.

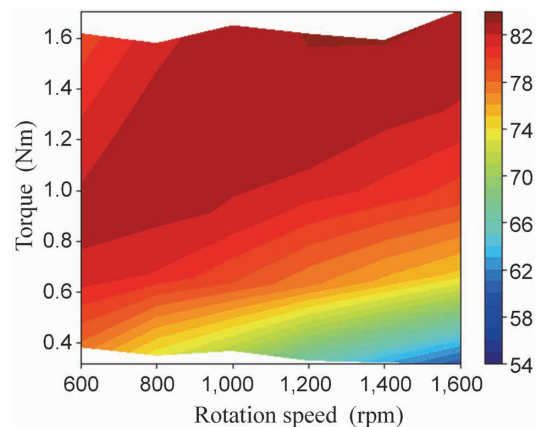**Fig. 9** shows the relationship between the torque

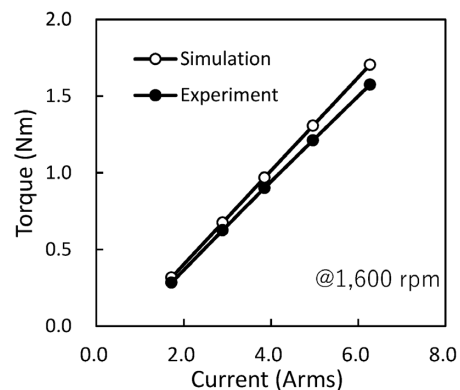Fig. 8 Motor efficiency calculated by FEM simulation

Fig. 9 Comparison of experimental and simulation data for torque current property at 1,600 rpm

and effective current value at 1,600 rpm. Fig. 9 shows the results of both the electromagnetic field analysis and the actual machine evaluation. Although the electromagnetic field analysis results show slightly higher torque, the error is within 10%, and the model approximating a fine iron core to a bulk shape should allow the rough design of a motor with thin hexagonal wire. On the other hand, the bulk model has teeth significantly different from that of the bent fine wire. Hence, tuning the shape and space factor should lead to a design with higher accuracy.

2.3 Effect of thin-wire diameter

The prototype motor has a large iron loss ratio in the high rpm range. Therefore, reducing the iron loss of the fine wire is expected to improve efficiency. As shown in Fig. 1, the thin wire with 0.71 mm opposing sides has lower iron loss and magnetic characteristics better than the thin wire with 1.24 mm opposing sides used in the prototype. Hence, electromagnetic field analysis was performed on the motor characteristics when the magnetic characteristics of 0.71 mm thin wire were applied

Fig.10 Simulation results of (a) motor efficiency, (b) iron loss and (c) torque for the axial gap motor (1,600 rpm, I_{rms}=6.3 A)

to the analysis model in section 2.2 to investigate the effects of material properties. **Fig.10** compares the torque, efficiency, and iron loss at a rotational speed of 1,600 rpm, effective current value of 6.3 A (torque 1.6 Nm), i.e., the highest efficiency point in the actual machine evaluation (iron loss in the experimental results includes mechanical loss). Reducing the wire diameter from 1.24 mm to 0.71 mm has improved efficiency by 6 points, increased torque by 6%, and reduced the iron loss of the motor iron core by 58%. The electromagnetic field analysis indicates that the maximum magnetic flux density at the center of the iron core is approximately 1.5 T, and the 0.71 mm wire has excellent magnetic characteristics below 1.5 T (Fig. 1), which is believed to have improved the motor performance. Pure iron has excellent workability, which facilitates the thinning of the diameter. A smaller diameter and higher space factor are expected to result in higher motor torque with higher efficiency.

Conclusions

Reducing the diameter of pure iron-based soft magnetic material decreases iron loss. Applying such thin magnetic wire to the stator iron core of an axial-gap motor can reduce its size and weight. The pure-iron thin wire with a high magnetic flux density is expected to lead to enhanced torque, miniaturization, and weight reduction of the motor and is also suitable for, to give an example, a direct drive without a speed reducer. The motor introduced in this paper is merely an example of utilizing pure-iron thin wire. Kobe Steel will continue to contribute to the improved performance of electromagnetic components by devising unprecedented structures and manufacturing methods.

References

1) M. Chiba et al. R&D Kobe Steel Engineering Reports. 2002, Vol.52, No.3, pp.66-69.
2) M. Sakata et al. R&D Kobe Steel Engineering Reports. 2015, Vol.65, No.2, pp.6-11.
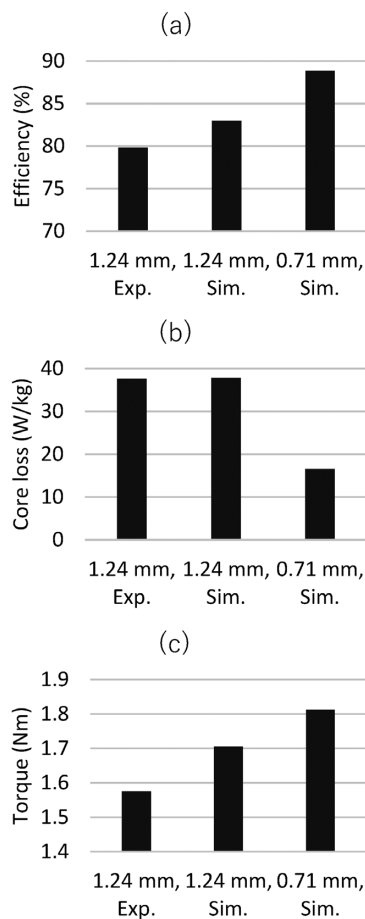3) N. Matsui. Rare earth-saving/No rare earth motors. NIKKAN KOGYO SHIMBUN, LTD. 2013.

Technology for Improving Performance of Tin Plating for Automotive Terminals

Yutaro UEDA*[1] · Masahiro TSURU*[1]

*[1] Copper Rolled Products Plant, Copper Rolled Products Unit, Advanced Materials Business

Abstract

Copper alloy, which has excellent electrical conductivity, is widely used for automotive terminals. Since copper alloys are oxidized in the atmosphere, and their oxide coating acts as electrical resistance, tin plating is applied to keep the contact resistance low. This paper explains the characteristics required for the tin plating of automobile terminals and introduces Kobe Steel's original tin-plated products with new reflow plating (high thermal resistance and low friction).

Introduction

Automobiles are equipped with electrical components that consist of, for example, control computers, sensors, and actuators, which are connected by wire harnesses. A wire harness is an assembly consisting of electrical wires and connectors, and the terminals built into each connector are one of the essential parts for transmitting power and signals. Recently, the electrification of automobiles is accelerating to realize "CASE," including automatic driving and electric driving. As a result, the number of onboard electronic devices has increased, and so has the number of electrical wires and terminals. These terminals are generally made of copper alloy, which has excellent electrical conductivity; however, copper alloys oxidize in the atmosphere, and the oxide film becomes electrical resistance. Hence, the common practice is applying a surface treatment such as tin plating to maintain the low contact electrical resistance (hereinafter referred to as "contact resistance") of each contact point, which is the connection part of the terminal.

This paper explains the characteristics required for the tin plating of automobile terminals and introduces Kobe Steel's original tin plating products, "new reflow plating (heat resistant specifications, low friction specifications)."

1. Characteristics required for terminal tin plating

The characteristics required for the tin plating of terminals are described, taking the tin plating used for the mass-production at Kobe Steel as an example. The cross-sections of copper alloy with reflow tin plating and new reflow plating in the plating/reflow process are illustrated in **Fig. 1**. Reflow tin plating is a type of plating performed by applying electric tin plating to a copper alloy and then heating and melting the plating above the melting point of tin (hereinafter referred to as "reflow treatment.") The reflow tin plating produces an intermetallic compound layer of tin and copper (hereafter referred to as copper-tin-based intermetallic compound) on top of the copper alloy and the surface covered with tin.

The new reflow plating consists of three layers of nickel, copper-tin-based intermetallic compound, and tin on the copper alloy. Fine asperities are given to the copper alloy surface in advance, and when plating is applied in the order of nickel, copper, and tin, the plating follows the asperities of the material. After that, the tin melts during the reflow treatment, the asperities formed after plating are smoothed, and the copper-tin-based intermetallic compound is exposed on the convex surface. As a result, fine copper-tin-based intermetallic compounds are dispersed on the tin-plated surface.

1.1 Contact reliability

Contact reliability is one of the most important characteristics required for terminals, and they are required to continue transmitting electrical signals and power from the moment of production until an automobile's end of life. To this end, the contact resistance of the terminal contact point must be kept low. Contact resistance is expressed by Equation (1) as the sum of film resistance, which is the electrical resistance of the film itself, and constriction

Fig. 1 Cross section structure of tin plated copper alloys in plating and reflow processes
*IMC: Intermetallic compound layer of tin & copper

resistance due to current concentration:[1), 2)]

$$R = R_f + R_c \cdots\cdots\cdots\cdots\cdots\cdots\cdots\cdots\cdots\cdots\cdots\cdots (1)$$

wherein R is the contact resistance (Ω), R_f is the film resistance (Ω), and R_c is the constriction resistance (Ω).

The film resistance and constriction resistance when homogeneous metals make contact are expressed by Equation (2):

$$R_f = \rho_f\, d\, /\, \pi a^2,\ R_c = \rho\, /\, 2a \cdots\cdots\cdots\cdots\cdots\cdots (2)$$

wherein ρ_f is the film-specific resistance ($\Omega\cdot m$), d is the film thickness (m), ρ is the metal-specific resistance ($\Omega\cdot m$), and a is the contact surface radius (m).

According to Equation (2), the film resistance decreases as the film thickness decreases and the contact area increases, and the constriction resistance decreases as the radius of the contact surface increases; that is, the contact area increases.

The tin plating applied to the copper alloy surface is covered with a thin oxide film. Oxide films have higher electrical resistance than metal and inhibit electricity transmission; hence, contact resistance generally increases when the oxide film is formed. However, in the case of tin plating, a thin hard oxide film (strength: 16.5 GPa)[3)] is formed on the soft tin (strength: 50-70 MPa).[3)] As a result, the oxide film cannot follow the deformation of the tin caused by sliding when the terminal is inserted and is broken, making it easy to obtain contact between the tins. Therefore, tin plating exhibits low contact resistance even when an oxide film is formed on its surface.

Tin plating is widely used for the contact points of terminals because it is a relatively inexpensive metal and provides stable contact reliability thanks to the breakage of the oxide film. However, in recent years, the miniaturization of the terminal has made it difficult for the oxide film to break, and the mounting environment, with factors such as heat and vibration, has become more severe, making it easier for tin plating to cause an increase in contact resistance. Hence, tin plating requires heat resistance to withstand high-temperature environments and fretting wear resistance to endure vibration and temperature changes.

1.2 Heat resistance

The primary heat source in an automobile is the heat-generating engine, and the engine room tends to be hotter than the car interior.[4)] The engine room reaches a maximum temperature of 120℃ under a scorching sun,[4)] and the accelerated life testing requires a heat resistance temperature of 150-160℃. In addition, due to the electrification of on-vehicle components, the number of terminals per connector is increasing, and the dense terminals make heat escape difficult. Therefore, the demand for heat resistance is becoming more stringent.

Fig. 2 illustrates the cross-section of a box terminal. Terminals include a box-shaped female terminal and a plate-shaped male terminal. The contact resistance is kept low by inserting the male terminal into the female terminal and applying a contact load with the spring of the female terminal. The miniaturization of terminals decreases the contact load of the spring holding down the contact point. Contact resistance depends on load, and the contact resistance tends to increase as the contact load decreases. This is because the contact area decreases as the contact load decreases,[5)] and the oxide film is less likely to be destroyed.

Gold plating, which has high electrical reliability, is generally used at locations of low contact load, where the oxide film is less likely to be destroyed, but gold plating is very expensive, and there is a need to reduce costs by applying tin plating. In addition, electrical reliability is highly required in high-temperature environments where oxide films easily grow. Hence, in areas where the contact load is low in a high-temperature environment, it is necessary to improve the contact reliability of tin plating.

Fig. 3 shows the contact resistance before heating and after holding at 160℃ for 1,000 h. The contact resistance was calculated on the basis of the voltage drop measured by the four-terminal method. A plate-shaped plating specimen and a gold wire bent into a U-shaped probe were used for the measurement. The probe was pressed against the specimen, and the voltage drop was measured at each load in the range of 1 to 5 N while gradually increasing the vertical load. The measurements were made while sliding in one direction at a speed of 1 mm/min. Before heating, all plating specimens maintained contact resistance below 1mΩ under the load of 1 to 5 N. This is considered to be because the tin oxide film had been destroyed by the sliding. After holding for 1,000 h, the contact resistance of the reflow tin plating increased significantly, exceeding 5 mΩ at load 3 N. On the other hand, with
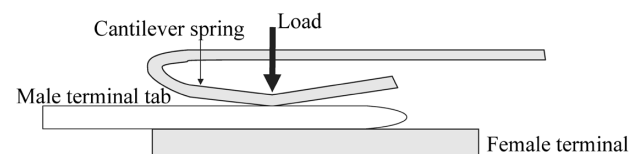

Fig. 2 Schematic image of cross section of terminal

the new reflow plating, the contact resistance was less than 1 mΩ at a load of 3 N and above, showing almost no increase, and maintaining 5 mΩ or less even at a load of 1 N.

Fig. 4 shows the results of cross-sectional SEM observation of tin plating after holding at 160℃ for 1,000 h and the construction of the oxide film in the surface layer. In the reflow tin plating, tin disappears, and a copper-tin-based intermetallic compound, Cu_3Sn (ε phase), is formed. It is considered that the exposure to a high-temperature environment has promoted the mutual diffusion of copper and tin in the material, forming a primary copper-tin-based intermetallic compound, Cu_6Sn_5 (η phase), depleting tin, and further diffusion has resulted in the formation of Cu_3Sn (ε phase).[6] In addition, a thick layer of Cu_2O is formed on the surface of the reflow tin plating. The specific electrical resistance of copper oxide (CuO: 10^6-$10^7 \Omega \cdot m$, Cu_2O: $10 \Omega \cdot m$)[7] is higher than that of tin oxide (SnO_2: $4 \times 10^{-4} \Omega \cdot m$)[7] and is considered to affect the contact resistance significantly. It is presumed that the formation of Cu_3Sn with a high copper content increased the thickness of the highly resistant copper oxide on the surface layer and the contact resistance. It is also presumed that the lower the load, the more difficult it is for oxide to be removed by sliding, which further increases the contact resistance.

In the case of the new reflow plating, Cu_6Sn_5 and a certain amount of tin is retained even after holding for 1,000 h. Unlike the reflow tin plating, no thick copper oxide is formed. Therefore, it is presumed that the oxide has been easily removed by sliding to maintain the low contact resistance. Tin and Cu_6Sn_5 are maintained because the underlying nickel plating suppresses the diffusion of copper from the base material, making it difficult for copper oxide to form.

It should be noted, however, that when tin plating is directly applied to the nickel plating, an intermetallic compound of nickel and tin is formed, reaching up to the plating surface due to mutual diffusion of nickel and tin in a high-temperature environment, resulting in the formation of nickel oxide with high resistivity (NiO: $4 \times 10^{11} \Omega \cdot m$)[7] on the surface. As a result, the contact resistance increases.[8] Therefore, it is necessary to form
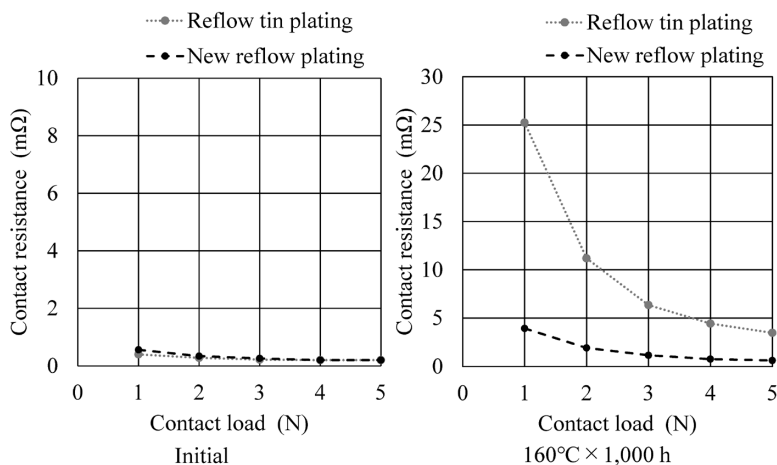
Fig. 3 Relationship between contact load and contact resistance before and after 160℃×1,000 h annealing
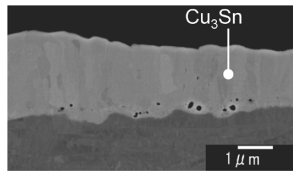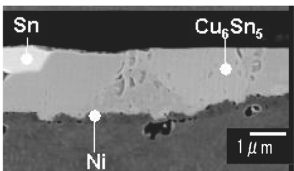
		Reflow tin plating	New reflow plating
SEM images of cross section			
Etching depth	0 nm	SnO_2, Cu_2O, CuO	SnO_2, Cu_2O, CuO
	5 nm	SnO_2, Cu_2O	SnO_2, Cu_2O
	15 nm	SnO_2, Cu_2O	SnO_2
	20 nm	SnO_2	-

Fig. 4 Cross sectional SEM images and composition of oxide films of tin plating after 160℃×1,000 h annealing

the 3-layer structure with a copper-tin-based intermetallic compound between the nickel and tin layers to suppress the diffusion.

The above facts show that it is essential to maintain tin and Cu_6Sn_5 to suppress the increase in contact resistance at high temperatures. To that end, it is effective to increase the thickness of the tin or use a 3-layer plating structure with a nickel layer, as in the case of the new reflow plating.[1]

1.3 Fretting wear resistance

Fretting wear is a phenomenon in which slight rubbing occurring between the contact points of terminals causes wear of the plating at the contact points. Once fretting wear occurs, the contact resistance may increase as the wear debris of tin accumulates and oxidizes between the contact points. Fretting wear has been said to be attributable to contact point displacement caused by vibration during engine drive and automobile running, and thermal expansion and contraction due to, for example, temperature changes in the surrounding environment and heat generated by energization.[1, 6] As the miniaturization of terminals progresses, the contact load at the contact points decreases, making the contact points more prone to displacement due to vibration and impact that hitherto have not been a problem, increasing the importance of fretting wear resistance.

Fig. 5 shows a schematic diagram of the fretting wear test, and **Fig. 6** shows the contact resistance behavior during the fretting wear test at loads of 3 N and 5 N for reflow tin plating. For the load of 3 N, a peak of contact resistance (first peak) is observed around 40 to 80 cycles, but this is different for the load of 5 N. In the fretting wear of tin plating, the wear debris of tin is generated by sliding, and, although some of the wear debris is discharged outside, the rest accumulates between the contact points. The accumulated wear debris of tin oxidizes, increasing the contact resistance.[1] After that, when wear progresses as far as the copper-tin-based intermetallic compound, more wear debris is discharged than is generated, decreasing the wear debris accumulated at the contact points and decreasing the contact resistance (first peak). Further sliding causes wear to progress, exposing the copper alloy base material, and finally contact resistance increases due to the wear and oxidation of the base material.[1] The first peak of contact resistance observed at the load of 3 N is considered to be caused by the small contact load weakening the force to discharge the wear debris to the outside, making it easy to accumulate. Thus, in the case of

※Yamasaki seiki CRS-B1050CHO

Conditions
Flat: Reflow plating, Emboss: Specimen
Curvature radius: 1.0 mm, Current: 10 mA
Sliding distance: 50 μm, Sliding frequency: 1 Hz
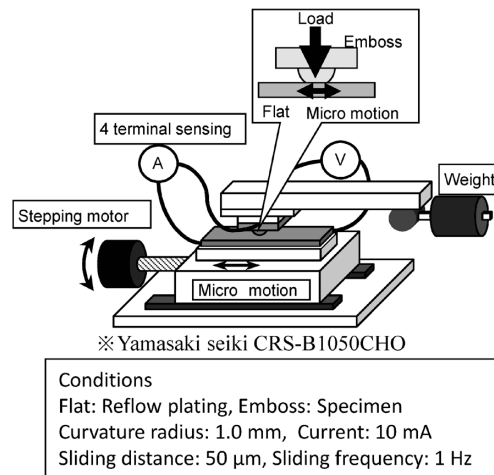
Fig. 5 Fretting test system
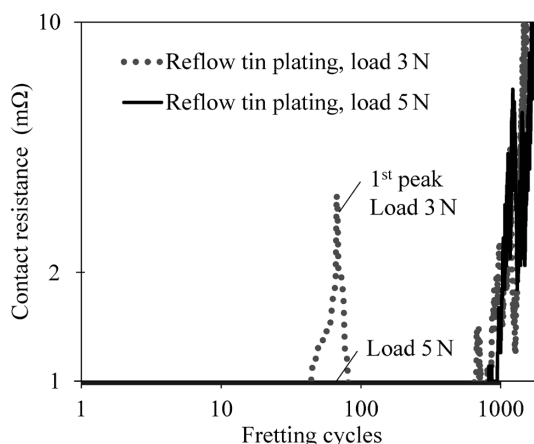
Fig. 6 Changes of contact resistance of reflow tin plating with different contact load

fretting wear, the lower the load, the easier it is for the wear debris to accumulate, which tends to increase the first peak value of the contact resistance. Therefore, plating is required to suppress the first peak of contact resistance at a low load. The first peak of contact resistance is due to the accumulation and oxidation of tin wear debris, and in order to lower the first peak of contact resistance, the generation and accumulation of wear debris must be suppressed. To this end, it is effective to reduce the thickness of tin plating, which is the source of wear debris, or to suppress tin wear.

Fig. 7 shows the relationship between the tin plating thickness of new reflow plating and reflow tin plating at the load of 3 N and the first peak contact resistance in fretting wear. Here, the tin plating thickness is the average thickness of the tin layer only, excluding the copper-tin-based intermetallic compound. For either type of plating, reducing the tin thickness lowers the first peak. The reason for this is considered to be the decrease in the amount of tin wear debris generated. When homogeneous metals are rubbed against each other,

Fig. 7 Relationship between tin plating thickness and 1st peak of contact resistance

adhesion generally tends to occur, making the wear severe (adhesive wear).[9] Thus, the primary cause of wear between two layers of tin plating is regarded as a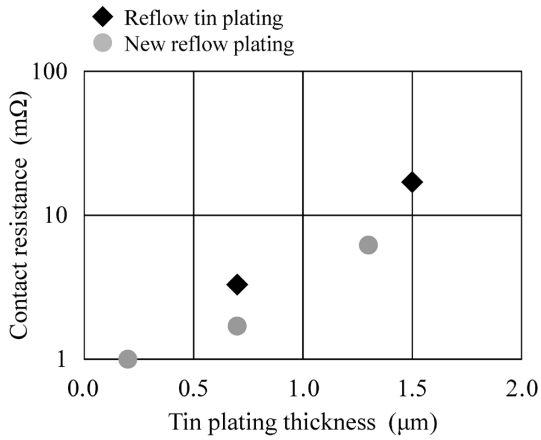dhesive wear. The new reflow plating exposes the copper-tin intermetallic compound on the surface to suppress the adhesive wear of tin. At around 0.7 μm tin thickness in Fig. 7, the new reflow plating has a lower first peak than the reflow tin plating. This is considered to be attributable to the effect, described above, of suppressing the adhesive wear of tin.

1.4 Terminal insertability

In recent years, the number of terminals per connector has increased, and the connector insertion force has increased accordingly. Since the work of inserting connectors is done manually, there is a move to tighten the insertion force standard to reduce the burden on workers, and reducing the insertion force of the connector is considered to become even more critical in the future. Since the friction force of the tin plating affects the insertion force of the connector, a reduction in the coefficient of friction is required for the tin plating.

Friction force is expressed as the sum of a force component required to separate the adhered parts (adhesive friction), a force component due to a hard surface digging into a soft surface (friction due to digging), and a component based on the energy loss caused by the difference in deformation force when pushing and pulling the material (elastic hysteresis loss).[1] In general, the difference in hardness of two layers of tin plating has little effect on the friction between them, the friction caused by digging is slight, and the adhesive friction becomes dominant. Therefore, the coefficient of friction is given by Equation (3):[9]

$$\mu = F/W = As/Ap = s/p \cdots\cdots\cdots\cdots\cdots\cdots\cdots\cdots (3)$$

wherein F is the friction force (N), W is load (N) in the direction normal to the plate thickness, A is the contact area (m^2), s is the shear strength of adhered part (N/mm^2), p is the plastic flow pressure (N/mm^2) = hardness of the material (N/mm^2).

The plastic flow pressure is the pressure at which the entire interior close to the surface near the contact part undergoes plastic deformation when the contact load is increased and corresponds to the hardness of the material.[1] According to Equation (3), the coefficient of friction can be reduced by lowering the shear strength of the adhered part and/or increasing the plastic flow pressure.

Fig. 8 is a schematic diagram of the method for measuring the coefficient of friction. The coefficient of friction was measured following the Japan Copper and Brass Association technical standard JCBA T311:2002. A plate-shaped test piece (Flat) and a test piece with a hemispherical protrusion with a radius of curvature of 1.0 mm (Emboss) were brought into contact, and the coefficient of friction was calculated from the friction force when a load of 3 N was applied in the normal direction of the plate surface.

Fig. 9 shows the relationship between tin thickness and coefficient of friction for new reflow
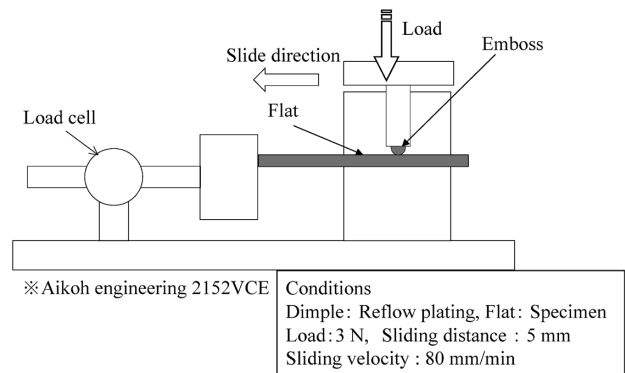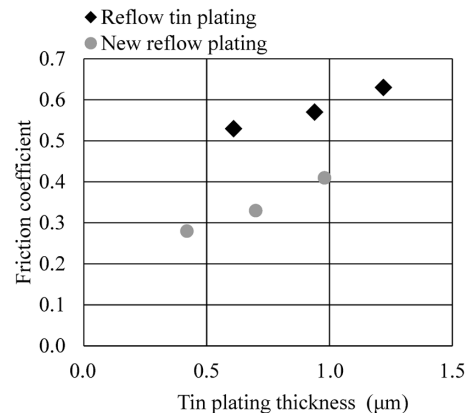

Fig. 8 Friction coefficient measurement system

Fig. 9 Relationship between tin plating thickness and friction coefficient

plating and reflow tin plating. For both cases of plating, the thinner the tin layer, the lower the coefficient of friction becomes. Thinning the tin layer makes the plating more susceptible to the rigid base material, increasing the apparent hardness and decreasing the coefficient of friction by suppressing the adhesive wear of the tin. Also, the new reflow plating results in a coefficient of friction lower than that of the reflow tin plating. The new reflow plating has a copper-tin-based intermetallic compound exposed on the surface, and the hard copper-tin-based intermetallic compound increases the apparent plating hardness and suppresses the adhesive friction of the tin, which is considered to have reduced the coefficient of friction.

2. Introduction to new reflow plating (heat resistant specifications, low friction specifications)

The following introduces a new reflow plating (heat resistant specifications) that has improved heat resistance by varying the tin thickness compared with the standard new reflow plating and a new reflow plating (low friction specification), especially with improved terminal insertability.

2.1 Developmental approach to tin plating for terminals

Fig.10 shows the positioning of tin plating for terminals with respect to terminal insertability and heat resistance. As mentioned above, increasing the tin thickness improves the heat resistance, but on the other hand, the terminal insertability and the fretting wear resistance characteristics decline. Therefore, it is difficult to achieve both by controlling the tin plating thickness alone. The new reflow plating simultaneously achieves various characteristics that were difficult to attain with conventional reflow

tin plating by having a three-layered structure and finely dispersed copper-tin-based intermetallic compound on the surface of the tin plating, and it has been adopted for automobile terminals.

However, with the recent changes in automobiles, the characteristics required for tin plating used for automobile terminals are becoming more stringent. Kobe Steel has developed a new reflow plating with heat-resistant specifications and low friction specifications as new variations in response to the increasing demand for heat resistance and terminal insertability.

2.2 New reflow plating (heat resistant specifications)

For improved heat resistance, the new reflow plating (heat resistant specifications) has a greater thickness of tin than the standard new reflow plating.

Fig.11 shows the contact resistance at a vertical load of 1 to 5 N when held at 160℃ for 1,000 h and 5,000 h. The contact resistance after 5,000 h of reflow tin plating is higher than after 1,000 h. This is presumed to be due to the thick growth of copper
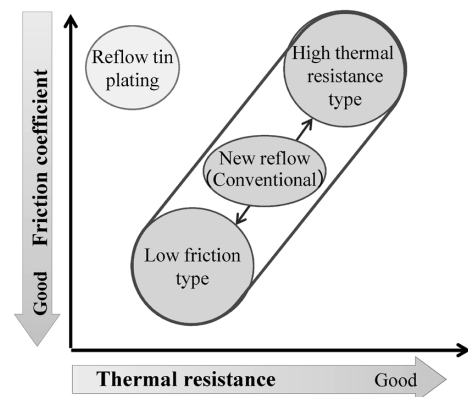
Fig.10 Positioning of friction coefficient and thermal resistance of tin plating for terminals
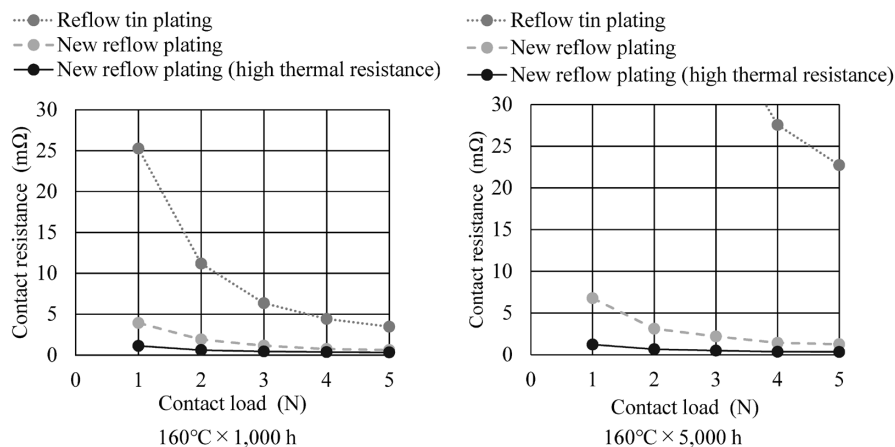
Fig.11 Relationship between contact load and contact resistance before and after 160℃×1,000 h and 5,000 h annealing

oxide. On the other hand, the new reflow plating (heat resistant specifications) maintains a contact resistance of 1 mΩ or less at load 1 N even after 5,000 hours and is more heat resistant than the new reflow plating. This is considered to be because thicker tin maintained the tin and Cu_6Sn_5 for a longer period than the new reflow plating did, suppressing the generation of copper oxide.

Fig.12 shows the relationship between the square root of the tin plating holding time at 160℃ and the thickness of the copper-tin-based intermetallic compound. The linear approximation of the plots has been extrapolated to obtain the growth rate of the copper-tin-based intermetallic compound. As mentioned above, increasing the tin thickness effectively improves the heat resistance. Therefore, the change in the time required for the tin to disappear when the tin thickness is increased from 1 μm to 1.5 μm has been calculated from the linear approximation of the growth rate of the copper-tin-based intermetallic compound. As a result, it was found that the reflow tin plating increases the disappearance time of tin by approximately 40 hours, whereas the new reflow plating significantly lengthens it to approximately 2,900 hours. Therefore, increasing the tin thickness of the new reflow plating is more effective in improving the heat resistance.

Fig.13 shows the coefficient of friction for the reflow tin plating and new reflow plating (heat resistant specifications). As mentioned above, the coefficient of friction increases as the tin plating thickness increases. The new reflow plating (heat resistant specifications) shows a coefficient of friction similar to that of the reflow tin plating, despite the thicker tin. The new reflow plating has the advantage of a coefficient of friction lower than that of the reflow tin plating. Hence, the new reflow plating (heat resistant specifications) has set the tin thicker than in the new reflow plating by determining the extent to which the coefficient of

friction is equivalent to that of the reflow tin plating.

The new reflow plating (heat resistant specifications) is suitable for applications requiring improved heat resistance and maintenance of terminal insertability in high-temperature environments.

2.3 New reflow plating (Low friction specifications)

The new reflow plating (low friction specifications) has reduced tin thickness in comparison with the standard new reflow plating for improved terminal insertability.

Fig.14 shows the coefficient of friction of tin plating. The bar graph represents the average value of ten measurements, and the error bar indicates the maximum and minimum values. The new reflow plating (low friction specifications) exhibits a lower coefficient of friction than the standard new reflow plating and is more consistent with less variability.

Fig.15 shows the behavior of the friction force of tin plating. Several small peaks are observed with the reflow tin plating and new reflow plating, but few peaks are observed with new reflow plating (low friction specifications). As mentioned above, tin plating results mainly in adhesive friction. Adhesive friction is a phenomenon of repeated sticking and

Fig.13 Friction coefficient of tin plating

Fig.12 Growth of intermetallic compound layer at 160℃
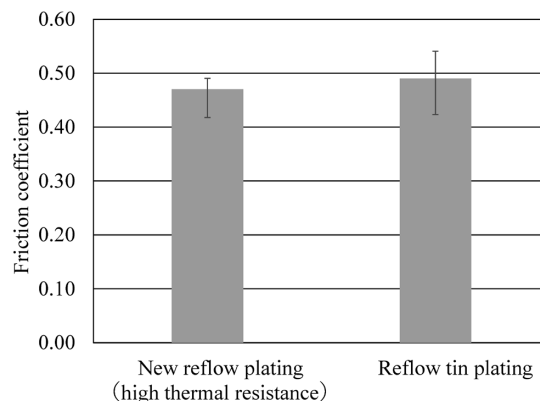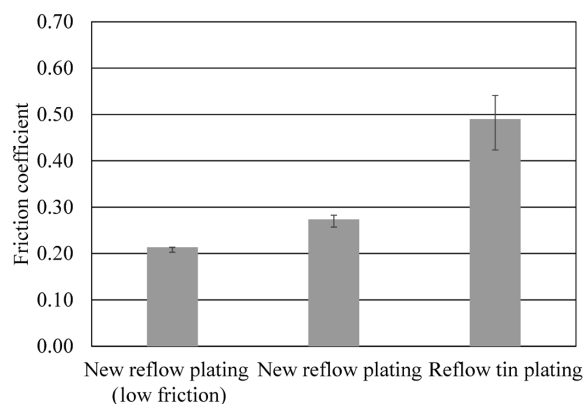
Fig.14 Friction coefficient of tin plating
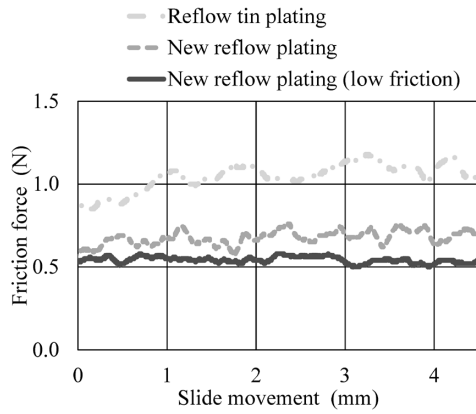
Fig.15 Change of friction force of tin plating
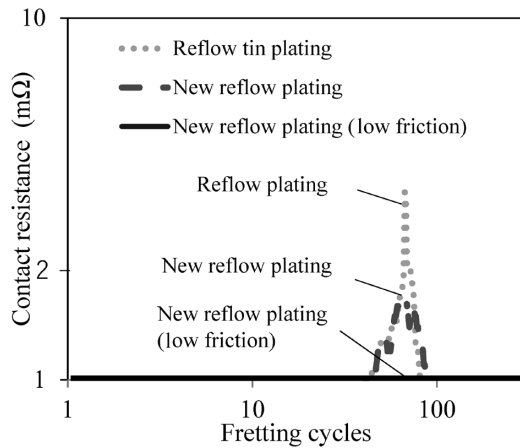
Fig.16 Changes of contact resistance of reflow plating

Fig.17 Relationship between contact load and contact resistance before and after 160℃×1,000 h annealing

Conclusions

The new reflow plating is a type of plating with improved heat resistance, fretting wear resistance, and terminal insertability compared with the conventional reflow tin plating and its use in tin plating for automobile terminals is spreading. Kobe Steel has added heat resistant specifications and low friction specifications as new variations of the new reflow plating. Utilizing these, the company will strive to propose tin plating suitable for the usage environment.

References

1) M. Tsuru et al. R&D Kobe Steel Engineering Reports. 2012, Vol.62, No.2, pp.59-62.
2) Latest Connector Technology '99 Editorial Committee. Latest Connector Technology '99. First edition. Japan Advanced Technology Co., Ltd., 1999, pp.1-3.
3) T. Tamai et al. IEICE Technical Report. EMD2008-2, pp.7-12.
4) S. Izumi. ESPEC Test Navi Report. 1997, No.9, pp.5-11.
5) S. Sawada. SEI TECHNICAL REVIEW. 2010, Vol.177, pp.36-42.
6) H. Sakamoto. R&D Kobe Steel Engineering Reports. 2019, Vol.69, No.1, pp.19-24.
7) G. V. Samsonov. The Oxide Handbook.-Physicochemical Properties-. 2nd Revised and Enlarged Edition, Japan-Soviet Press, 1979, p.209.
8) T. Hara et al. R&D Kobe Steel Engineering Reports. 2004, Vol.54, No.1, pp.9-12.
9) Y. Yamamoto et al. TRIBOLOGY. 2nd edition, Ohmsha Ltd., 2010, pp.41-42, pp.193-194.

breaking,[9] and it is presumed that the small peaks of friction force have been caused by the repetition of the adhesive friction of tin. The new reflow plating (low friction specifications) achieves even lower friction and variability suppression by reducing the tin thickness and suppressing the adhesive friction of tin.

Fig.16 shows the contact resistance behavior during the fretting wear test of tin plating. The new reflow plating (low friction specifications) reduces the first peak even more than the new reflow plating by reducing the tin thickness.

Fig.17 shows the contact resistance of tin plating after holding at 160℃ for 1,000 h. The new reflow plating (low friction specifications) has slightly higher contact resistance at load 1 N than the new reflow plating but is more heat resistant than the reflow tin plating. This is because the three-layered structure suppresses the diffusion of copper.

The new reflow plating (low friction specifications) is suitable for applications with exceptionally high insertion force specifications and where fretting wear resistance is required.
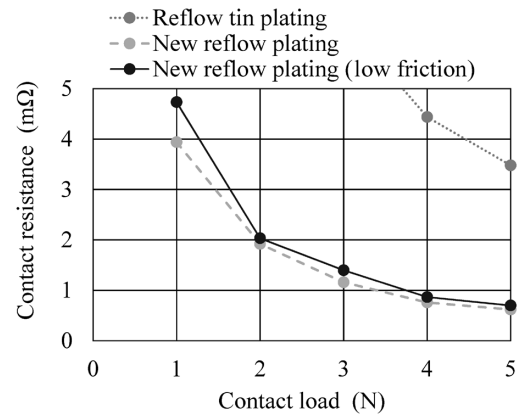
Stabilization of Characteristics by Hydrogen Plasma Treatment for Top-gate Thin-film Transistor Using High-mobility Oxide Semiconductor, a-IGZTO

Dr. Kohei NISHIYAMA[*1] ・ Dr. Mototaka OCHI[*1] ・ Yumi TERAMAE[*2] ・ Hiroshi GOTO[*3]

[*1] Applied Physics Research Laboratory, Technical Development Group
[*2] Applied Physics Research Laboratory, Technical Development Group (currently Osaka Branch Office)
[*3] Kobelco Research Institute, Inc.

Abstract

Top-gate thin film transistors (TFTs) using a high mobility oxide semiconductor, amorphous In-Ga-Zn-Sn-O (a-IGZTO), are attracting much attention in the field of flat panel displays. Here, the effectiveness of hydrogen plasma treatment for the formation process of low electrical resistance source/drain has been clarified. The hydrogen plasma treatment has reduced the sheet resistance of an a-IGZTO film, and this low resistance state has demonstrated high stability under heat treatment. An X-ray photoelectron spectroscopy confirmed the OH group's existence after argon plasma irradiation, suggesting that a-IGZTO has been physically sputtered. Meanwhile, it has been shown that hydrogen plasma irradiation causes the a-IGZTO to be reduced by hydrogen radicals, the reduction reaction producing metallic components. This reduction reaction is considered to have made the top-gate type TFT treated by hydrogen plasma more stable under heat treatment.

Introduction

New technologies, such as big data, AI, IoT, and automated driving, enrich our society more and more. Electronic devices support this digital society, and one of the essential elements is transistors, which have a current control function. Before transistors, vacuum tubes were used in electronic devices, but they could not be made smaller. The invention of transistors paved the way for miniaturization and high performance, and today we live in a society that uses electronic devices in all aspects of life. Silicon is often used as the semiconductor material for transistors, and the history of electronic devices can be described as a history of the evolution of transistors based on silicon. In the field of displays, one of the electronic devices, thin film transistors (hereinafter called "TFTs") using amorphous silicon (hereinafter called "a-Si"), which can be manufactured in large areas at low costs, are widely used. In recent years, oxide materials that exhibit semiconductor characteristics (hereinafter referred to as "oxide semiconductors") have been proposed as new materials, other than silicon, to meet the increasing demand for higher-performance TFTs. Oxide semiconductors are materials that can achieve 20 times higher mobility than a-Si TFTs, while having the same capability as a-Si to form a thin film over a large area. For example, amorphous In-Ga-Zn-O (a-IGZO)[1), 2)] and amorphous In-Ga-Zn-Sn-O (a-IGZTO)[3), 4)] with higher mobility are mass-produced as semiconductor materials for LCDs used in TVs, tablets, and notebook PCs. Recently, their application to Organic Light Emitting Diodes (OLEDs) has been increasing, and further expansion into the semiconductor field, such as memory, is also being considered. Kobe Steel has been developing oxide semiconductor materials and TFT processes in response to this market expansion.

In OLEDs, which are current-driven, the parasitic capacitance of the TFT must be reduced to stabilize the characteristics. In order to reduce parasitic capacitance, it is essential to change the TFT structure from the conventional bottom-gate structure to a top-gate (also called planar) structure.[5)] One of the most significant differences between the top-gate and bottom-gate structures is in making the oxide semiconductor layer conductive (semiconductor-conductor conversion process). In the top-gate structure, the resistance of the oxide semiconductor film can be selectively reduced by masking the gate electrode and applying semiconductor-conductor conversion. Using this low-resistance region as a source/drain region (hereinafter referred to as an "S/D region") advantageously eliminates the overlap between the gate electrode and the S/D region, thereby reducing parasitic capacitance. However, to a function as a TFT, it is necessary to create regions with two types of characteristics, semiconductor and conductor, within a single activation layer (e.g., a-IGZTO). Several methods have been proposed to form the S/D region, including plasma treatment,[6)-9)] reaction with aluminum,[10), 11)] ion implantation,[12), 13)] and laser exposure.[14)] Among these, hydrogen plasma exposure is expected to cause less physical damage to oxide semiconductors because of the lighter mass of hydrogen. In addition, oxide semiconductors tend to be converted easily into conductors in the presence of hydrogen,[15)] and this tendency is more

pronounced in high mobility materials; so hydrogen plasma exposure is expected to entail low resistance. In addition, it is known that oxide semiconductors generally have increased conduction carriers due to oxygen deficiency. However, heat treatment can adjust the number of carriers to an appropriate level and improve TFT characteristics.[16] Hence, a semiconductor-conductor conversion process that is stable against heat treatment during fabrication is required.

Hence, Kobe Steel has developed a fabrication process for the high mobility oxide semiconductor a-IGZTO, using hydrogen plasma with a wide process window for heat treatment. This paper shows that the transfer characteristics of a top-gate TFT that has undergone hydrogen plasma treatment include excellent heat resistance. Also reported are the study's results using X-ray Photoelectron Spectroscopy (XPS) on the source-drain formation mechanism by hydrogen plasma treatment.

1. Experimental method

In order to evaluate the sheet resistance and chemical bonding state of an a-IGZTO film, 40 nm thick films of a-IGZTO were deposited by DC magnetron sputtering on glass substrates under gas pressure of 0.13 Pa and an $O_2/(Ar+O_2)$ flow ratio of 4%. The deposited a-IGZTO films were heat treated at 350℃ for 1 h in air and exposed to argon or hydrogen plasma. For plasma exposure, parallel-plate plasma apparatuses with different RF power were used. Sheet resistance was measured for each plasma-exposed film by a four-point probe method before the XPS measurement.

Fig. 1 shows the cross-sectional structure corresponding to each fabrication step of a-IGZTO-TFT used to evaluate transfer characteristics and the test element group (TEG) to evaluate sheet resistance change during the fabrication process. A buffer layer of SiO_2 was formed on a glass substrate by plasma-enhanced chemical vapor deposition (hereafter referred to as PE-CVD.) Then a-IGZTO was deposited to form a film 40 nm thick by DC magnetron sputtering with the substrate temperature set to room temperature, followed by patterning by wet etching. Subsequently, after heat treatment at 350℃ for 1 h in the atmosphere, a SiO_2 gate insulator (hereinafter referred to as "GI") films of 150 nm were deposited by PE-CVD
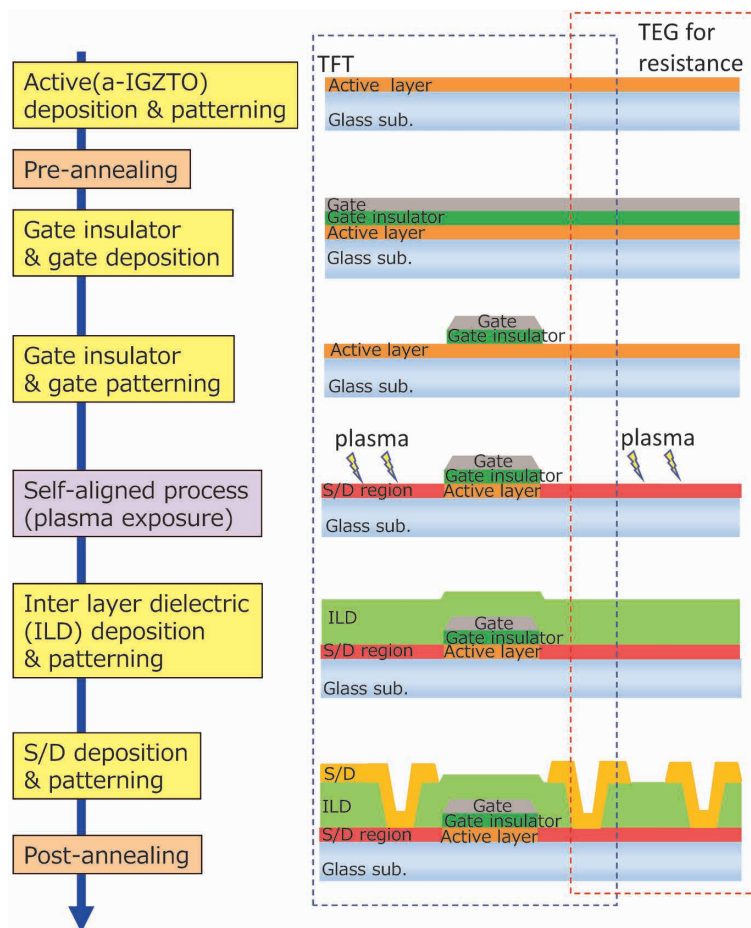

Fig. 1 Fabrication flow and cross-sectional schematics of top-gate TFT and test element group (TEG) for resistance

at temperatures from 250 to 300℃ using a SiH$_4$/ N$_2$O gas mixture. Next, the Mo gate electrode was deposited by DC magnetron sputtering, the gate electrode was patterned by wet-etching, and the gate insulator film was patterned by reactive ion etching (RIE). Furthermore, the S/D region was formed by exposing the oxide semiconductor surface to argon or hydrogen plasma, using the gate electrode as a mask. Then, an SiO$_2$ protective film was formed by PECVD, and contact holes were formed by dry etching. This was followed by forming S/D electrodes of Mo alloy by DC magnetron sputtering. Transfer characteristics were measured with a semiconductor parameter analyzer. The test element group (TEG) for resistance, which underwent the same process as the TFT, was also measured to evaluate the change in electrical resistance of the S/D region.

2. Experimental results and discussions

2.1 Stability of TFT transfer characteristics under heat treatment

Fig. 2 shows the dependence of sheet resistance on the plasma exposure time when argon plasma

treatment and hydrogen plasma treatment are applied to an a-IGZTO thin film deposited on a glass substrate. The sheet resistance of the a-IGZTO thin film after film deposition and heat treatment (pre-anneal) is approximately 10^4 kΩ/□, and the sheet resistance has decreased significantly in both of the plasma treatments. Even an exposure time as short as 15 s is considered sufficient.

Fig. 3 shows the plasma exposure time dependence of TFT transfer characteristics using the hydrogen plasma exposure process. As confirmed by the sheet resistance measurement, excellent TFT transfer characteristics were obtained even with a short plasma exposure time. In addition, a slight shift of the threshold voltage to the negative voltage direction is observed as the plasma exposure time increases.

Fig. 4 (a) shows the stability of drain current against a heat treatment, post-annealing, of TFTs with argon plasma and hydrogen plasma exposure. At post-annealing temperatures below 200℃, there is no decrease in drain current for either argon plasma-exposed or hydrogen plasma-exposed TFTs. However, for the argon plasma-exposed TFT, the drain current decreased rapidly with the increasing post-annealing temperature above 200℃. On the
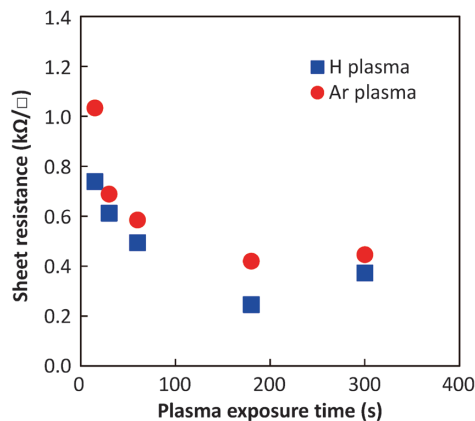

Fig. 2 Dependence on plasma exposure time of sheet resistance on oxide semiconductor (a-IGZTO)

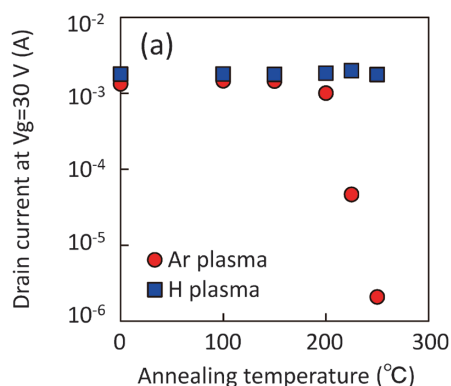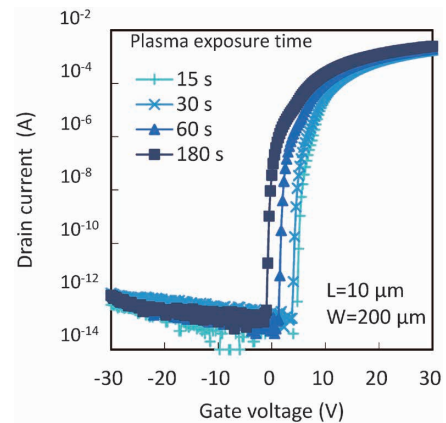Fig. 3 Dependence of hydrogen plasma exposure time of Id-Vg curve of top-gate TFT

Fig. 4 (a) Dependence on annealing temperature of drain current, (b) Relation of drain current vs. sheet resistance on S/D region of a-IGZTO
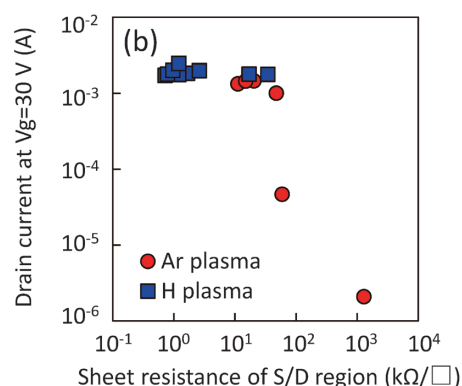
other hand, the TFT exposed to hydrogen plasma shows no decrease in the drain current at least up to 250℃. In order to discuss the change in drain current due to the difference in the plasma exposure methods, the relationship between drain current and sheet resistance in the S/D region is shown in Fig. 4(b). The sheet resistance in the S/D region was measured for TFT devices on the same substrate (devices fabricated in the same process), as shown in Fig. 1. When the sheet resistance in the S/D region exceeds approximately 50 kΩ, there is a sharp drop in the drain current. Since this value of 50 kΩ corresponds to the conductivity required for 1 mA flow in Kobe Steel's TFT structure, it is considered that the resistance in the S/D region increased due to the heat treatment, becoming a resistance component and causing a rapid decrease in drain current.

2.2 Consideration of formation mechanism of S/D region, using XPS analysis

Oxidation of the constituent elements of an a-IGZTO is suspected to be the cause of the increased resistance of the oxide semiconductor. In order to capture the changes in chemical state such as oxidation-reduction, the changes in the bonding state of oxide semiconductors exposed to hydrogen plasma and argon plasma, respectively, were examined by XPS analysis. The effect of the TFT fabrication process was evaluated. The heat-treated a-IGZTOs were exposed to a CHF_3/Ar mixed gas plasma that simulates dry etching of a gate-insulating film by the RIE process (hereinafter referred to as RIE plasma.) Then, for a chemical derivatization, they were exposed to argon plasma and hydrogen plasma, respectively, before being subjected to XPS analysis. Among the a-IGZTO constituent elements, focus was placed on In as the carrier source. A comparison was made on the effect of plasma treatment on In 3 $d_{5/2}$ peak, which has a relatively significant difference in chemical shifts among metals, oxides, and hydroxides (**Fig. 5**). The In 3 $d_{5/2}$ peak was separated using the peaks at 443.73 eV corresponding to metallic In, 444.65 eV corresponding to In_2O_3, and 445.13 eV corresponding to $In(OH)_3$. Each peak's full width at half maximum (FWHM) was set to 1.8 eV. The FWHM was assumed to remain unchanged due to the process. Before the plasma treatment, the peak at 444.65 eV corresponding to In_2O_3 is dominant (Fig. 5(a)). In contrast, a peak at 445.13 eV corresponding to $In(OH)_3$ hydroxide grows in a (CHF_3/Ar) mixed gas simulating the RIE plasma process for gate insulating film (Fig. 5(b)). In the case of RIE plasma, fluorine radicals, hydrogen radicals, and argon ions exist in the plasma. Therefore, the reaction of the oxide semiconductor with fluorine radicals (or C-Fx), the reaction with hydrogen radicals, and the sputtering effect of argon ions are considered to act in a combined manner. Next, the effect of plasma
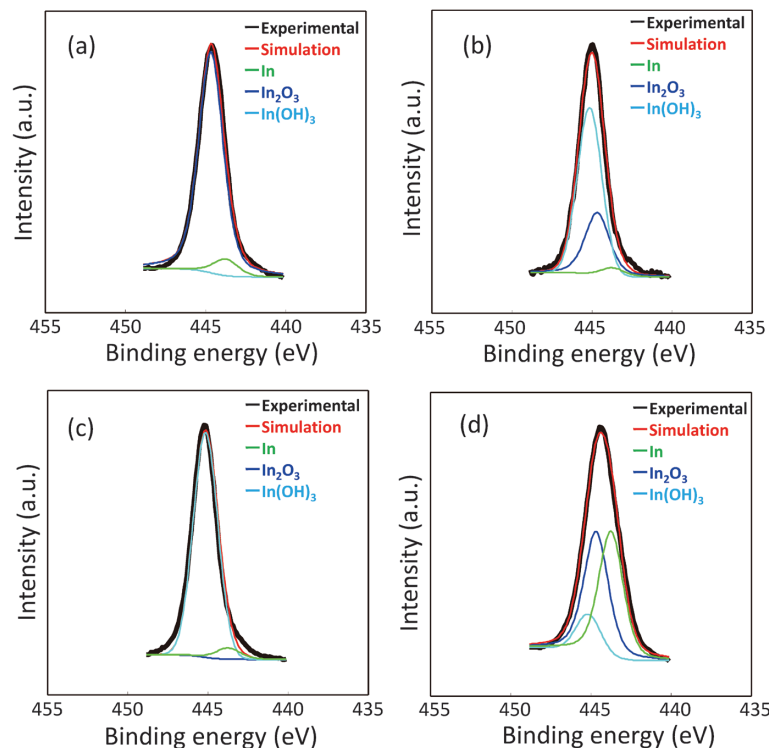

Fig. 5 In $3d_{5/2}$ peaks of XPS spectra on the a-IGZTO thin film surfaces, (a) no plasma exposure, (b)after RIE, (c) RIE and argon plasma, and (d) RIE and hydrogen plasma exposure

exposure was confirmed. As shown in Fig. 5 (c), the peak corresponding to In(OH)$_3$ increases after argon plasma exposure. On the other hand, as shown in Fig. 5(d), after hydrogen plasma exposure, the In 3 d$_{5/2}$ peak significantly shifts to the low energy side, the ratio of the hydroxide peak decreases, and the peak indicating metallic bonding appears. This result suggests the reduction of In by hydrogen plasma exposure. It should be noted that similar results have been obtained when the RIE plasma process is omitted, indicating that there is little influence of the RIE plasma process and the semiconductor-conductor conversion process is dominant.

On the basis of these results, the possible mechanisms of the effects of argon plasma exposure and hydrogen plasma exposure on a-IGZTO are shown in **Fig. 6**. The effect of argon plasma treatment is presumed to be physical sputtering of the surface by argon ions. The surface is sputtered, and the deficiency of oxygen, serving as a carrier source, is considered to cause low resistance.[8] It should be noted, however, that because of the large mass of argon ions, oxygen atoms, and all atoms constituting a-IGZTO (In, Ga, Zn, Sn, and O) are sputtered to form dangling bonds. It is assumed that the topmost surface of a-IGZTO is modified with OH groups by subsequent exposure to moisture in the atmosphere, as observed by XPS. On the other hand, since the mass of hydrogen atoms is much smaller than that of argon atoms, the hydrogen plasma treatment should bring on a much smaller physical sputtering effect on the a-IGZTO surface. In hydrogen plasma, hydrogen cation

(proton) generated by the ionization of hydrogen removes O or OH groups from the surface of the a-IGZTO. In other words, the reduction of In-O bonding and the formation of metallic bonding are considered to have increased the number of carriers and decreased the electrical resistance in the S/D region. Thus, although the same resistance reduction phenomenon occurs on a-IGZTO, the argon plasma treatment and hydrogen plasma treatment have different resistance reduction mechanisms, which is considered to have caused the difference in the effect on the TFT characteristics. Thermal desorption spectrometry (TDS) of a-IGZTO shows that the desorption of the OH group begins at around 100℃, and desorption of In is observed at 400℃ and above. Therefore, the In-In bond is presumed to be more stable than the In-OH bond. As shown in Fig. 3, the threshold voltage of the TFT tends to shift in the negative voltage direction as the hydrogen plasma exposure time is increased. The fact that the TFT characteristics were affected even though the channel was not exposed to the plasma suggests that the proton from the hydrogen plasma penetrated the a-IGZTO film. Based on the above results, hydrogen plasma treatment produces a more stable metal component on the a-IGZTO surface than argon plasma treatment, making the surface less susceptible to oxidation by subsequent heat treatment. The effect of the oxidation on the material's surface extends to the interior, and the low resistance state of the interior is maintained even when the surface is oxidized, indicating high heat resistance, as shown in Fig. 4.
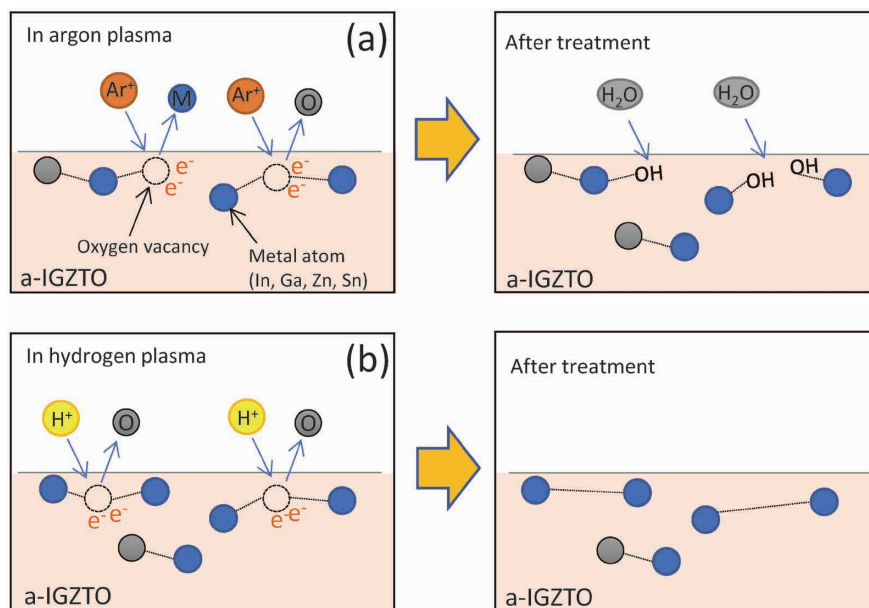

Fig. 6 Schematic representation of a possible mechanism to explain the difference between the (a) argon and (b) hydrogen plasma exposure

Conclusions

A high-mobility a-IGZTO TFT with a top-gate structure for OLEDs has been shown to have a wide process window for heat treatment when fabricated using hydrogen plasma. In the semiconductor-conductor conversion using hydrogen plasma, XPS analysis has shown that the metal component increases due to the reduction of oxide semiconductors by a proton. As a result, it has been found that the insulator-conductor conversion state of a-IGZTO is stabilized, and the increase in electrical resistance due to heat treatment is suppressed.

This paper has reported on the latest materials and process influences on oxide semiconductors for displays. In the field of electronic devices such as semiconductor memories, the application of oxide semiconductors has begun to be investigated for higher performance, and the evaluation results for semiconductor memory using Kobe Steel's a-IGZTO have been reported.[17] The knowledge of process design guidelines based on material development and analytical techniques obtained in the development of oxide semiconductors can also be applied in this field. Kobe Steel will strive to contribute to the further expansion of the use of oxide semiconductors.

References

1) K. Takechi et al. J. Appl. Phys. 1998, Vol.84, pp.3993-3999.
2) K. Nomura et al. Nature. 2004, Vol.488, p.432.
3) M. Ochi et al. Proc. IDW'18. 2018, p.308.
4) Y. Goto et al. Tech_library KOBELCO research institute. 2020, No.50, pp.21-24.
5) Thin Film Materials and Devices Research Group ed. Thin Film Transistors. CORONA PUBLISHING CO., LTD., 2008, p.229
6) J. Park et al. Appl. Phys. Lett. 2008, Vol.93, pp.053501-1-053501-3.
7) H. Lu et al. Proc. 2016 23rd International Workshop on Active-Matrix Flatpanel Displays and Devices. 2016, pp.131-134.
8) Y. Magari et al. ECS J. Solid State Sci. Technol. 2017, Vol.6, pp.Q101-Q107.
9) H. Tsuji et al. IDW '20. 2020, pp.149-150.
10) N. Morosawa et al. Jpn. J. App. Phys. 2011, Vol.50, Article096502.
11) T. Liang et al. IEEE J. Electron Devices Soc. 2018, Vol.6, pp.680-684.
12) Z. Ye et al. IEEE Tran. Electron Devices. 2012, Vol.59, pp.393-399.
13) R. Chen et al. IEEE Electron Device Lett. 2012, Vol.33, pp.1150-1152.
14) M. Nakata et al. IEEE Transactions on Industry Application. 2017, Vol.53, pp.5972-5977.
15) M. Nakata et al. Jpn. J. Appl. Phys. 2019, Vol.58, No.9, Article090602.
16) S. Morita et al. R&D Kobe Steel Engineering Reports. 2015, Vol.65, No.2, pp.72-77.
17) J. Wu et al. IEEE Transactions on Electron Devices. 2021, Vol.68, Issue12, pp.6617-6622.

Technical Trends in, and Analysis of Evaluation Technologies of Secondary Batteries

Dr. Takayuki TSUBOTA[*1] · Dr. Takashi ACHIHA[*1] · Yoshiki HAYASHI[*1] · Dr. Takuya MORI[*1] · Hiroshi OZONO[*1]
Hidemasa TSUNEISHI[*1]

[*1] Kobelco Research Institute, Inc.

Abstract

The shift toward electric vehicles (EV shift) is being accelerated worldwide to reduce CO_2 emissions during running. In addition, more renewable energy is being introduced, increasing the demand for secondary batteries. Against this backdrop, studies are being conducted to increase the energy density of lithium-ion batteries for EVs and stationary battery storage. The company is also focusing on developing new batteries, e.g., all-solid-state batteries that can further improve energy density and sodium-ion batteries that use sodium instead of lithium, a rare metal. Kobelco Research Institute supports the development of batteries through its evaluation/analytics technologies, including "the prototype production of lithium-ion batteries, all-solid-state batteries, and sodium-ion batteries," "battery characteristics evaluation technology," "reaction distribution analysis technology in battery cells," "redox reaction analysis technology," and "non-destructive deterioration diagnosis technology for reuse," thus contributing to the realization of carbon neutrality.

Introduction

Decarbonization is accelerating globally. The Paris Agreement, adopted at the 21st Conference of the Parties to the United Nations Framework Convention on Climate Change held in 2015, sets a common long-term global goal of keeping the average temperature rise well below 2℃ above pre-industrial levels and pursuing efforts to limit global warming to 1.5℃." The 2021 Intergovernmental Panel on Climate Change 6th Assessment Report concludes that "there is no doubt that human influence has warmed the atmosphere, oceans and land." The EU, promoting decarbonization, has announced that it will reduce greenhouse gas emissions to virtually zero by 2050. In Japan, there was a declaration of "2050 carbon neutral, the realization of a decarbonized society," and in April 2021, the greenhouse gas reduction target was significantly raised to "reduce emissions in 2030 by 46% compared to 2013."

These trends of decarbonization have a significant impact on the automobile industry, which is a critical core industry that supports the Japanese economy. Europe has announced a policy to ban the sale of gasoline and diesel vehicles, including hybrid vehicles, by 2035 and is ambitiously promoting the shift to electric vehicles (EVs). The secondary battery, a component of an electric powertrain, is a critical device that greatly affects the driving performance of automobiles, such as cruising distance and acceleration. Research and development for high energy density and high input/output are accelerating.

This paper describes the technological trends of lithium-ion batteries, including the next generation, and the latest analytical evaluation and analysis technology at the Kobelco Research Institute.

1. Technological trend of liquid lithium-ion secondary batteries

Lithium-ion batteries are smaller, lighter, and have higher voltage and energy density than conventional aqueous secondary batteries such as nickel-metal hydride batteries. In addition to small batteries for mobile devices, in recent years their application has expanded to in-vehicle batteries such as those for EVs and stationary large storage batteries. Akira Yoshino, the 2019 Nobel Laureate in Chemistry, established the fundamental concepts in 1985, including the structure of the lithium-ion battery with lithium cobalt oxide ($LiCoO_2$) as the cathode and carbon material as the anode, the cathode aluminum foil current collector, and the olefin microporous membrane for the shutdown function during heat generation.[1] Later, in 1991, Sony Energytech Inc. (currently Sony Energy Devices Corporation) put lithium-ion batteries into practical use. A schematic diagram of the lithium-ion battery is shown in **Fig. 1**. In an example of a battery with lithium cobaltate for the cathode and graphite for the anode, the reaction of a lithium-ion battery during charging consists of the occurrence of the desorption of Li^+, releasing electrons from the cathode to the external circuit and inserting them into the anode through the electrolyte. Conversely, during discharge, the desorption of Li^+ occurs at the anode, with electrons being inserted into the cathode. The reaction equation is shown below. This is a simple reaction in which Li^+ moves back and forth between the cathode and anode, which is called a "rocking-chair reaction."
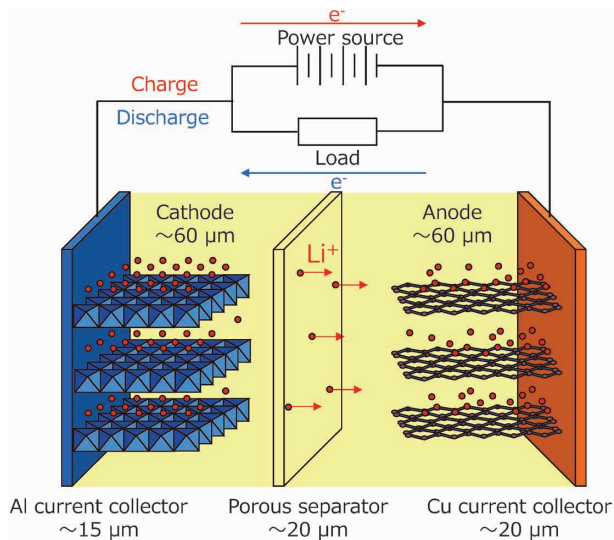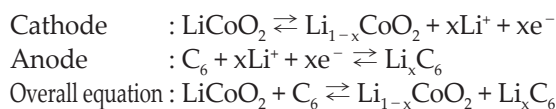
Fig. 1 Schematic diagram of a typical lithium-ion battery

Cathode : $LiCoO_2 \rightleftarrows Li_{1-x}CoO_2 + xLi^+ + xe^-$
Anode : $C_6 + xLi^+ + xe^- \rightleftarrows Li_xC_6$
Overall equation : $LiCoO_2 + C_6 \rightleftarrows Li_{1-x}CoO_2 + Li_xC_6$

Meanwhile, stationary storage batteries are becoming more common as the introduction of renewable energy sources such as photovoltaic and wind power generation expands. However, as the share of renewable energy--whose output fluctuates greatly depending on the weather conditions--increases, it flows back into the grid of electric power companies, causing large frequency fluctuations and adversely affecting the stable supply of electric power. Such cases are becoming apparent. For a stable supply of electric power, there are high expectations for ample MWh-class battery storage for peak-shaving and peak-shifting.

1.1 Further energy densification of cathode

The lamellar oxide $LiCoO_2$ used as a cathode material in lithium-ion batteries has been widely applied to mobile devices. However, approximately 60% of the world's production of Co, a rare metal, is produced in the Democratic Republic of the Congo (DRC), and the country's political instability makes the risky location and price hikes an issue. This has spurred the development of Li $(Ni_{1/3}Co_{1/3}Mn_{1/3})$ O_2 (NCM111), in which Co is partially replaced with Ni and Mn.[2),3)] In 2010, when the study for automotive applications was underway, $LiMn_2O_4$ with spinel structure and $LiFePO_4$ with a low cost and excellent thermal stability, despite its low operating voltage, were also used, in addition to NCM111. However, from the viewpoint of cruising distance, cathode materials with high energy density have been preferred, and cathode materials for in-

vehicle batteries have converged on NCM-based materials, which are being applied to lithium-ion batteries for EVs. In the charge/discharge process of NCM111, the preferential redox reaction is Ni^{2+}/Ni^{4+}. For even higher energy density, studies are being conducted to apply an increased Ni ratio, e.g., Li $(Ni_{0.5}Co_{0.2}Mn_{0.3})O_2$ (NCM523), Li $(Ni_{0.6}Co_{0.2}Mn_{0.2})$ O_2(NCM622), and Li $(Ni_{0.8}Co_{0.1}Mn_{0.1})O_2$(NCM811).[4),5)] Recently, $LiFePO_4$, which has excellent thermal stability, has been attracting attention again from the viewpoint of safety when used in EVs.

1.2 Further energy densification of anode

The anodes of lithium-ion batteries are mainly made of carbon materials, but the theoretical capacity of graphite is 372 mAh/g, and more than 90% of the theoretical capacity has already been used as the effective capacity. For further energy densification of anodes, research and development are underway on Si-based alloy anodes with a greater theoretical capacity than graphite. Si has an excellent capacity to occlude lithium ions; however, the volume expands by approximately a factor of 4 when fully charged. The significant expansion and contraction associated with occluding and releasing lithium ions during charge/discharge cycles cause pulverization and a rapid decline in capacity. Hence, SiO with Si nanoclusters dispersed in a SiO_2 matrix has been commercialized to improve the cycle life.[6), 7)] SiC and SiO-C are also being studied.[8), 9)] Furthermore, the morphology control of particles, such as Si nanoparticles and nanowires, is also being investigated.[10), 11)]

2. Analysis/evaluation technology contributing to the development of high energy density batteries

2.1 Visualization of reaction distribution in the depth direction of electrode

Kobelco Research Institute. Inc (KRIJ) is engaged in the prototyping and evaluation of lithium-ion batteries. The company can prototype electrodes using various materials, including developed products, and prototype batteries of cylindrical, laminated, and square types, as shown in **Fig. 2**. These are being used to elucidate cycle degradation and storage degradation mechanisms.[12)] This section introduces new evaluation and analysis techniques for battery development oriented toward high energy density, such as in-vehicle batteries.

In-vehicle batteries are subjected to the charge/discharge of a large current during regenerative charging at startup/deceleration and quick charging.
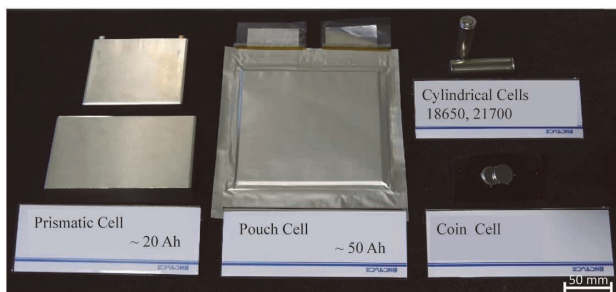
Fig. 2 Battery cells for testing

A large amount of lithium ion moves between electrodes inside the battery, resulting in lithium-ion distribution in the electrode's depth direction.[13] In other words, excessive reactions are repeated in the electrode surface layer near the opposite pole, resulting in localized degradation and a decline in capacity and input/output characteristics. However, in the case of the NCM cathode, lithium ion moves through the electrolyte to resolve its potential difference from the moment charge/discharge ends, and a relief phenomenon occurs, which averages the amount of lithium between active materials. Therefore, the analysis could not capture the reaction distribution after the relief. KRIJ has developed a new method of instantly removing electrolytes, which serve as relief paths, and has succeeded in solidifying the lithium-ion distribution in the electrode without relief.

A battery using a $Li(Ni_{0.8}Co_{0.15}Al_{0.05})O_2$ cathode (NCA) was prototyped, and the electrolyte was removed after discharge at a 3C rate. The rate 1C refers to a current that discharges at the rated capacity of 1 h, and the rates 2C and 3C refer to currents that discharge at the rated capacity of 1/2 h and 1/3 h, respectively. Sampled electrodes were thinned in the cross-sectional direction using a microtome. Transmission imaging XAFS measurements were performed at BL08B2 at the SPring-8. Imaging XAFS is a technique to visualize the spatial distribution of chemical bonding states in a sample area of a few square millimeters using a two-dimensional X-ray detector. The Ni K-edge was measured, and machine-learning noise reduction was performed on the X-ray transmission images. **Fig. 3** shows the distribution of Ni valence, which is a color intensity image of the energy value around the normalized intensity of 0.3 in the X-ray absorption near edge structure (XANES) region. A higher energy value indicates a higher state of charge (where discharge is not in progress). The upper part of Fig. 3 is on the side of the opposite pole (anode side), and the lower part is on the side of the current collector. It is confirmed that the reaction preferentially occurs on the electrode surface
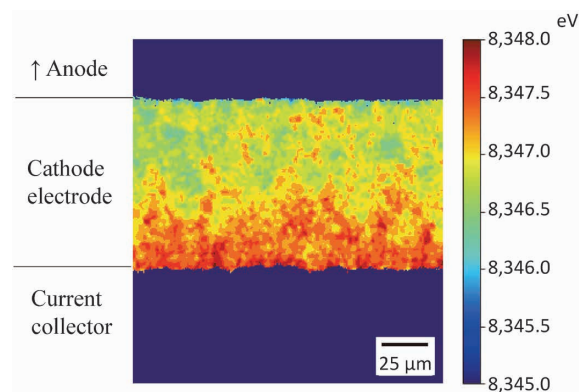

Fig. 3 Energy distributions of Ni K-edge XAFS in the NCA cathode

near the anode. For EV batteries, it is necessary to increase the amount of active material to achieve higher capacity. Designing an electrode with thick film and high density is prone to such a reaction distribution, which may cause rapid capacity decline and an increase in resistance. Understanding the reaction distribution of the battery to be used and controlling the charge/discharge rate appropriately will lead to longer battery life.

2.2 Visualization of electron conduction path in the depth direction of electrode

On the other hand, the formation and maintenance of an appropriate electron conduction path are necessary for the charge transfer reaction to proceed at the electrolyte/active material interface. Using $LiNi_{0.5}Mn_{1.5}O_4$ (LNMO), a next-generation active material for 5 V-class high-potential cathodes, a cathode was prototyped for cycle degradation tests. After 300 cycles of charge/discharge at a 2C rate, the capacity declined significantly to 30% of what it had been initially. The cross-sectional shape of the LNMO cathode and the electron conduction path are shown in **Fig. 4**. The left column shows atomic force microscope (AFM) images; the upper row shows the initial product, and the lower row shows the degraded product. The degraded product shows more cracks in the active material than the initial product, especially in the upper part near the anode, which is pulverized by the expansion and contraction caused by charge/discharge. The electron conduction path detected, by scanning spread resistance microscope (SSRM) is visualized in the right column of Fig. 4. The SSRM is a method to visualize the distribution of resistance values by scanning the sample surface with a conductive probe. In the degraded product, the electronic conduction of the electrode surface layer near the anode has declined significantly. The repeated
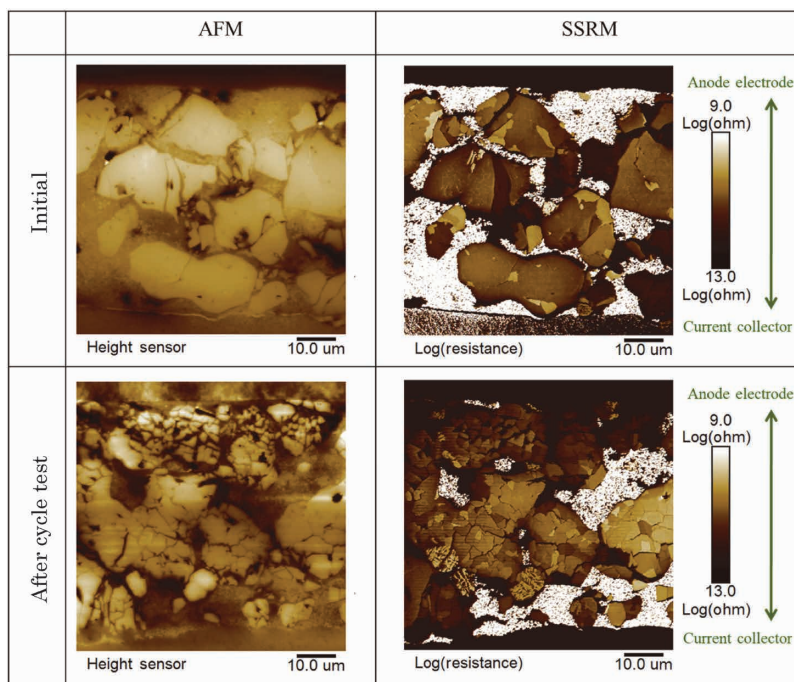
Fig. 4 Cross sectional views of LNMO cathodes and electron conduction paths

insertion desorption of excess lithium ion in the electrode surface layer is considered to have caused the active material of the electrode surface layer to be pulverized and the electron conduction path of the conductive agent to be cut off. Since no electrode reaction takes place unless electrons are supplied together with lithium ions, the breakage of the electron conduction path causes a significant decline in capacity.

2.3 Non-destructive degradation diagnostic technology for reuse

Used lithium-ion batteries are increasing with the spread of EVs, and efforts are underway to reuse them in stationary energy storage systems. The differential analysis of the charge/discharge curve is a method to evaluate cathode degradation and anode degradation by obtaining peaks corresponding to phase transitions of the active material without breaking down the battery. A storage test was conducted on a prototype battery using NCA as the cathode active material and graphite as the anode active material, and the battery was kept fully charged at 70℃ for one week. **Fig. 5** shows the charge/discharge curves before and after the storage test and the dV/dQ curve obtained by differentiating the charge/discharge curve. Fig. 5(b) indicates by arrows the peaks derived from graphite stage structure identified from KRIJ's monopole data. The peak shifts to the high voltage side due to storage degradation. In the charged
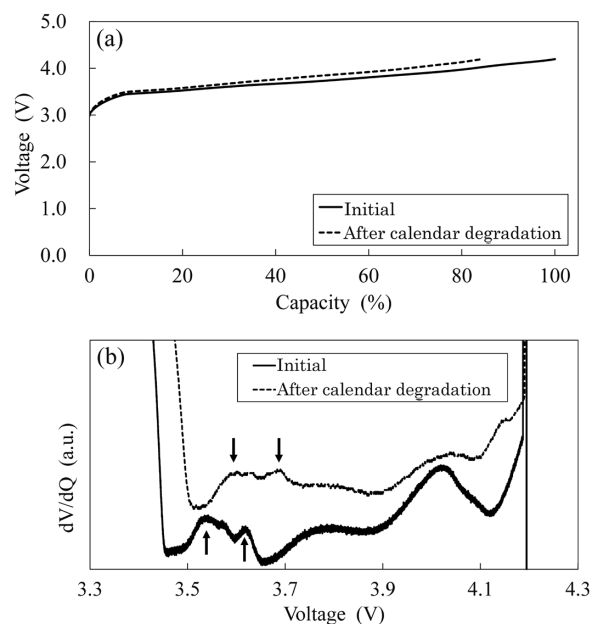
Fig. 5 Charge curves (a) and dV/dQ curves (b) before and after calendar degradation

state, the anode is exposed to a strongly reducing environment, and the electrolyte decomposition reaction occurs, during which the lithium ion inserted into the anode is incorporated into the sub-reaction of film formation and becomes carbonate or phosphate, thereby reducing the amount of lithium ion available for operation. This causes a gap between the cathode and anode capacities, and as the capacity range of the cathode used shifts to the high potential side, the anode peak also shifts relative to the high voltage side. Thus, utilizing the

monopole information allows the degradation state to be analyzed non-destructively.

3. Expectations for new batteries

3.1 Secondary battery project initiatives in Japan

In NEDO's "Research and Development Initiative for Scientific Innovation of New Generation Batteries (RISING)" (FY2009-FY2015) and "Research and Development Initiative for Scientific Innovation of New Generation Batteries 2 (RISING2)" (FY2016-FY2020), the development of an innovative battery with an energy density of 500 Wh/kg, which significantly exceeds the performance of conventional lithium-ion batteries, has been promoted through industry-government-academia collaboration, aiming at a cruising distance equivalent to that of current gasoline-powered vehicles. The candidates for new batteries include a fluoride shuttle battery with anion as a charge compensation carrier, a battery using conversion reaction, a zinc-air battery, and a lithium-sulfur battery. From FY2021 on, NEDO's "Research and Development Initiative for Scientific of New Generation Batteries 3" will focus on the research and development of fluoride batteries and zinc anode batteries that can achieve both high energy density and safety while using inexpensive materials with few resource constraints.

Basic research on all-solid-state batteries has been conducted by ALCA-Specially Promoted Research for Innovative Next Generation Batteries (ALCA-SPRING). Studies are underway from basic research to practical application, including the research and development of the production process of an all-solid-state lithium-ion battery, aimed at installation in EVs, in NEDO's "Development of Material Evaluation Techniques for Advanced and Innovative Batteries (Phase 2)", which began in FY2019.[14)-16)]

The Element Strategy Initiative of the Ministry of Education, Culture, Sports, Science, and Technology is developing sodium-ion batteries as eco-friendly post-lithium-ion batteries. As mentioned above, lithium-ion batteries have been commercialized and are being applied to EVs and sizeable stationary power sources. However, for large power supplies, in which material costs play a more significant role, the reduction of environmental impact and cost performance are prioritized. Therefore, there is a high expectation for the development of sodium-ion batteries, whose charge carriers use sodium, with reserves approximately 1,000 times greater than those of lithium,[17)] a rare element with a small Clarke number.

The prototyping/evaluation technology for the all-solid-state battery and sodium-ion battery, which are nearing commercialization as new batteries, is introduced below.

3.2 Prototyping/evaluation technology of all-solid-state battery

KRIJ has been independently synthesizing solid electrolyte, prototyping and evaluating all-solid-state batteries based on sulfide, and is entering the phase of practical application. **Fig. 6** shows the ionic conductivity of glass-ceramic $Li_7P_3S_{11}$, LGPS-type $Li_{10}GeP_2S_{12}$, and argyrodite-type Li_6PS_5Cl and Li_6PS_5Br at various temperatures as representative examples of sulfide-based solid electrolytes synthesized at KRIJ.[18)] Some systems exhibit ionic conductivity close to the ionic conductivity of 10^{-2} S/cm^2 of electrolyte and are nearing practical application. The rate characteristics of a coated all-solid-state battery using Li_6PS_5Cl are shown in **Fig. 7**. The discharge capacity of more than 80% is maintained even at a 5C rate, showing excellent
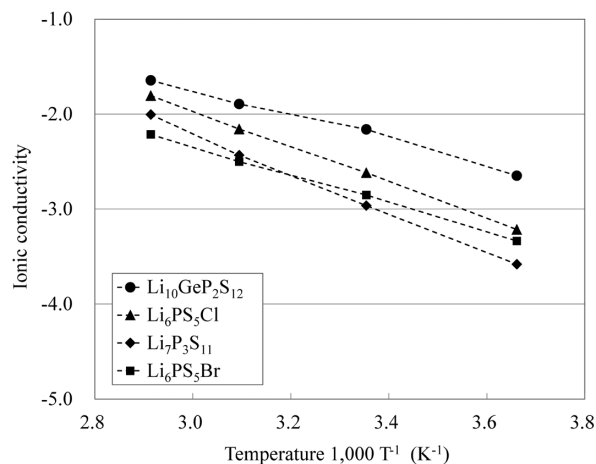

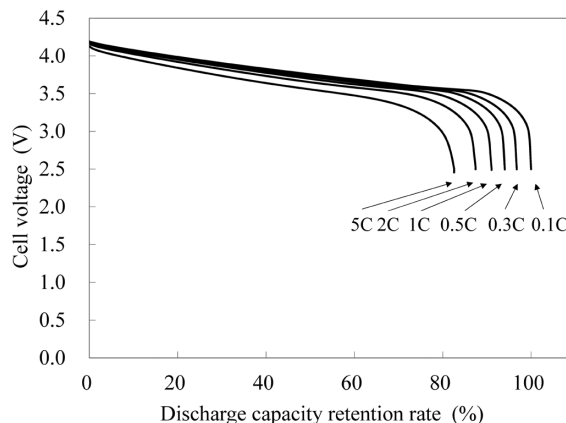Fig. 6 Ionic conductivity of sulfide-based solid electrolytes

Fig. 7 Discharge rate characteristics of sulfide-based all-solid-state batteries

output characteristics. In electrolyte, in addition to lithium ion (cation), a counterpart anion is transferred, and the ion transport number of lithium ion, which contributes to ionic conduction, is about 0.3.[19] On the other hand, solid electrolyte differs from the electrolyte in that the ion transport number of lithium ion is 1. In electrolyte, a solvothermal reaction occurs in which solvent molecules of electrolyte are coordinated around lithium ion, and a desolvation reaction occurs when lithium ion is inserted into active material. In a solid electrolyte, there is no reaction with the solvent, and the reaction occurs smoothly at the solid-electrolyte/active-material interface, making the battery system suitable for high-speed charge/discharge.

3.3 Prototyping/evaluation technology of sodium-ion battery

The history of investigating cathode materials used in sodium-ion secondary batteries is long, and many studies have been conducted on oxide, phosphate, sulfide, and other cathode materials.[20)-23)] In the oxide system, starting with $NaCoO_2$, the $NaMeO_2$ compound (Me: transition metal element) with a layered rock salt structure is a promising candidate. The ionic radius of transition metals Fe and Li are close, and cation mixing occurs quickly, making $LiFeO_2$ electrochemically inert. On the other hand, $NaFeO_2$ is electrochemically active, and inexpensive Fe can be selected as a transition metal.[24] In the layered rock salt structure where the Fe^{3+}/Fe^{4+} reaction is used, the P2 and O3 types have been studied.[25), 26)]

Focus was placed on the O3-type layered rock salt structure, which has been used in lithium-ion batteries, to synthesize $Na(Fe_{1/3}Mn_{1/3}Co_{1/3})O_2$, $Na(Ni_{1/3}Fe_{1/3}Co_{1/3})O_2$, and $Na(Ni_{1/3}Mn_{1/3}Fe_{1/3})O_2$ based on $Na(Ni_{1/3}Mn_{1/3}Co_{1/3})O_2$ with lithium replaced by sodium, and Ni, Mn, and Co replaced by Fe, respectively. Sodium-ion batteries using these for their cathodes were prototyped, and their redox reaction and charge/discharge characteristics were investigated.

A case of $Na(Fe_{1/3}Mn_{1/3}Co_{1/3})O_2$ is shown as an example of redox reaction analysis. Mössbauer measurement of Fe by transmission ^{57}Fe Mössbauer spectroscopy was performed at room temperature in the velocity range $\pm$ 5.2 mm/s. **Fig. 8** shows the Mössbauer spectrum of $Na(Fe_{1/3}Mn_{1/3}Co_{1/3})O_2$ adjusted to each voltage. A paramagnetic doublet spectrum is observed in each sample. The isomer shift reflects the s-electronic charge density and is also known as the chemical shift. On the other hand, the quadrupole split reflects the electric field gradient induced by the oxygen ligands in the matrix. At 2.5 V, Fe exhibits a typical quadrupole split and is in a single Fe^{3+} valence state. On the other hand, the shape of the Fe^{3+} doublet becomes gradually asymmetric with increasing voltage. The analysis with Fe^{3+} and Fe^{4+} has confirmed that the average valence of Fe increased due to an increase in the Fe^{4+} component by the desorption of sodium ions.

Fig. 9 shows the hard X-ray XAFS measurement results for $Na(Fe_{1/3}Mn_{1/3}Co_{1/3})O_2$ at the Fe-K

IS (mm/s) +0.33
QS (mm/s) 0.61

IS (mm/s) +0.31
QS (mm/s) 0.61
IS (mm/s) -0.07
QS (mm/s) 0.39

IS (mm/s) +0.26
QS (mm/s) 0.61
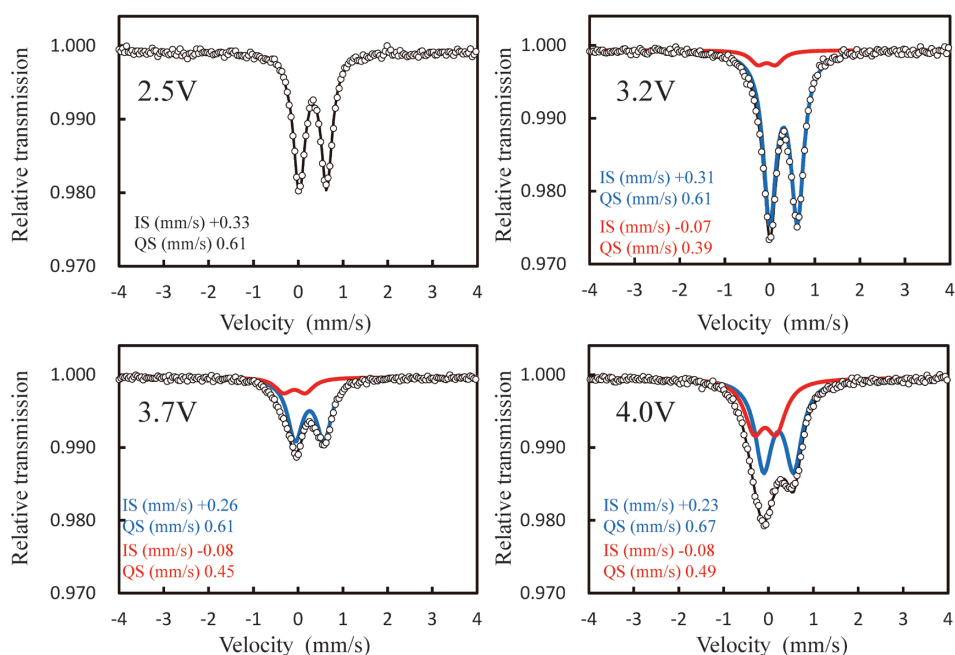IS (mm/s) -0.08
QS (mm/s) 0.45

IS (mm/s) +0.23
QS (mm/s) 0.67
IS (mm/s) -0.08
QS (mm/s) 0.49

Fig. 8 ^{57}Fe Mössbauer spectra of $Na(Fe_{1/3}Mn_{1/3}Co_{1/3})O_2$
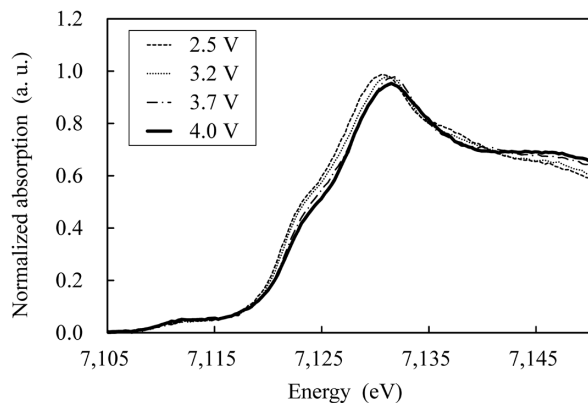
Fig. 9 Fe K-edge X-ray absorption spectra of Na $(Fe_{1/3}Mn_{1/3}Co_{1/3})O_2$
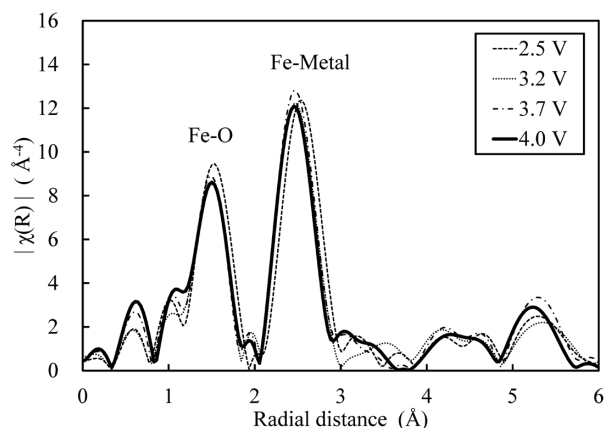

Fig.10 Radial distribution functions around Fe atoms

absorption edge adjusted to each voltage. Comparison with a reference sample has confirmed Fe to be Fe^{3+} after synthesis. As the voltage increases, the XANES spectrum shifts to the high-energy side, confirming an increase in the average valence of Fe, similar to the Mössbauer results. The radial distribution function around Fe is shown in **Fig.10**. In the radial distribution function around Fe, the lattice spacing of Fe-O, the first proximal lattice, shrinks as the voltage increases, suggesting an increase in valence, which indicates a redox reaction of Fe.

Fig.11 compares the discharge capacities. Thus, by appropriately selecting inexpensive transition metals such as Fe, various capacities and operating voltages can be expressed, and the creation of a wide variety of materials can be expected. The ionic radius of sodium is larger than that of lithium, so the Coulomb force is smaller, and if the desolvation process is diffusion-controlled,[27] charge/discharge can be performed faster than with a lithium-ion battery. Combinations with high output characteristics have also been reported,[28] and expectations for sodium-ion batteries as post-lithium-ion batteries are growing.
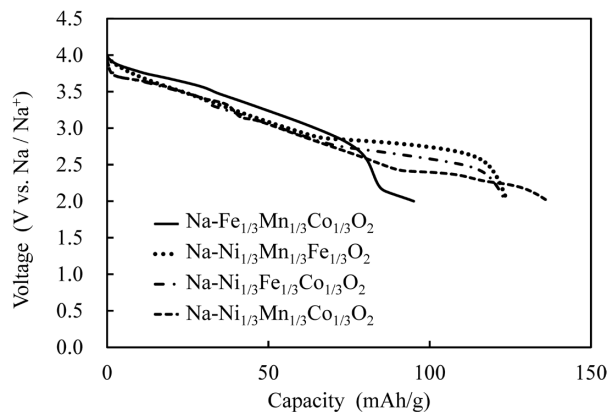
Fig.11 Comparison of discharge capacity of O3 type layered rock salt structure cathode materials

Conclusions

The promotion of decarbonization efforts in the international community is an urgent task. The decarbonization of power sources is progressing with the social implementation of hydrogen energy, the electrification of vehicles, and the introduction of renewable energy. Secondary batteries are an essential technology for EVs and electric power storage, and efforts are being made to improve the high energy density and safety of current liquid lithium-ion batteries. In addition, there are high expectations for the emergence of new batteries, such as all-solid-state batteries and sodium-ion batteries. Kobelco Research Institute will support the research and development of secondary batteries by providing prototypes of secondary batteries, physical analysis, chemical analysis, safety tests, and combined analysis with CAE, and will contribute to the realization of SDGs and carbon neutrality.

References

1) J. Yamaki. Chemistry today. 2019, No.585, pp.39-41.
2) N. Yabuuchi et al. J. Electrochem. Soc. 2005, No.152, No.7, pp.A1434-A1440.
3) N. Yabuuchi et al. J. Power Sources. 2005, Vol.146, pp.636-639.
4) H. -J. Noh et al. J. Power Sources. 2013, Vol.233, pp.121-130.
5) A. Verma et al. J. Electrochem. Soc. 2017, Vol.164, No.13, pp.A3380-A3392.
6) Y. Hwa et al. J. Power Sources. 2013, Vol.222, pp.129-134.
7) K. Pan et al. J. Power Sources. 2019, Vol.413, pp.20-28.
8) J. Saint et al. Adv. Funct. Mater. 2017, Vol.17, pp.1765-1774.
9) M. Yamada et al. J. Electrochem. Soc. 2011, Vol.158, No.4, pp.A417-A421.
10) P. Hovington et al. J. Power Sources. 2014, Vol.248, pp.457-464.
11) C. K. Chan et al. J. Power Sources. 2009, Vol.189, pp.1132-1140.
12) T. Tsubota et al. R&D Kobe Steel Engineering Reports. 2015, Vol.65, No.2, pp.92-97.

13) M. Katayama et al. J. Vac. So. Jpn. 2015, Vol.58, No.10, pp.375-378.

14) A. Hayashi et al. Electrochem. Commun. 2003, Vol.5, No.8, pp.701-705.

15) N. Ohta et al. Adv. Mater. 2006, Vol.18, No.17, pp.2226-2229.

16) N. Kamaya et al. Nature Mater. 2011, Vol.10, pp.682-686.

17) S. Okada et al. Electrochemistry. 2015, Vol.83, No.3, pp.170-175.

18) K. Kataoka et al. Journal of the Japanese Association for Crystal Growth. 2019, Vol.46, pp.1-10.

19) Y. Yamada et al. Nature Energy. 2019, Vol.4, pp.269-280.

20) B. L. Ellis et al. Nature Mater. 2007, Vol.6, pp.749-753.

21) A. Kitajou et al. J. Power Sources. 2012, Vol.198, pp.389-392.

22) K. Chihara et al. Electrochim. Acta. 2013, Vol.110, pp.240-246.

23) De-long Ma et al. Nano Energy. 2014, Vol.10, pp.295-304.

24) J. Zhao et al. J. Electrochem. Soc. 2013, Vol.160, pp.A3077-A3081.

25) M. Sathiya et al. Chem. Mater. 2012, Vol.24, pp.1846-1853.

26) N. Yabuuchi et al. Nature Mater. 2012, Vol.11, pp.512-517.

27) N. Nakayama et al. J. Power Sources. 2007, Vol.174, pp.695-700.

28) T. Tsubota et al. Evergreen 2019, Vol.6, No.4, pp.275-279.

Recent Development Trends in Materials for Bipolar Plates of Proton Exchange Membrane Fuel Cells (PEMFCs) and Kobe Steel's Activities

Toshiki SATO[*1]

[*1] Materials Research Laboratory, Technical Development Group

Abstract

Proton exchange membrane fuel cells (PEMFCs) are expected to become clean energy sources for transportation applications. Their bipolar plates, which are crucial parts of PEMFCs, significantly affect the durability, power-generation performance, and cost of PEMFCs. Thus, much effort has been made to improve the durability and performance of bipolar plates and reduce their costs. To improve the corrosion resistance and interfacial contact resistance (ICR), which affect the durability and characteristics of bipolar plates, Kobe Steel has been developing coated titanium using an unprecedented film and process since 2004. This paper reviews the recent development of carbon-polymer composites and coated metals, considered materials for bipolar plates, while focusing on their corrosion resistance and ICR. Also described is Kobe Steel's effort to develop film for titanium bipolar plates.

Introduction

Since the Industrial Revolution began in the mid-eighteenth century, the human race has produced various forms of energy by burning fossil fuels to enrich people's lives. On the other hand, greenhouse gases such as carbon dioxide, which are emitted into the atmosphere in large quantities as generative products, are causing global warming. This problem threatens the survival of the human race by driving up the average global temperature. Hence, efforts to achieve carbon neutrality, moving toward zero net greenhouse gas emissions, are rapidly accelerating worldwide. In Japan, the government declared in October 2020 that it aims to be carbon neutral by 2050.[1] Hydrogen plays a critical role in carbon neutrality. It is used for fuel cells, which are clean power generation systems that only emit water produced by the reaction of hydrogen and oxygen and essential products driving decarbonization. In particular, proton exchange membrane fuel cells (PEMFCs) have been used for automobiles,[5] thanks to their low-temperature operation, quick start, high energy efficiency, compact size, and light weight.[2)-4)] Their development is underway to reduce costs further and promote widespread use.

Among the components making up an automotive PEMFC, bipolar plates are estimated to account for 80% of the PEMFC's weight, 50-65% of its volume, and 35-40% of the PEMFC's total cost.[6] Since they are required to perform various functions, they are positioned as one of the essential components of PEMFCs, and efforts are being made to reduce costs and improve performance.

This paper reviews recent research and development trends in bipolar plates, which are vital components of automotive PEMFCs, focusing mainly on interfacial contact resistance (hereinafter referred to as "ICR") and durability, and also describes Kobe Steel's latest efforts in bipolar plate development.

1. PEMFC's structure and characteristics required for bipolar plate

Fig. 1 schematically shows the structure of a PEMFC. A PEMFC comprises stacks of basic units called cells, surrounded by dotted squares. Each cell consists of a polymer electrolyte membrane coated with platinum catalyst on both sides and gas diffusion layers (hereinafter referred to as "GDLs") on both sides, which are sandwiched between bipolar plates from the outside. Conductive carbon paper or carbon cloth is used for the GDLs to distribute hydrogen and oxygen uniformly on the platinum catalyst surface and to conduct electrons. The power generation voltage per cell is approximately 0.6 to 1 V,[7)-9)] and to obtain high output, 300 to 400 cells are usually stacked for passenger car applications.[10), 11)] Since two bipolar plates are required per cell, the number of bipolar plates_ranges from 600 to 800.

As shown in Fig. 1, a bipolar plate discharges water generated by flowing hydrogen and oxygen and also serves as a channel for cooling water flowing on the opposite side of the fuel gas. Therefore, channels must be formed on it by press forming or other means. The bipolar plate must also have high thermal conductivity because the cooling water plays a role in maintaining the PEMFC temperature at an appropriate level by removing the excess heat generated in the power generation process. In addition, since the bipolar plate serves as a current collector that collects and conducts
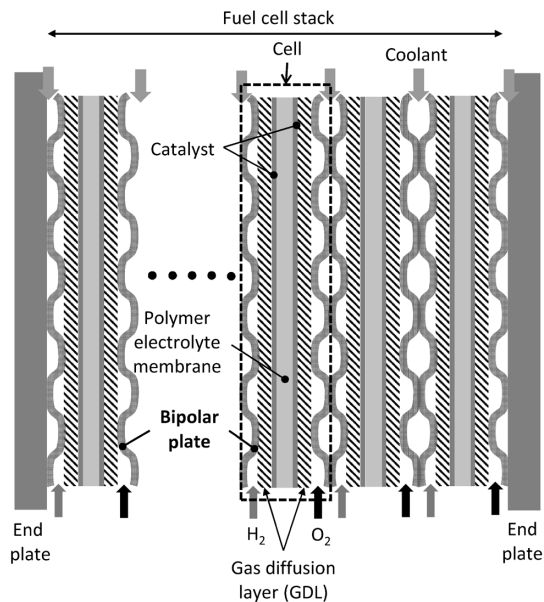
Fig. 1 Schematic diagram of a proton exchange membrane fuel cell (PEMFC) stack

Table 1 DOE technical targets for bipolar plates

Characteristic	Units	2025 target
Plate cost (guideline)	$/kW	2
Plate weight (guideline)	kg/kW	0.18
Plate H_2 permeation coefficient	Std cm^3 /sce·cm^2·Pa	2×10^{-6} @80°C, 3atm 100%RH
Corrosion anode (guideline)	µA/cm^2	<1 and no active peak [pH3.0, 0.1ppmF, 80°C, Ar purge 0.1mV/s, -0.2 to 0.4VvsSHE]
Corrosion cathode (guideline)	µA/cm^2	<1 [pH3.0, 0.1ppmF, 80°C, aerated at 1.0VvsSHE for> 24h]
Electrical conductivity	S/cm	>100
Interfacial contact resistance	Ω·cm^2	<0.01 (at a compaction force of 1.38MPa)
Flexural strength	MPa	>40
Forming elongation	%	40

electrons generated by the decomposition of hydrogen on the platinum catalyst, the resistance, or ICR, of the surface in contact with the GDL must be low. Furthermore, the inside of a PEMFC is a corrosive environment of acid with a pH of 2 to 3.[12), 13)] Thus, the bipolar plate is also required to have corrosion resistance. In the case of automotive applications, not only lightweight but also thinning of the bipolar plate is necessary because PEMFCs are often mounted in a limited space, for example, in passenger cars.[14)] They must also be strong enough to withstand automobiles' vibrations and mechanical shocks.[8)]

Thus, bipolar plates are required to have many functions and characteristics, as well as a low cost. As shown in **Table 1**, the US Department of Energy (hereinafter referred to as "DOE") has set 2025 target values for the cost and characteristics required for bipolar plates for transport equipment,[15)] and

research and development are being conducted to achieve these target values. As a result of many research and development efforts, two promising materials have been identified: carbon-resin composite materials and surface-treated metals.

2. Bipolar plate materials

2.1 Carbon-resin composite material

A carbon-resin composite is a material in which a resin is mixed with more than a set amount of conductive carbon fillers to improve electrical conductivity by the phenomenon of rapid network formation among fillers based on the percolation theory[24)]. Those fillers include graphite powder,[16), 17)] expanded graphite powder,[16), 19), 20)] carbon fibers,[16)-18)] carbon black,[17), 18)] carbon nanotubes,[17), 18), 21)] and graphene.[22), 23)] Although its electrical conductivity, thermal conductivity, and material strength are inferior to those of metals, it has excellent corrosion resistance. Therefore, it has already been put into practical use in stationary fuel cells, where long-term durability is required, and there is little need to reduce size and weight through strength and thinning.[25)] In automotive applications, it is suitable for large commercial vehicles and buses with enough space for installation, even if the bipolar plate is thickened to ensure strength.[14), 26)]

The resin materials used as a base can be classified into two types: thermosetting resins such as phenol resin,[16), 19)] epoxy resin,[17), 18)] and vinyl ester resin;[28)] and thermoplastic resins such as polyethylene resin, polypropylene resin, polyphenylene sulfide resin,[20), 27)] polyvinylidene fluoride resin,[28), 29)] and polyphenylene sulfide resin.[30)] Thermosetting resins are cured by increasing the crosslink density through the polymerization reaction by heating and thus have high strength and heat resistance. It also has the advantage of being easy to increase electrical and thermal conductivity because it can be mixed with more carbon filler thanks to its low viscosity. On the other hand, it has the disadvantages of low toughness and low productivity compared with thermoplastic resin, due to its low impact resistance and long reaction time. Thermoplastic resin softens when heated to or above its glass-transition temperature or to a temperature at or above the melting point, and generally has lower creep strength and heat resistance than thermosetting resin. Another disadvantage is that it is difficult to add a large amount of carbon filler due to its high viscosity. On the other hand, it has the advantages of high toughness and impact resistance. It also enjoys high productivity, since it quickly

solidifies when cooled below its melting point or glass-transition temperature.

Although the characteristics thus differ between the resin types, the common issues are compatibility with regards to conductivity, material strength, and the hydrogen-gas leakage barrier property. The carbon filler must be added in 35 to 85 wt.% to increase conductivity. Although the conductivity increases with the amount of carbon filler added, the strength and hydrogen-gas leakage barrier property decrease due to the aggregation of carbon fillers and void formation caused by the resin not covering the carbon filler completely.[31), 37)] Carbon-resin composite materials are mainly formed into bipolar plate shapes by compression or injection molding; however, a resin-rich layer with low carbon filler composition is formed on the surface, resulting in a significant increase in ICR.[14), 31)] For this reason, several methods have been investigated, including a method to remove the resin-rich layer using Ar plasma or by mechanical polishing,[32), 33)] a method to prevent the formation of a resin-rich layer by inserting a soft film such as fluoride ethylene-propylene copolymer between the carbon-resin composite and the mold during molding,[34)] and a method of forming a graphite film on the surface by inserting graphite foil between the mold and the carbon-resin composite and performing compression molding.[35)] The features of the manufacturing method of carbon-resin composite materials and bipolar plates are summarized by A. Tang et al.,[36)] S. Porstmann et al.,[14)] and N. Saadat et al.,[37)] and these references should be consulted.

2.2 Metallic materials

The high strength of metals enables weight reduction by thinning, and channels can be easily formed by press forming. In addition, its high electrical and thermal conductivity and the absence of hydrogen gas leakage problems make it a strong candidate material for bipolar plates in PEMFCs. However, due to the high temperature, high humidity, and acidic corrosive environment inside PEMFCs, metal ions dissolve due to corrosion and penetrate the platinum catalyst layer as well as polyelectrolyte membrane, poisoning them and reducing their output and leading to power generation failure in the worst case.[8), 15)] In addition, the ions of transition metals such as Fe, Co, and Cu act as catalysts for the Fenton reaction, which generates OH radicals that destroy the solid polymer electrolyte membrane in PEMFC.[15), 38)] For this reason, metals such as aluminum,[39), 40)] copper,[41), 42)] stainless steel,[43)-57)] and titanium[58)-68)] have been considered. However, in consideration of corrosion resistance, these have been reduced to corrosion-resistant metals, i.e., stainless steel and titanium.[14)] A Google scholar search of English papers on corrosion resistance and contact resistance for the five years from 2017 to 2021 shows 64 for stainless steel and 23 for titanium, compared with 9 for aluminum and 4 for copper. In particular, stainless steel has been the most widely considered because it has a lower base material cost than titanium. On the other hand, although titanium is more expensive than stainless steel, it shows high corrosion resistance in high temperatures, high humidity, and acidic atmospheres.[8)] Thus, it has less elution as metal ions and less toxicity to solid polymer electrolyte membrane and platinum catalyst.[69)] Furthermore, its low density, approximately 60% of that of stainless steel, contributes to the weight reduction of PEMFC. Stainless steel and titanium exhibit corrosion resistance thanks to an oxide film called passivation film with a thickness of several to 10 nm. However, this film brings high electrical resistance on the surface, resulting in high ICR, low power generation efficiency, and in the worst case, power generation failure. Therefore, the practical application of metallic bipolar plates depends on developing an inexpensive surface treatment technology that combines corrosion resistance and conductivity.

3. Surface treatment technology for metallic bipolar plates

Regardless of the type of base material, the surface treatments under consideration are classified as follows: i) nitride[44), 51), 61)] and carbide[63), 64)] films of group 4a, 5a, 6a elements in the periodic table; ii) films of amorphous carbon[49), 53), 68)] and graphene[62), 66)]; iii) conductive oxide films[57)]; iv) films that are diffusion-processed such as chromizing[56)] and nitriding[60)]; v) films of noble metals,[48)] 4a, 5a group metals[70), 71)] or Ni-P plated[65)] metals; and vi) resin films containing conductive nanoparticles.[72)] Except for v) and vi), the films are conventional hard films, most of which are deposited by existing methods. The rest are those in which multilayering of these films attempted to improve adhesion,[43), 54)] pinhole reduction to improve corrosion resistance,[50), 55)] and doping of elements to improve corrosion resistance and ICR.[43), 47), 73)]

Table 2 and **Table 3** summarize the results of ICR and polarization current measurements before and after the polarization testing for the main surface treatments of stainless steel and titanium over the last five years. The types of films studied

Table 2 A summary of the results of corrosion tests and ICR measurements of coatings for stainless steel bipolar plates in the main literature in the past 5 years

| Substrate | Coating & film thickness(nm) | Coating method[3] | Corrosion test condition | | | P[1] (MPa) | ICR(mΩ·cm²) | | ΔICR[2] (mΩ·cm²/h) | Corrosion current (μA/cm²) | Ref. |
			Electrolyte	Temp. (°C)	Polarization conditions ①anode, ②cathode		Before polarization	After cathode polarization			
SUS316L	Ti-doped a-C[3](625-725)/Ti(100)	MS	0.5M H₂SO₄ + 2ppm F⁻	70	②0.6VvsSCE for 2h 1.4sSCE for 1h	1.5	Coated =3.47−5.64	—	—	Coated =0.28-0.58	43
SUS430	β-Nb₂N(600)	Molten salt	0.5M H₂SO₄ + 2ppm F⁻	70	0.17VvsSHE for 500h, H₂ purge	1.4	SUS430=5.3 Coated=2.3	SUS430=29.5 Coated=3.8	SUS430=12.1 Coated=0.75	SUS430=7 Coated=0.1-0.3	44
SUS316L	C doped CrTiN	MS	0.5M H₂SO₄ + 0.2ppm F⁻	70	1.1VvsSHE for 2h	1.4	SUS316L=276 Coated=4.8	Coated=7.6	Coated=1.4	Coated=0.609	47
SUS316L	Au dots on TiN	TiN=MS Au=TS	pH3 H₂SO₄ + 0.1ppm F⁻	80	②0.67VvsAg/AgCl for 96h, air purge	1.38	Coated=1.72	Coated=5.84	Coated=0.043	Coated =0.2±0.04	48
SUS316L	a-C(545)/Ti:C /Ti(100)	MS and heat treatment	0.5M H₂SO₄ + 2ppm F⁻	70	②0.6VvsSCE for 5h	1.5	SUS316L=106.12 Coated=3.31	SUS316L=163.03 Coated=5.64	SUS316L=11.4 Coated=0.47	SUS316L=5.96 Coated=0.1	49
SUS316L	TiN/TiAlN multilayer	AIP	0.5M H₂SO₄ + 2ppm F⁻	80	①-0.1VvsSCE for 4h, H₂ purge ②0.6VvsSCE for 4h, O₂ purge	1.4	SUS316L=59 Coated=6	SUS316L=94 Coated=10	SUS316L=8.8 Coated=1	Coated= ①0.4,②0.73	50
SUS316L	CrN	MS	0.6M H₂SO₄	60	②0.48VvsSCE for 16h, O₂ purge	1.0	Coated=8.4	—	—	Coated=0.1	51
SUS304	TiB₂(2×10⁴)	HEMAA	0.3M H₂SO₄ + 2ppm F⁻	25	No polarization immersion for 480h	1.5	SUS304=50 Coated=19	SUS304=60 Coated=19	SUS304=0.021 Coated=0	—	52
SUS316L	a-C(200)	MS	0.5M H₂SO₄ + 5ppm F⁻	80	②0.6VvsSCE for 12h, air purge	1.5	SUS316L=12.60 Coated=2.91	SUS316L=19.28 Coated=4.06	SUS316L=0.56 Coated=0.096	Coated =0.00752	53
SUS316L	TiN(1100)/Ti TiAlN(1100 -1300)/TiN/Ti	MS	0.5M H₂SO₄ + 5ppm F⁻	70	②0.6VvsSCE for 5h, air purge	1.4	TiN=8.3 TiAlN=12.6	TiN=14.3 TiAlN=22.1	TiN=1.2 TiAlN=1.9	TiN≒0.11 TiAlN<0.1	54
SUS316L	TiN(50)/Ti(50) multilayer	AIP	0.5M H₂SO₄ + 2ppm F⁻	70	②0.6VvsSCE for 1h, O₂ purge	1.4	SUS316L=150 Coated=11	SUS316L=276 Coated=18	SUS316L=126 Coated=7	SUS316L=0.22 Coated=0.033	55
SUS316L	Cr(6×10⁴)	CH	0.5M H₂SO₄ + 2ppm F⁻	70	①-0.1VvsSCE for 4h, H₂ purge ②0.6VvsSCE for 4h, O₂ purge	1.4	SUS316L=105.2 Coated=1.4	SUS316L=166.7 Coated=4.5	SUS316L=15.4 Coated=0.78	Coated 0.14-0.16	56
SUS316L	Nb-doped TiO₂(700)	Sol-gel	0.1M H₂SO₄	80	②0.6VvsSCE for 720h, air purge		SUS316L=58 Coated=38	SUS316L=70 Coated=41	SUS316L=0.017 Coated=0.0041	SUS316L=5 Coated=0.042	57

1) P=Compaction force of ICR measurement ． 2) ΔICR=(ICR before polarization - after cathode polarization)/cathode poralization time

3) a-C=Amorphous carbon, MS=Magnetron Sputtering, TS=Thermal Spray, AIP=Arc Ion Plating, HEMAA=High Energy Micro Arc Alloying CH=Chromising

Table 3 A summary of the results of corrosion tests and ICR measurements of coatings for titanium bipolar plates in the main literature in the past 5 years

| Coating & film thickness(nm) | Coating method[3] | Corrosion test condition | | | P[1] (MPa) | ICR(mΩ·cm²) | | ΔICR[2] (mΩ·cm²/h) | Corrosion current (μA/cm²) | Ref. |
		Electrolyte	Temp. (°C)	Polarization conditions ①anode, ②cathode		Before polarization	After cathode polarization			
Ta,N-doped TiO₂	Sol-gel	0.3M HCl		No polarization only an immersion of 240h		Coated=71	Coated=73	Coated=0.008	—	59
Ti₂N(700-2100)	Plasma nitriding	pH3 H₂SO₄ and 0.1ppmF⁻	80	①-0.1VvsSCE for 4h ②0.6VvsSCE for 4h	1.5	Uncoated=12.63 Coated=4.06-5.98	Uncoated=26.25 Coated=4.94-8.0	Uncoated=3.4 Coated=0.36	①Negative ②0.08	60
TiN(1900-2800)	AIP	0.5M H₂SO₄ and 2ppm F⁻	70	—	1.4	Uncoated=35.0 Coated=3.0-3.5	—	—	—	61
Graphene oxide (2000)	EPD and heat treatment	0.5M H₂SO₄ and 2ppm F⁻		①-0.1VvsSCE for 4h, H₂ bubble ②0.6VvsSCE for 4h, air bubble	1.8	Uncoated=173.62 Coated=3.98	—	—	①0.264 ②0.294	62
TiC(2000)	DGPSM	0.5M H₂SO₄ and 2ppm F⁻	70	①-0.1VvsSCE for 4h, H₂ bubble ②0.6VvsSCE for 4h, air bubble	1.4	Uncoated=98.1 Coated=7.5	Uncoated=176.9 Coated=16.9	Uncoated=19.7 Coated=2.4	①-0.27 ②0.17	63
NbC(700)	Sputtering	0.5M H₂SO₄ and 3ppm F⁻	75	①-0.1VvsSCE for 4h, H₂ bubble ②0.6VvsSCE for 4h, air bubble	1.4	Uncoated=91.9 Coated=16.6	Uncoated=180.4 Coated=24.5	Uncoated=22.1 Coated=2.0	①-0.26 ②0.32	64
Ni-P including TiN nanoparticles	Electroless plating	0.5M H₂SO₄ and 2ppm F⁻	70	①-0.1VvsSCE for 5h, H₂ bubble ②0.6VvsSCE for 5h, air bubble	1.4	—	Coated=3.5-8.7	—	①1.56 ②0.21	65
Graphene oxide (2000)	ED and heat treatment	0.5M H₂SO₄ and 2ppm F⁻	70	①-0.1VvsSCE for 5h, H₂ bubble ②0.6VvsSCE for 5h, air bubble	1.4	Coated=about 4	Coated=about 4	Coated=0	①0.2 ②0.2	66
Carbon/PTFE/TiN composite(2300)	Hydrothermal method	0.5M H₂SO₄ and 2ppm F⁻	70	①-0.1VvsSCE for 5h, H₂ bubble ②0.6VvsSCE for 5h, air bubble	1.6	Uncoated=80 Coated=9.5-14	—	—	①0.92 ②0.53	67
a-C(534-1281) /Ti	MS	0.5M H₂SO₄ and 5ppm F⁻	70	②0.6VvsSCE for 2h	1.5	Coated=6.52	—	—	②0.1	68

1) P=Compaction force of ICR measurement ． 2) ΔICR=(ICR before polarization - after cathode polarization)/cathode poralization time

3) MS=Magnetron Sputtering, AIP=Arc Ion Plating, EPD=Cathodic Electrophoretic Deposition, DGPSM=Double Glow Plasma Surface Modification, ED=Electrodeposition

during that period have not changed significantly compared with those of the five years before that, and the main objective has been to improve the performance of films. In polarization testing, which evaluates the elution of metal ions from bipolar plate materials, i.e., corrosion resistance, the components and composition of the evaluation solutions are mainly evaluated under stricter conditions than those shown in Table 1 for the DOE's 2025 target evaluation conditions. Nevertheless, surface-treated stainless steel and titanium meet the current targets of DOE for corrosion. The corrosion current lower than that of the untreated base material, indicating that the surface treatment is effective in improving corrosion resistance. On the other hand, since there is no provision in DOE's goal to measure the ICR after polarization testing, most of the literature measures only the initial ICR before polarization or measures the ICR after a few hours of polarization in a corrosive environment more severe than DOE's conditions. Selecting films with ICR that is stable in the PEMFC environment for metallic bipolar plates is vital. Hence, to compare the film's stability, a 0.5 kmol/m^3 aqueous solution of sulfuric acid containing 0 to 5 ppm of fluorine ions, the most frequent evaluation condition in Tables 2 and 3, was prepared. In this aqueous solution, the ICR increment ΔICR per 1 h was calculated by taking the difference between the ICR after polarization and the ICR before polarization and dividing it by the polarization time for the film polarized at an electric potential of 0.6 VvsSCE. The results are shown in Table 2, Table 3, and **Fig. 2**. Although this is a rough estimation of the trend, ΔICR tends to be large for nitride and carbide and small for the films of amorphous carbon and graphene. The conductive carbon material is used as a resin-carbon composite material with high durability, but it also shows excellent characteristics as a film in terms of ICR stability.

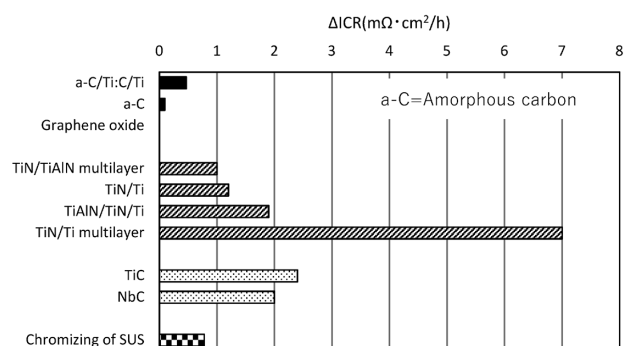It should be noted that the DOE's durability target for 2025 for an 80 kW class fuel cell vehicle is set at 8,000 h.[15] To accurately evaluate the durability time of films for metallic bipolar plates, it will be necessary to set appropriate acceleration evaluation conditions and develop evaluation techniques to predict long-term ICR changes.

4. Kobe Steel's approach

4.1 Kobe Steel's approach to bipolar plate material development

Kobe Steel has been developing surface treatment technology for bipolar plates using titanium as the base material since 2004. Titanium is characterized by its high corrosion resistance and resistance to elution even at high electric potentials. W. Li et al. deposited a film of amorphous carbon on the surface of SUS316L and grade 2 titanium.[68] They observed the surface after 1 h of holding in an aqueous solution at 70℃ of 0.5 kmol/m^3 sulfuric acid, with the addition of 2 ppm of fluorine ion, at an electric potential of 1.4 VvsSCE, simulating the start-up and shutdown of a fuel cell vehicle. As a result, they reported that pitting was observed in the pinhole defects of amorphous carbon in SUS316L, while no pitting was observed in titanium. This suggests that titanium is insensitive to elution, even with pinholes. On the other hand, the present author observed cracks in the graphite layer after the press-forming of graphite-coated titanium.[77] E. Haye et al. applied biaxial tension simulating press-forming on a film of CrN deposited on the surface of SUS316L. They reported cracks in the CrN, and approximately 11% of the SUS316L base material was exposed.[51] As mentioned in the previous section, most of the films under consideration are hard, brittle films. Therefore, press forming after surface treatment is considered to cause cracks in the surface-treated layers of both titanium and stainless steel, exposing the base material. However, from the viewpoint of reducing the production cost of bipolar plates, precoat treatment, in which surface treatment is performed before press forming, is advantageous, as pointed out by S. Porstmann et al.[14] and J. M. Huya-Kouadio et al.[26] Precoating can increase productivity by the continuous surface treatment of coils, allowing fuel-cell manufacturers to simply press-form bipolar plates. This eliminates the need for time-consuming handling of each bipolar plate after pressing for transport to the surface treatment process and subsequent surface treatment. Since titanium is corrosion-resistant, pinholes and exposure to the base material are considered acceptable. Thus, it is highly feasible to shorten the film deposition or precoating time, which may result

Fig. 2 Amount of increase per hour in ICR of each coating by cathode polarization

in thinner films with more pinholes. On the other hand, precoating stainless steel is difficult because the base material exposure increases the risk of degrading power generation performance due to the elution of the base material.

In addition, conventional development has been dominated by using existing film and film deposition technologies to reduce the cost of surface treatment. Against this backdrop, Kobe Steel has been developing unique surface treatment technologies with the goal of precoat titanium, considering that conventional technologies have limitations in performance improvement and production cost reduction. The following is a brief description of surface treatment technologies developed by Kobe Steel.

4.2 Titanium material surface-treated with noble metals

Titanium alloy with a mixed film of noble metal and titanium oxide,[74), 75)] and Au-coated titanium with a nano-level thickness of Au film[76)] have been developed using noble metals such as Pd, Pt, and Au, which are resistant to elution in the fuel cell environment and maintain conductivity.

Making a composite coating of noble metal-titanium oxide comprises dissolving titanium by immersing a titanium alloy containing noble metal in a nitric hydrofluoric acid solution to concentrate the noble metal on the surface and performing oxidation treatment in low oxygen partial pressure. The thin film is approximately 50 nm thick, ensuring conductivity by the noble metals. Ti-0.15 wt.% Pd alloy was immersed in an aqueous sulfuric acid solution at 80℃ and pH 2 for 1,000 h. Its ICR was approximately 5 mΩ·cm^2 before and after the immersion with almost no change. The power generation test incorporating the PEMFC showed excellent power generation performance equivalent or superior to that of graphite bipolar plates.[75)]

Since titanium-noble metal alloy contains noble metal in the titanium matrix, unnecessary noble metal that does not contribute to the ICR leads to higher costs. Au-coated titanium is a cost-effective way to reduce costs by eliminating unnecessary noble metals as much as possible. This is pure titanium coated with a 5 to 20 nm thick Au film deposited by sputtering followed by heat treatment in a vacuum. Generally, the film is deposited after removing the passivation film on the titanium surface to ensure the adhesion of the film. The drawbacks are that the passivation film, which provides corrosion resistance to titanium, is removed and that the removal of this film takes a long time. Hence, a film of Au is deposited without removing the passivation film. A part of the oxygen in the passivation film is diffused and absorbed into titanium by vacuum heat treatment, changing it to oxygen-deficient conductive titanium oxide. This increases the conductivity and improves the adhesion of Au by diffusing Au into the titanium oxide layer. The ICR remained at approximately 4 mΩ·cm^2 after 1,000 h of application of 0.65 VvsSCE electric potentials in an aqueous solution of sulfuric acid at 80℃ and pH 2, showing excellent durability. The PEMFC power generation test showed excellent performance equivalent to or better than that of graphite bipolar plates.

4.3 Graphite-coated titanium material[77)]

The noble metal-based film in the previous section has the disadvantage of a high production cost due to the high price of noble metal and the time-consuming vacuum process. Hence, graphite-coated titanium has been developed to reduce costs by adopting an atmospheric process without using noble metals. Aqueous paint containing graphite powder is applied to both sides of the titanium foil. The graphite layer is formed by stretching the graphite powder into a film by passing it through a roll press (**Fig. 3**). Finally, a TiC adhesion layer is formed at the interface between the graphite layer and titanium by heat treatment that also serves as strain relief annealing of titanium. The ICR hardly increased and was maintained at approximately 4 mΩ·cm^2 even after applying the electric potential of 0.65 VvsSCE for 1,000 h in an aqueous solution of sulfuric acid at 80℃ and pH 2, exhibiting excellent durability.
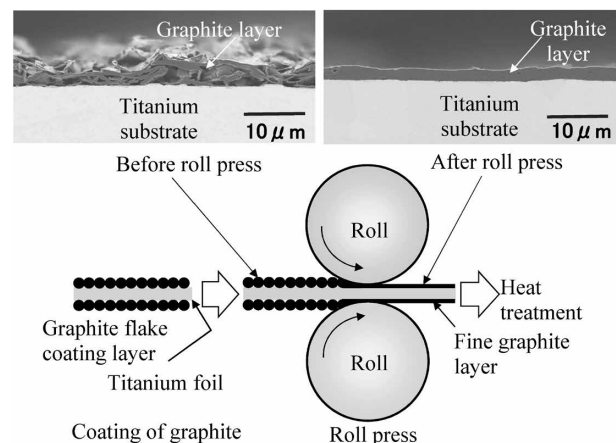

Fig. 3 Process of graphite coating on titanium and structures of graphite layers before and after roll press

Conclusions

The bipolar plate is a critical component that dramatically affects the performance, life, and cost of PEMFCs. Efforts are underway to improve the performance and reduce the cost of carbon-resin composite material and surface-treated metal, which are candidates for bipolar plate materials. The major challenges in the case of carbon-resin composites are compatibility between the material strength/hydrogen leakage barrier and bulk resistance/contact resistance, and in the case of metals, the development of surface treatment film that achieves long-term durability at a low cost. Since titanium can be precoated and has excellent corrosion resistance, it is a promising material with the potential for cost reduction through increased bipolar plate productivity and long-term durability.

Kobe Steel has been developing a unique surface treatment technology for titanium for many years, aiming at durability and cost reduction. As a result, the company has developed precoat type nano-Carbon composite coat (NC) titanium and realized its mass production. NC titanium is used as bipolar plate material in the MIRAI (trademark of Toyota Motor Corporation), a fuel cell vehicle launched in December 2020. Kobe Steel will strive to continue its efforts for further performance improvement and cost reduction and contribute to carbon neutrality through the prevalence of fuel cell vehicles.

References

1) Ministry of Economy, Trade and Industry. Green Growth Strategy Through Achieving Carbon Neutrality in 2050. 2021.
2) S. Gottesfeld et al. Adv. Electrochem. Sci. Eng. 1997, Vol.5, pp.195-301.
3) Y. Tang et al. Appl. Energy, 2011, Vol.88, pp.68-76.
4) D. Garrain et al. Smart Grid and Renewable Energy. 2011, Vol.2, No.2, Article4954.
5) Y. Tanaka et al. TOYOTA Technical Review. 2021, Vol.66, No.2, pp.6-11.
6) S. Mahabunphachai et al. J. Power Sources. 2010, Vol.195, No.16, pp.5269-5277.
7) T. Kawai. Jour. Jpn. Soc. Mech. Eng. 2016, Vol.119, No.1169, pp.206-211.
8) T. Bohackova et al. Materials. 2021, Vol.14, No.10, Article 2682.
9) S. Karimi et al. Ad. Mater. Sci. Eng. 2012, Article828070.
10) S. Mizuno et al. TOYOTA Technical Review. 2021, Vol.66, No.2, pp.22-27.
11) H. Nakaji et al. Manufacturing & Technology. 2016, Vol.68, No.2, pp.72-75.
12) M. Hashimoto et al. J. Jpn. Inst. Met. 2007, Vol.71, pp.545-552.
13) M. Ueda et al. J. Japan Inst. Met. Mater. 2007, Vol.71, No.7, pp.545-552.
14) S. Porstumann. J. Manufac. Proc. 2020, Vol.60, pp.366-383.
15) U. S. DRIVE Fuel cell technical team roadmap New York US Drive partnership. 2017, pp.1-34.
16) R. Taherian et al. Mater. & Design, 2011, Vol.32, pp.3883-3892.
17) J. H. Lee et al. J Power Sources. 2009, Vol.193, pp.523-529.
18) N. A. M. Radzuan et al. Composition Part B. 2017, Vol.110, pp.153-160.
19) A. Masand et al. Mater. Res. Express. 2017, Vol.4, No.9, Article095604.
20) P. Rzeczkowski et al. Polymers. 2019, Vol.11, No.3, Article 462.
21) K. Yao et al. Energy & Fuels. 2017, Vol.31, No.12, pp.14320-14331.
22) M. Phuangngamphan et al. J. Appl. Polym. Sci. 2019, Vol.136, No.11, Article47183.
23) N. A. M. Radzuan et al. Int. J. Hydrogen Energy. 2019, Vol.48, No.58, pp.30618-30626.
24) N. Afiqah et al. Int. J. Hydrogen Energy, 2017, Vol.42, pp.9262-9273.
25) H. Sakai et al. Journal of Japan Society for Fuzzy Theory and Intelligent Informatics. 2019, Vol.1, No.2, pp.653-661.
26) J. M. Huya-Kouadio et al. Electrocem. Soc. 2018, Vol.83, No.1, pp.93-109.
27) H. E. Lee et al. Composite Structures. 2015, Vol.134, pp.44-51.
28) B. Hu et al. Int. J. Hydro. Energy. 2021, Vol.46, pp.25666-25676.
29) E. Planes et al. Composites Sci. Technol. 2015, Vol.110, pp.17-25.
30) M. C. L. de Oliveira et al. Int. J. Hydro. Energy. 2014, Vol.39, pp.16405-16418.
31) K. I. Jeong et al. Composite Structures. 2021, Vol.262, Article 113617.
32) H. N. Yu et al. Composite structures. 2012, Vol.94, pp.1911-1918.
33) B. Avasarala et al. J. Power Sources. 2009, Vol.188, pp.225-229.
34) D. Lee et al. Composite Structures. 2017, Vol.160, pp.976-982.
35) H. N. Yu et al. J. Power Sources. 2011, Vol.196, pp.9868-9875.
36) A. Tang et al. J. Renew. Sustain. Energy. 2021, Vol.13, No.2, Article022701.
37) N. Saadat et al. Renew. Sustain. Energy Rev. 2021, Vol.138, Article110535.
38) Q. Tang et al. Inter. J. Hydro. Energy. 2021, Vol.46, pp.22040-22061.
39) J. Barranco et al. Inter. J. Hydro. Energy. 2010, Vol.35, pp.11489-11498.
40) A. E. Fetohi et al., Inter. J. Hydro. Energy. 2012, Vol.37, pp.7677-7688.
41) V. V. Nikam et al. Electrochem. Acta. 2006, Vol.51, pp.6338-6345.
42) S.S. Hsieh et al. Micron. 2008, Vol.39, pp.263-268.
43) W. Li et al. Mater. Chem. and Phys. 2022, Vol.276, Article 125234.
44) L.X. Yang et al. Inter. J. Hydrogen Energy. 2021, Vol.46, pp.33206-33214.
45) Q. Jia et al. Mater. Today Chem. 2021, Vol.21, Article100521.
46) J. Li. J. Mater. Sci. 2021, Vol.56, pp.8689-8703.
47) B. Mi et al. Inter. J. Hydrogen Energy. 2021, Vol.46, pp.32645-32654.
48) X. Z. Wang et al. Corrosion Sci. 2021, Vol.189, Article 109624.
49) W. Li et al. Inter. J. Hydrogen Energy. 2021, Vol.46, pp.22983-22997.

50) S. P. Mani et al. J. Mater. Sci. 2021, Vol.56, pp.10575-10596.

51) E. Haye et al. Inter. J. Hydrogen Energy, 2020, Vol.45, pp.15358-15365.

52) R. Y. He et al. Corrosion Science. 2020, Vol.170, Article 108646.

53) H. Li et al. J. Power Source. 2020, Vol.469, Article228269.

54) J. Jin et al. Mater. Chem. and Phys. 2020, Vol.245, Article 122739.

55) S. Jannat et al. J. Power Source. 2019, Vol.435, Article226818.

56) Z. Dong et al. Inter. J. Hydrogen Energy. 2019, Vol.44, pp.22110-22121.

57) Y. Wang et al. Corrosion Sci. 2018, Vol.142, pp.249-257.

58) W. Yan et al. Diamond and related Mater. 2021, Vol.120, Article108628.

59) Y. Wang et al. J. alloys and Compounds. 2021, Vol.879, Article160470.

60) H. Shen, L. Wang. Inter. J. Hydrogen Energy. 2021, Vol.46, pp.11084-11091.

61) T. Li et al. Inter. J. Hydrogen Energy. 2021, Vol.46, pp.31382-31390.

62) Y. Liu et al. Coatings. 2021, Vol.11, Article437.

63) J. Shi et al. Inter. J. Hydrogen Energy. 2020, Vol.45, pp.10050-10058.

64) P. Zhang et al. Surface Coating Technology. 2020, Vol.397, Article126064.

65) C. Ouyang et al. Int. J. Electrochem. Sci. 2020, Vol.15, pp.80-93.

66) J. Wang et al. Inter. J. Hydrogen Energy. 2019, Vol.44, pp.16909-16917.

67) P. Gao et al. Inter. J. Hydrogen Energy. 2018, Vol.43, pp.20947-20958.

68) W. Li et al. Diamond and Related Mater. 2021, Vol.118, Article108503.

69) Y. A. Dobrovol'skii et al. Russian J. General Chem. 2007, Vol.77, No.4, pp.752-765.

70) M.-T. Lin et al. Surface Coatings Technol. 2017, Vol.320. pp.217-225.

71) Y. S. Kim et al. Materials. 2021, Vol.14, No.17, Article4972.

72) Y. Wang et al. Progress in Organic Coatings. 2019, Vol.137, Article105327.

73) J. Jin et al. Inter. J. Hydrogen Energy. 2017, Vol.42, pp.11758-11770.

74) T. Sato et al. R&D Kobe Steel Engineering Reports. 2005, Vol.55, No.3, pp.48-51.

75) T. Sato et al. Ti-2007 Sci. and Technol. Japan Inst. of Mater. 2007, pp.1679-1682.

76) T. Sato et al. R&D Kobe Steel Engineering Reports. 2010, Vol.60, No.2, pp.29-32.

77) T. Sato et al. R&D Kobe Steel Engineering Reports. 2015, Vol.65, No.2, pp.21-24.